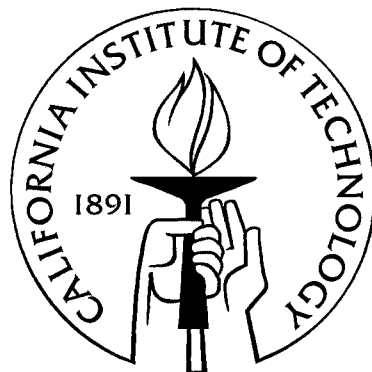


# Nanophotonic Devices Based on Planar Photonic Crystals

Thesis by  
Marko Lončar

In Partial Fulfillment of the Requirements  
for the Degree of  
Doctor of Philosophy



California Institute of Technology  
Pasadena, California

2003  
(Submitted June 2, 2003)

UMI Number: 3091463

Copyright 2003 by  
Loncar, Marko

All rights reserved.



---

UMI Microform 3091463

Copyright 2003 by ProQuest Information and Learning Company.  
All rights reserved. This microform edition is protected against  
unauthorized copying under Title 17, United States Code.

ProQuest Information and Learning Company  
300 North Zeeb Road  
P.O. Box 1346  
Ann Arbor, MI 48106-1346

© 2003

Marko Lončar

All Rights Reserved

*To my parents, Jele and Luka Lončar.  
Mojim roditeljima, Jeli i Luki Lončar.*

# Acknowledgements

I came to Caltech six years ago to study power electronics and build efficient DC-DC converters, but instead I ended up building one of the world's smallest lasers. It was my adviser Professor Axel Scherer who sparked my interest in nano-science and who gave me the opportunity to explore the exciting field of nanoscale optics. I would like to thank Axel for his guidance and for the research freedom that I have enjoyed, and I am grateful for his understanding and support. The experience that I have gained by working in his group will be of invaluable importance in my future career.

I would like to thank my former adviser Professor Slobodan Ćuk for giving me the opportunity to come to Caltech and for the understanding that he showed for my newly developed research interests. I would like to acknowledge the help and many fruitful discussions I have had with professors Amnon Yariv, Hideo Mabuchi, Demetri Psaltis and Stephen Quake.

I am thankful to Professor Jelena Vučković and Tomoyuki Yoshie, my friends, colleagues and collaborators for all the great times we shared together. It has been a great pleasure to know you and work with you guys! Also, I would like to thank all the other members of Caltech Nanofabrication Group for putting up with me all these years, and in particular to Professor Oskar Painter, David Barsic, Professor Theodor Doll, Mark Adams, Dr. Koichi Okamoto, Michael Hochberg, Tom Behr-Jones, Jeremy Witzens, Terrel Neal and Brett Maune. Special thanks are due to our group's administrative assistant Kate Finigan and lab coordinator Dr. Guy DeRose.

Throughout my education I was fortunate to have excellent teachers who were able to spark my interest in science and help me recognize my talents and ambitions. I would like to thank the teachers from my elementary school "Svetozar Miletić" (Zemun, Serbia), my high school "Matematička Gimnazija" (Belgrade, Serbia) and the Faculty of Electrical Engineering at the University of Belgrade (Serbia).

I would like to thank my friends, people that have touched my life in many different

ways, for their friendship, support and love.

Finally, I am grateful for the constant love and support that I've been receiving from my sister Marija, my parents Jele and Luka and my family back in Croatia and Bosnia. My parents have been my greatest inspiration and my first teachers. They have developed my interest in science, but also they have taught me to enjoy other aspects of life. I am grateful for their love, devotion and support that has carried me through difficult times and helped me reach my dreams. This thesis is for them.

# Abstract

Photonic Crystals, man-made periodic structures with a high refractive index contrast modulation, have recently become very interesting platform for the manipulation of light. The existence of a photonic bandgap, a frequency range in which propagation of light is prevented in all directions, makes photonic crystals very useful in applications where spatial localization of light is required. Ideally, by making a three-dimensional photonic crystal, propagation of light in all three dimensions can be controlled. Since fabrication of 3-D structures is still a difficult process, a more appealing approach is based on the use of lower dimensional photonic crystals. A concept that has recently attracted a lot of attention is a planar photonic crystal based on a dielectric membrane, suspended in the air, and perforated with a two-dimensional lattice of holes.

In this thesis theoretical and experimental study of planar photonic crystal nanolasers, waveguides and super-dispersive elements is presented. Room temperature operation of low-threshold nanolaser is demonstrated, both in air and in different chemical solutions. For the first time, we have demonstrated that photonic crystal nanocavity lasers can be used to perform spectroscopic tests on ultra-small volumes of analyte. Our porous cavity design permits the introduction of analyte directly into the high optical field of the laser cavity, and therefore it is ideally suited for the investigation of interaction between light and matter on a nanoscale level. We showed that small changes in refractive index of the ambient surrounding the laser can be detected by observing the shifts in emission wavelengths of the laser. Our lasers can be integrated into large arrays to permit the analysis of many reagents at the same time. The nanolasers can also be integrated with photonic crystal waveguides to form the integrated systems of higher complexities. Theoretical and experimental investigation of various photonic crystal waveguide designs is discussed. Details of the fabrication procedure used to realize nanophotonic devices in silicon on insulator as well as InGaAsP materials are presented.

# Contents

<b>Acknowledgements</b>	<b>iv</b>
<b>Abstract</b>	<b>vi</b>
<b>1 Introduction</b>	<b>1</b>
1.1 Photonic Crystals . . . . .	2
1.2 The Origin of The Photonic Band-Gap . . . . .	5
<b>2 Photonic Crystal Slabs</b>	<b>9</b>
2.1 Introduction . . . . .	9
2.2 Comparison between Square and Triangular Photonic Crystal Lattices . . . . .	12
2.3 Geometry-dependent Properties of Photonic Crystals . . . . .	14
2.3.1 Influence of the Hole Size . . . . .	14
2.3.2 Influence of the Refractive Index of Environment . . . . .	17
2.3.3 Influence of the Refractive Index of the Slab . . . . .	18
2.4 Propagation of Light in Photonic Crystal Slabs . . . . .	19
2.4.1 Self-collimation in Square Lattice PPCs . . . . .	21
2.4.2 Complete Band-diagram of Triangular Lattice PPC . . . . .	27
2.5 Conclusion . . . . .	27
<b>3 Planar Photonic Crystal Cavities and Lasers</b>	<b>31</b>
3.1 Introduction . . . . .	31
3.2 High-Q Cavity Design . . . . .	36
3.3 Low-threshold Planar Photonic Crystal Nanolaser . . . . .	42
3.3.1 Fabrication Procedure . . . . .	44
3.3.2 Characterization of High-Q Cavities . . . . .	51

3.3.3	Room Temperature Laser . . . . .	56
3.4	Photonic Crystal Lasers as Chemical Sensors . . . . .	62
3.4.1	Fabrication of Photonic Crystal Bio-Chemical Sensors . . . . .	64
3.4.2	Chemical Sensing . . . . .	69
3.4.3	Dense Integration of Laser Sensors . . . . .	73
3.5	Conclusions and Future Work . . . . .	75
<b>4</b>	<b>Planar Photonic Crystal Waveguides</b>	<b>78</b>
4.1	Introduction . . . . .	78
4.2	Design of Planar Photonic Crystal Waveguides . . . . .	79
4.2.1	Single Line Defect Waveguide . . . . .	79
4.2.2	Effect of the Hole Size on the Waveguide Properties . . . . .	88
4.2.3	Waveguides Based on the Rearrangement of the PPC Lattice . . . . .	92
4.2.4	Waveguides Based on the Modification of the Hole Size . . . . .	98
4.3	Fabrication . . . . .	102
4.4	Experimental Characterization . . . . .	109
4.4.1	Transmission Measurements . . . . .	109
4.4.2	Measurement of the Dispersion of the Guided Modes . . . . .	114
4.5	Conclusions . . . . .	129
<b>Bibliography</b>		<b>131</b>

# List of Figures

1.1	Photonic crystals of different dimensionality (a) 1-D: Bragg mirror (after A. Scherer <sup>5</sup> ), (b) 2-D: Microstructured fiber (after R. F. Cregan <sup>6</sup> ) (c) 3-D: Yablanovite structure (after C. C. Chen <sup>7</sup> ) . . . . .	3
1.2	SEM micrograph of a planar photonic crystal waveguide fabricated in SOI wafer. . . . .	4
1.3	(a) Square lattice photonic crystal. (b) Si block, without air holes. . . . .	5
1.4	Dispersion diagrams for light propagating along the x-axis direction for various sizes of air holes in Si block. Normalized frequency in units $a/\lambda = \omega a/2\pi c$ is shown on the y-axis and normalized propagation constant on the x-axis. . . . .	6
1.5	The field profiles of dielectric and air band. It can be seen that light is concentrated in the Si in the case of then dielectric band, and in the air hole region in the case of the air band. . . . .	7
1.6	Band diagram calculated along high symmetry directions in 2-D photonic crystal lattice of square symmetry. The position of the first-order bandgap is indicated. The schematic of the irreducible first Brillouin zone is shown in the inset, along with the position of high symmetry points. . . . .	8
2.1	(a) Schematic of planar photonic crystal. Two mechanisms that make three-dimensional light localization possible are indicated. (b) Lightline (black solid line) and lightcone (gray region) overlaid on a dispersion diagram of the square lattice planar photonic crystal along the $\Gamma X$ direction. . . . .	10

2.2	(a) Schematic view of the Si slab patterned with 2-D square lattice of holes. Unit cell of the PC and boundary conditions used in the 3-D FDTD calculation are also indicated. (b) Si slab perforated with 2-D square lattice of holes. Without loss of generality, lattice constant $a$ in the figure is chosen to be $a = \pi/a$ (dimensionless units), in order to conveniently show reciprocal lattice vectors. The square represents the first Brillouin zone, and $\Gamma$ , $X$ and $M$ are the high symmetry points. (c) Si slab perforated with 2-D triangular lattice of holes. This time we chose $a = \frac{4\pi}{3a}$ . Hexagon represents the first Brillouin zone with high symmetry points indicated. . . . .	13
2.3	Band diagrams of eigen modes of Si slab perforated with 2-D lattice of holes of (a) square and (b) triangular symmetry. The x-axis represents different directions in the reciprocal lattice, and the y-axis normalized frequency in the units $a/\lambda$ . The gray region represents the light cone. Even modes (TE-like) are represented with circles and odd (TM-like) with stars. Insets show the SEM micrographs of the fabricated photonic crystal structure, and the first Brillouin zones. . . . .	15
2.4	Bandgap position as a function of relative hole size ( $r/a$ ) and relative thickness of the slab ( $t/a$ ). (a) Positions of the band edges are shown: top of the dielectric band with full circles, and bottom of the air band with open squares. (b) The width of the bandgap for various geometries. $n_{slab} = 3.5$ (Si) and $n_{env.} = 1$ (air). . . . .	16
2.5	Air-band and dielectric-band edge dependence on the refractive index of environment ( $n_{env.}$ ) surrounding PPC slab, for $r/a = 0.3$ (red) and $r/a = 0.4$ (blue). . . . .	18
2.6	Band diagrams for PPC realized in $Si_3N_4$ slab for two different hole sizes. Only TE-like modes are shown. . . . .	19
2.7	(a) Schematic view of the Si slab patterned with 2-D square lattice of holes. External light is incident to the slab at an angle $\theta$ . Unit cell of the PC, with boundary conditions used in the 3-D FDTD calculation, is also indicated. (b) Band diagram for TE-like (vertically even) modes of the square lattice PPC. Grey region represents the light cone. Inset shows high symmetry points in the first Brillouin zone. . . . .	20

2.8	(a) The dispersion ( $\omega(k)$ ) relation for the first two bands of the square PPC, calculated for all $k$ vectors in the first Brillouin zone. The light cone is represented as an unshaded mesh. (b) The iso-frequency contours for the first and (c) second band. The color represents different normalized frequencies - $a/\lambda$ . The vectors represent the gradient of frequency change as the function of $k_x$ and $k_y$ components. . . . .	22
2.9	The dispersion of the first two bands supported in the unpatterned Si slab. The light cone is represented as an unshaded mesh. The iso-frequency contours in the case of the unpatterned slab are circles (shown for $a/\lambda \in 0.2774, 0.3041, 0.3309$ ) since all in-plane directions are equivalent. . . . .	23
2.10	(a) The iso-frequency contours of the Band 2 of square lattice PPC. Only the region below the light cone is shown [ $\lambda \in (0.273, 0.306)$ ]. The light cone, for $\lambda = 0.306$ , is represented by the dashed circle. The light of frequency $a/\lambda = 0.3$ is self-collimated and propagates in the direction (in the real space) indicated by the gray color. (b) The iso-frequency contours of the unpatterned Si slab are circles. Light diverges at the angles shown in the gray color. . . . .	25
2.11	Evolution of the $B_z$ component of the EM-field excited in the (a) unpatterned slab and (b), (c) slab patterned with square lattice PPC. Structures were excited with dipole sources (with $E_x$ component) at frequencies (a) $a/\lambda = 0.19$ , (b) $a/\lambda = 0.19$ and (c) $a/\lambda = 0.295$ . Self-collimation can be observed in the case (c) as predicted. In this case, light is radiated predominantly along $\Gamma X$ directions. Radiation in $y - axis$ direction is stronger because the structure was excited with $E_x$ field only. . . . .	28
2.12	Band-diagram of the first three bands of a triangular PPC, calculated for all $k$ vectors in the first Brillouin zone. The light cone is represented as an unshaded mesh. . . . .	29
2.13	The bands of triangular lattice shown along with their iso-frequency contours. . . . .	30
3.1	Dispersion diagram for the modes supported in the triangular lattice planar photonic crystal ( $r/a = 0.3$ this time). Mode profiles for one component of the E field in the dielectric (red) and air (blue) band, taken at the X point, are also shown. . . . .	33

3.2	One of the dipole modes supported in a single defect cavity. In-plane and out-of-plane energy leaks can be observed. . . . .	34
3.3	Single defect cavity fabricated in AlGaAs, and designed to operate at $\lambda = 852$ nm. . . . .	35
3.4	(a) Conventional single defect cavity ( $p = 0$ ). When structure is “cut” along the dashed line, and two PPC half-planes are dislocated along $\Gamma X$ direction by $p/2$ , (b) high-Q cavity can be formed ( $p = 0.25 \cdot a$ ). . . . .	36
3.5	Defect modes of the cavity with $p/a = 10\%$ and $r_{def} = 0.2a$ . (a) Cavity supports two dipole modes, and their profiles are shown ( $B_z$ component and vector of the $\vec{E}$ field). Spectrum of the modes supported in the cavity, obtained using 3-D FDTD, is also shown. The bandgap is shown in white. (b) Amplitude of the E field is shown. It can be seen that light is localized in the small defect hole. . . . .	38
3.6	Dependence of the position of the two dipole modes of the cavity on the amount of dislocation introduced ( $p$ ), and the size of the defect hole ( $r_{def}$ ). . . . .	38
3.7	Dependence of the (a) vertical and (b) lateral quality factor of the HQ mode on the amount of dislocation ( $p$ ) and the size of the defect hole ( $r_{def}$ ). Only five layers of photonic crystal surrounding the defect hole was used. $Q_{lateral}$ can be improved by adding more photonic crystal layers. . . . .	40
3.8	Dependence of the (a) Q factor and (b) eigen-frequency of cavity resonance on the refractive index of analyte introduced in the cavity with $p/a = 25\%$ . . . .	41
3.9	High-Q cavity designs based on fractional edge dislocations fabricated in (a) AlGaAs, (b) SOI, (c) InGaAsP. . . . .	43
3.10	(a) Mask used for fabrication of high-Q cavities of the first generation. Mask consists of PMMA, Au and $Si_3N_4$ . (b) Patterns in PMMA after e-beam lithography. Au can be seen at the bottoms of the holes in the PMMA. . . . .	45
3.11	SEM micrographs of the cavity after the ion milling step: (a), (b) are top views, and (c) and (d) view at $30^\circ$ angle. . . . .	47
3.12	SEM micrograph of the sample after RIE. (a) Top view and (b) at $30^\circ$ angle.	47

3.13	Fabrication procedure for PPC lasers made in InGaAsP material. RF sputtering (1) is used to deposit dielectric and is followed by deposition of <i>Au</i> mask (2). E-beam lithography consists of PMMA deposition (3), e-beam writing (3) and PMMA developing (4). Patterns are transferred from PMMA into <i>Au</i> using IBE (5) and then into $Si_3N_4$ using RIE (6). Finally, cavities are etched into InGaAsP using ICP-RIE (7) and the membrane is released from the substrate in HCl (8). Final structure is a free standing InGaAsP membrane with four quantum wells (thin red layers). . . . .	49
3.14	SEM micrograph of the structure $b_4$ . Each structure consists of (a) six different cavities with different elongation parameters: $p_0 = 0$ , $p_1 = 0.05 \cdot a$ , $p_2 = 0.1 \cdot a$ , $p_3 = 0.15 \cdot a$ , $p_4 = 0.2 \cdot a$ and $p_5 = 0.25 \cdot a$ . (b) Blow-up of $p_3$ cavity, and (c) of a single hole (tilted). Quantum wells and undercut air region can be seen. (d) Optical image of all 50 fabricated structures. Structures for which we show experimental data are indicated by arrows. . . . .	50
3.15	SEM micrographs of (a) $a_2 p_4$ , (b) $b_1 p_5$ , (c) $b_4 p_4$ and (d) $b_4 p_5$ along with the distribution of hole sizes in the bulk photonic crystal mirrors surrounding each cavity. . . . .	52
3.16	Experimental setup. Pump beam ( $\lambda = 830$ nm) is focused on the sample using high-power NIR lens (100x). Si detector behind beam splitter (BS) is used to monitor the pump power. Emission from the sample is collected using the same lens, and is analyzed with an optical spectrum analyzer (OSA). The emission from photonic crystal resonators can also be monitored with an infrared camera (IR) using a pair of flip-up mirrors. Inset shows the size of the pump beam. . . . .	53
3.17	(a) Emission from unprocessed InGaAsP material and (b) from rectangular membrane suspended in air. Fabry-Perot resonances, due to rectangular cavity formed between etched facets, can be seen. . . . .	54
3.18	Structure $b_4$ . Position of resonant modes detected in cavities $p_0 \div p_5$ as a function of the elongation parameter $p$ . . . . .	55

3.19	Structure $b_4$ , cavity $p_3$ . Polarization dependance of the resonant modes. $0^\circ$ corresponds to the y-axis direction. Figure also shows mode profiles ( $B_z$ component), polarization ( $\vec{E}$ ) and position in the spectrum of the LQ and HQ modes, the result of 3-D FDTD analysis. . . . .	57
3.20	Cavity $b_4$ , $p_5$ . L-L curve for two different duty cycles (DC). The pulse periodicity was $1\mu s$ in both cases. Spectra taken above threshold for $DC = 1\%$ (red) and below threshold for $DC = 3\%$ (black arrow) are shown as insets. (b) Wavelength chirp in case of $DC = 3\%$ . . . . .	58
3.21	Cavity $b_4$ . L-L curves for structures $p_5$ and $p_4$ pumped with $DC = 1\%$ . Reduced differential quantum efficiency in the case of $p_4$ structure is due to the smaller Q factor. Spectra for $p_4$ structure, at and above threshold, are also shown. . . . .	60
3.22	Structure $b_1$ , cavity $p_5$ . Photoluminescence spectra taken at (a) low and (b) high pumping levels. Linewidth narrowing (HQ mode) and gain clamping can be observed. Q-factors of LQ mode are estimated to be around $Q_{LQ} = 505$ . . .	61
3.23	L-L curve of structure $b_1$ $p_5$ taken at different pumping levels. $DC = 1\%$ . . .	61
3.24	Structure $a_2$ $p_4$ . (a) L-L curve. Lasing action occurs from HQ mode positioned at $\lambda = 1598$ nm. Insets show spectrum above threshold, and mode profiles of the lasing mode for several pump levels. The boundaries of the structure can also be seen. The mode is very well localized to the center of the cavity. (b) Tuning properties of $a_2$ structure, as a function of the elongation parameter $p$ . . . . .	62
3.25	Scanning electron micrograph and calculated field distribution of a photonic nanocavity laser sensor. . . . .	64
3.26	SEM micrograph of structures B: $r_2c_5$ (a, b) and C: $r_5c_2$ small (c) after reactive ion etching using PMMA as the mask and $CHF_3$ as the reactive gas. . . . .	65
3.27	SEM micrograph of high-Q planar photonic crystal cavity, defined in the suspended membrane. . . . .	66
3.28	Membrane not completely released from the substrate. The light gray region at the bottom and top of the figure, as well as the diagonal line at the left side of the figure are regions where sacrificial InP was not completely removed. Q-factors can be spoiled significantly if non-undercut region is close to the cavity region. . . . .	67

3.29	Pattern recognition. (a) SEM micrograph of one of the structures. (b) Blow-up of the region indicated by square. Edges of the holes detected in this step are shown in red. (c) Detected holes are shown in white and their area is calculated and used to estimate (d) the radius of each hole. . . . .	68
3.30	(a) Sensor response measured from 6 nanocavities with a lattice parameter of $a = 446$ nm (dashed lines) and $a = 460$ nm (solid lines) as a function of $p/a$ dislocation parameter. The three curves correspond to the laser wavelength with air, methanol and IPA backfilled into the cavity. (b) Spectrum change and (c) threshold curve change of laser before and after filling with IPA. . . .	71
3.31	Dependence of (a) $a/\lambda$ and (b) $\lambda$ of HQ mode on refractive index of the environment ( $n_{env}$ ). Three different cavities, labelled $R_6C_5$ , $R_7C_5$ and $R_7C_3$ , were tested. . . . .	72
3.32	(a) Fabricated structure consists of three cavities integrated within the same photonic crystal mirror. Defect holes are indicated by arrows, and their size increases from right to left. (b) Resonances detected in each cavity. Mode experience blue-shift as the size of defect hole increases. Positions of pump-beam are shown. . . . .	74
3.33	Simultaneous emission from two adjacent nano-lasers pumped simultaneously using big pump spot. Insets show near-field image of the light emitted from nanolasers. . . . .	75
4.1	Schematic of the single line defect waveguide. Unit cell and boundary conditions used in the FDTD calculation are indicated. . . . .	80
4.2	(a) Cross section of the fabricated square lattice waveguide suspended in the air and (b) schematic of the waveguide viewed end-on. Reflection symmetry planes are $\sigma_{xy}$ in the middle of the slab (vertical symmetry plane), and $\sigma_{yz}$ in the center of the waveguide (lateral symmetry plane). . . . .	81

4.3	Dispersion diagram for (a) vertically even (TE-like) and (b) vertically odd (TM-like) guided modes in the square lattice waveguide. Symmetry of the modes with respect to the lateral symmetry plane ( $\sigma_{yz}$ ) is indicated. Modes are labeled $e_1 - e_4$ for vertically even case, and $o_1 - o_2$ for vertically odd case. Characteristic high symmetry points are also shown (dielectric band only). Insets show field patterns of (a) $B_z$ and (b) $E_z$ components in the middle of the slab (z-slice) for different guided modes. In the case of TM-like guided modes ( $o_1$ and $o_2$ ), distribution of $E_z$ component along the cross section of the waveguide is shown, as well. . . . .	83
4.4	Dispersion diagram for (a) vertically even (TE-like) and (b) vertically odd (TM-like) guided modes in the waveguide based on the triangular PC lattice. Insets show field patterns of (a) $B_z$ and (b) $E_z$ components in the middle of the slab (z-slice). In the case of TM-like modes ( $o_1$ , $o_2$ ), distribution of $E_z$ component along the cross section of the waveguide ( $\sigma_{xz}$ plane) is shown. Note that the cross sections for $o_1$ and $o_2$ modes are taken at different positions along the waveguide. Field profile for $o_2$ is taken near the cut-off and therefore the field penetrates the photonic crystal, as can be seen in the inset. . . . .	85
4.5	Distribution of the $B_z$ component of the field along the cross section of the <b>square</b> lattice based waveguide ( $\sigma_{xz}$ plane) for different guided modes. Labeling is (mode, $k_y \cdot \frac{a}{\pi}$ , $a/\lambda$ ). (a) ( $e_1, 15/24, 0.173$ ), (b) ( $e_2, 22/24, 0.320$ ), (c) ( $e_3, 22/24, 0.395$ ) and (d) ( $e_4, 22/24, 0.404$ ). It can be seen that all the modes are fundamental in the vertical direction. The core of the waveguide appears as the rectangle in the center of the figure. . . . .	86
4.6	Distribution of the $B_z$ component of the field along the cross section of the <b>triangular</b> lattice based waveguide ( $\sigma_{xz}$ plane) for different guided modes. (a) ( $e_1, 17/24, 0.191$ ), (b) ( $e_2, 24/24, 0.260$ ), (c) ( $e_4, 21/24, 0.346$ ) and (d) ( $e_5, 21/24, 0.382$ ). Again, all the modes are fundamental in the vertical direction. The core of the waveguide appears as the rectangle in the center of the figure. . . . .	87
4.7	The band diagram for the TE-like (vertically even) modes of the Si slab perforated with triangular lattice of air holes. Parameters used in analysis are $r = 0.3a$ (hole radius), $t = 0.55a$ (slab thickness), $n_{Si} = 3.5$ (refractive index of Si). . . . .	89

4.8	$\omega - \beta$ relation for the guided modes in the single line defect waveguide <i>type 0</i> for (a) $r/a = 0.3$ and (b) $r/a = 0.4$ . The straight solid line represents the light line. The modes above the light line, in the light gray region, will leak energy into the air (leaky modes). The dark gray areas are the regions where extended states of the PPC slab exist. Guiding can occur in the white regions.	91
4.9	Different type of waveguides. By moving the PPC mirrors that surround the single line defect waveguide (a) along the direction indicated by arrows ( $\Gamma X$ direction) we can form a <i>type 1</i> waveguide (b). (c) Unperturbed PPC lattice. If we offset the black holes along the $\Gamma J$ direction (as indicated by arrow) for the amount $d$ , we can form a (d) new type of waveguide ( <i>type 2</i> ). By controlling the parameter $d$ , we can control the positions of the guided modes of the structure. . . . .	93
4.10	Dispersion relations for the guided modes of the <i>type 1</i> and <i>type 2</i> waveguides for different values of controlling parameters ( $M$ and $d$ respectively). Arrows indicate the positions of the modes as we change the controlling parameters. (a) <i>Type 1</i> waveguide. The width of the waveguide (center-to-center distance between two holes adjacent to the waveguide) is defined as $a \cdot \sqrt{3}/2 \cdot (1 + M/6)$ . $M=6$ yields a single line defect waveguide. (b) <i>Type 2</i> waveguide. Position of the modes as a function of the parameter $d$ - offset along the $\Gamma J$ direction. . . . .	95
4.11	(a), (b) Field pattern of the <i>mode 1</i> in the <i>type 1</i> waveguide for $M = 5$ . (c), (d) Field pattern of the <i>mode 1</i> in the <i>type 2</i> waveguide, for $d = 0.5a$ . (a) and (c) show field profiles at the middle of the slab, and (b) and (d) at the positions indicated by dashed lines in the (a) and (c) respectively. The intensity bar is also shown. Field patterns are shown for $\beta = \pi/a$ . . . . .	96
4.12	Electric field pattern at X point in the unperturbed PPC in the case of (a) dielectric and (b) air band. (c) Black holes - new type of waveguide (for $d = 0.5a$ ). Black holes at the LHS and open holes at the RHS represent positions of the holes in the unperturbed PPC. The regions where air replaces dielectric (A) and vice versa (B) as we move holes around (black holes at the RHS) are also indicated. . . . .	97

4.13	(a) SEM micrograph of the fabricated <i>type 3</i> waveguide, formed by increasing the size of the holes adjacent to the single line defect waveguide. (b) and (c) Dispersion relations - position of the laterally (a) even, and (b) laterally odd modes as the function of the size of the holes adjacent to the waveguide. . . .	100
4.14	Dispersion relation for the guided modes in the (a) <i>type 4</i> and (b) <i>type 5</i> waveguides, as the function of the radius of the <i>defect</i> holes ( $r_{defect}$ ). Arrows indicate positions of the modes for different values of $r_{defect}$ . SEM micrographs of the fabricated structures are shown in the insets. (c) Dispersion diagram for TM-like guided modes supported in <i>type 4</i> and <i>type 5</i> waveguides. . . . .	101
4.15	(a), (b) Field patterns of the <i>mode 1</i> in the <i>type 4</i> waveguide with $r_{defect} = 0.2a$ . (c), (d) Field patterns of the guided mode in the <i>type 5</i> waveguide with $r_{defect} = 0.45a$ . (a) and (c) show field profiles at the middle of the slab, and (b) and (d) at the positions indicated by dashed lines in the (a) and (c), respectively. Field patterns are shown for $\beta = \pi/a$ . . . . .	103
4.16	(a) Waveguide with two 60 bends and $25\mu m$ bend-to-bend spacing. (b) High Q cavity filter formed by coupling single defect cavity to the two waveguide sections. . . . .	104
4.17	Fabrication procedure: 1) oxidation and 2) HF dip in order to define the thickness of the Si slab; 3) deposition of PMMA and 4) electron-beam lithography to define patterns in PMMA; 5) CAIBE to transfer patterns into silicon; 6) removal of PMMA and thinning of the substrate; 7) HF dip to remove SiO <sub>2</sub> layer underneath the waveguide in order to improve the vertical confinement of light. . . . .	106
4.18	(a) SEM micrograph of the $90^\circ$ bend in the square lattice after CAIBE. (b) SEM micrograph of the cross section of the square lattice waveguide. Layers top-down are Si slab ( $280nm$ ), SiO <sub>2</sub> ( $340nm$ ) and Si substrate. The lattice constant is $a \approx 500nm$ and the hole radius $r \approx 200nm$ . . . . .	107
4.19	(a) SEM micrograph of the cross section of the triangular structure waveguide suspended in the air. Layers top-down are Si slab/ air/ Si substrate. (b) SEM micrograph of $60^\circ$ bend in the triangular lattice. Area that is undercut extends about $1\mu m$ around the waveguide. Parameters of the fabricated structure are $a \approx 530nm$ , $r \approx 208nm$ and $d \approx 300nm$ . . . . .	108

4.20	Experimental setup for characterization of PPC waveguides. . . . .	110
4.21	Light guided in the waveguide around two 90 bends (top view). It can be seen that the light is confined to the waveguide (upper right inset). Inset in the lower right corner shows the SEM micrograph of the corner design in the square lattice. Visualization of light propagation is made possible by coupling intentionally to leaky modes which radiate from the top surface of the guide. Enhanced losses for these modes can be seen at the sharp bends. . . . .	112
4.22	Visualization of light guided in the triangular lattice single line defect waveguide around $60^\circ$ bend in the case of (a) simple corner design and (b) corner with cavity. . . . .	113
4.23	Waveguiding at $\lambda = 1550\text{nm}$ around a $60^\circ$ bend. Two cameras are used simultaneously, a top (camera No.1) and in-plane view (camera No.2) of the tested structure. (a) When input fiber is aligned to the input of the waveguide, an output signal, transmitted around $60^\circ$ bend is detected (signal B) and (b) when it is misaligned a transmitted signal is not present. The position of the slab is indicated with two parallel lines. (c) Detected output power (arbitrary units) at different positions along the cleaved output facet of the waveguide. Two peaks correspond to the signals A and B. The figure is obtained as a line scan of the Figure 4(a) along the middle of the slab. . . . .	115
4.24	Experimental setup. The structure that we have characterized is a single line defect waveguide with a single defect cavity in it. $L \approx 122\mu\text{m}$ . . . . .	117
4.25	Formation of the standing wave in the numerical model of our experiment. Waveguides, closed with cavities at one side, are excited with dipole sources at the entrance of the waveguide (left-hand side). . . . .	118
4.26	Wavelength dependence of the signal scattered in the vertical direction, detected by the camera. Periodic intensity modulation can be observed for all wavelengths except for $\lambda \in (1490\text{nm}, 1510\text{nm})$ . Periodicity of this modulation grows shorter as the difference between the wavelength and $1500\text{nm}$ grows larger, in either direction of the wavelength. An optical microscope image of the structure is also shown. $L = 122\mu\text{m}$ . . . . .	119

4.27	Experimentally mapped dispersion diagram of the leaky TE-like modes supported in the waveguide, overlaid onto the calculated diagram (black solid lines). Frequency range probed in the experiment is shown in blue. The light-blue pixels represent the spatial frequencies ( $\beta$ ) detected in the spectrum of the periodic intensity modulation pattern recorded by the camera. Insets show mode profiles ( $B_z$ ) for the two modes of interest. The light line is represented by the straight solid line, the leaky-modes region in light-gray, and the extended states of photonic crystal in dark-gray. . . . .	121
4.28	Standing wave formed in a waveguide with bend. (a) Experiment and (b) 3-D FDTD simulation. . . . .	123
4.29	(a) Signal detected with the camera, and (b) light intensity in the waveguide normalized to the intensity at the input - line scans across the data shown in (a). Radiation losses can be seen to increase as the wavelength departs from the mini stop band centered around 1500nm. . . . .	125
4.30	(a) Field profile ( $B_z$ taken at the middle of the slab) of a leaky mode excited in the waveguide. (b) $P_z$ component of the Poynting vector, at a distance of about $1\mu m$ from the top surface of the structure, shown for three different frequencies. Periodic intensity modulation can be observed. (c) Profile of $B_z$ component taken at the center of the waveguide (envelop is shown in red). Beating between two Bloch components and signal attenuation along the waveguide can be seen. (d) Spatial frequency spectrum of the signal shown in (c). Most of the mode energy is stored in the component at $k_2$ since its intensity is almost 10 times greater than the one at $k_1$ . The light cone is represented in gray. . . . .	126
4.31	Dispersion diagram of the TE-like guided modes supported in the triangular lattice PPC waveguide. The light cone is shown in light-gray and the extended states of the surrounding PPC (projected along $\Gamma J$ direction) in dark-gray. . . . .	127

# List of Tables

2.1	Design parameters of the photonic crystal used in order to have the bandgap centered around $\lambda = 1.5\mu m$ . . . . .	14
3.1	Applications of high-Q cavities . . . . .	42
3.2	InGaAsP wafer structure . . . . .	44
3.3	Process parameters for fabrication of the first generation samples . . . . .	48
3.4	Geometry of four nano-lasers tested in the experiment . . . . .	51
4.1	The structure of SOI wafer . . . . .	104
4.2	Waveguide losses of the leaky $e_1$ mode of the PPC waveguide . . . . .	129

# Chapter 1

## Introduction

*Photonics* has recently become an attractive alternative to electronics technology owing to advantages offered by information processing in the optical domain. For example, devices that are using a *photon* rather than an *electron* as an information carrier can benefit from the high speed of optical signals, reduced cross-talks between the channels, etc. Because of that, recently we have witnessed an increased interest in compact optical components like resonators, waveguides, etc. At the same time, nanotechnology and nanofabrication have recently emerged as a powerful technology that offers an opportunity to create nanoscale structures in a reproducible and controllable manner. The technology that was driven by the ever-growing need to shrink the sizes of electronic chips has now evolved to a precision which allows us to control the flow of photons within structures nanofabricated in standard electronic semiconductor materials. By combining the need for integrated photonics with the promise of nanofabrication technology, a field of *Nanophotonics* has emerged. The optical systems that have traditionally been made in silica, for example, can now be scaled down and fabricated in conventional microelectronics materials (silicon, GaAs, etc.). These ultra-small optical systems, defined in high refractive index contrast platforms, can be highly integrated, thus realizing for the first time the dream of large-scale integrated all-optical systems for information processing. In addition, since nanophotonic systems are realized in standard electronic materials they can be integrated with electronic components resulting in hybrid systems of higher complexity. On the other hand, nanoscale photonic structures offer a great promise for the investigation of fundamental physical laws that govern the behavior of photons. Strong coupling between light and matter, efficient control of spontaneous emission and enhanced nonlinear phenomena, are some of the interesting phenomena that can be observed when light and matter interact on a nanoscale level. Nanophotonics

also offers advantages for biochemical sensing on a nano-scale.

## 1.1 Photonic Crystals

The *photonic crystal*<sup>1-4</sup> (PC) is one of the platforms that can enable the miniaturization of photonic devices and their large-scale integration. These man-made periodic nano-structures can be designed to form frequency bands (photonic bandgaps) within which the propagation of electromagnetic waves is forbidden irrespective of the propagation direction. Depending on the dimensionality of spatial periodicity, we distinguish between several different classes of photonic crystals. One-dimensional photonic crystals are well-known dielectric stacks. For example, in Figure 1.1(a) we show a vertical cavity surface emitting laser<sup>5</sup> (VCSEL) that utilizes Bragg mirrors to achieve light localization in the vertical direction. If the periodicity is two-dimensional (2-D), we talk about 2-D photonic crystals. Strictly speaking, these structures are assumed to be infinitely long in the direction perpendicular to the plane in which 2-D periodicity exists. Even though there was a lot of reports on theoretical investigation of these structures, they show little practical promise for nanophotonics applications since only finite height structures can be fabricated. One of the most promising applications of 2-D PCs is photonic crystal fiber,<sup>6</sup> shown in Figure 1.1(b). In such a structure, light is confined to the core by the photonic band gap (PBG), and propagates down the fiber, along the PC holes. By making the spatial periodicity in three dimensions, *real* three-dimensional (3-D) photonic crystals<sup>7</sup> can be realized [Figure 1.1(c)]. 3-D PCs can have complete bandgap, and therefore can control propagation of light in all directions. These structures can be realized using standard top-down etching techniques, multiple thin-film deposition techniques, self-assembly, micromanipulation, etc.

Fabrication of 3-D PC structures is still a difficult process, and a more appealing approach is based on the use of lower-dimensional photonic crystals. A structure that has recently attracted a lot of attention is a semiconductor slab perforated with 2-D lattice of holes<sup>8,9</sup> (Figure 1.2). The big advantage of these *planar* photonic crystals (PPC) is their fabrication procedure, which is compatible with standard planar technology used to realize micro-electronic systems. *Lithographic tunability* is another great advantage of PPC

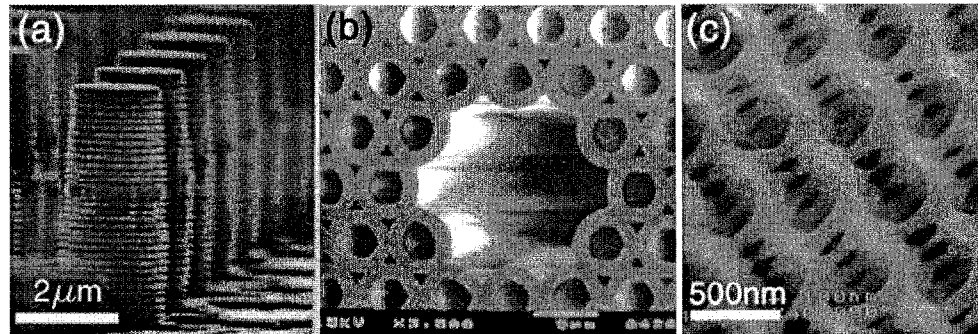


Figure 1.1: Photonic crystals of different dimensionality (a) 1-D: Bragg mirror (after A. Scherer<sup>5</sup>), (b) 2-D: Microstructured fiber (after R. F. Cregan<sup>6</sup>) (c) 3-D: Yablanovite structure (after C. C. Chen<sup>7</sup>).

concept - for example lasers that operate at different wavelengths can be monolithically integrated within the same semiconductor slab, and the tuning of the lasing wavelength can be achieved by changing the periodicity of the structure.<sup>10</sup> The size of nanophotonic devices based on the PPC concept is comparable to the wavelength of the light in the material and therefore it is possible to realize functional photonics components that are at least an order of magnitude smaller than conventional structures. Therefore, planar photonic crystal devices offer a promise to replace conventional photonics components in highly integrated optical systems. PPCs show even greater promise for realization of devices that cannot be made using a conventional approach. For example, highly dispersive prisms<sup>11</sup> (*super-prisms*) and self-collimators, discussed in Chapter 2, are some of the examples. However, the most attractive planar photonic crystal device might be a compact and efficient *nanocavity* (Chapter 3). This is due to extraordinary feature of PPCs to localize high electromagnetic fields in very small volumes, for a long period of time. In addition to many advantages, photonic crystals have some disadvantages and challenges that still need to be addressed. For example, electrical pumping of photonic crystal nanolasers still remains to be solved and power emitted from these structures is tiny. Also, present state-of-the-art PPC waveguides (Chapter 4) are still inferior to the conventional waveguides, and their propagation losses are at least an order of magnitude higher than losses in conventional devices.

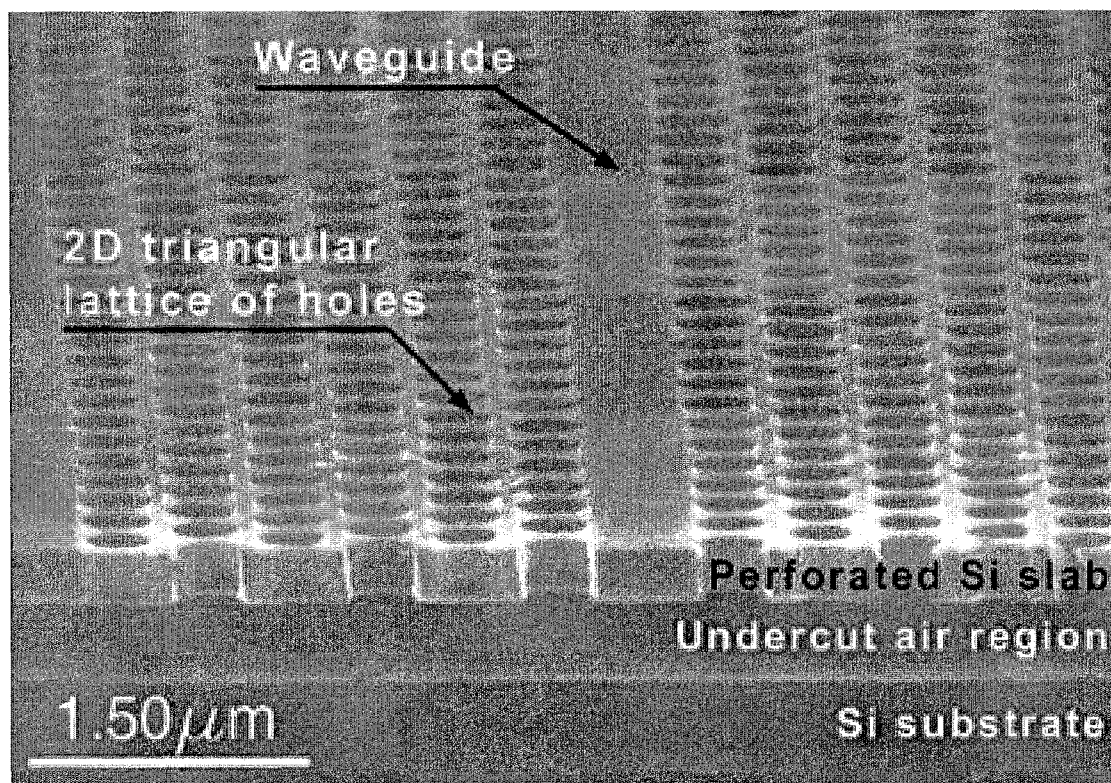


Figure 1.2: SEM micrograph of a planar photonic crystal waveguide fabricated in SOI wafer.

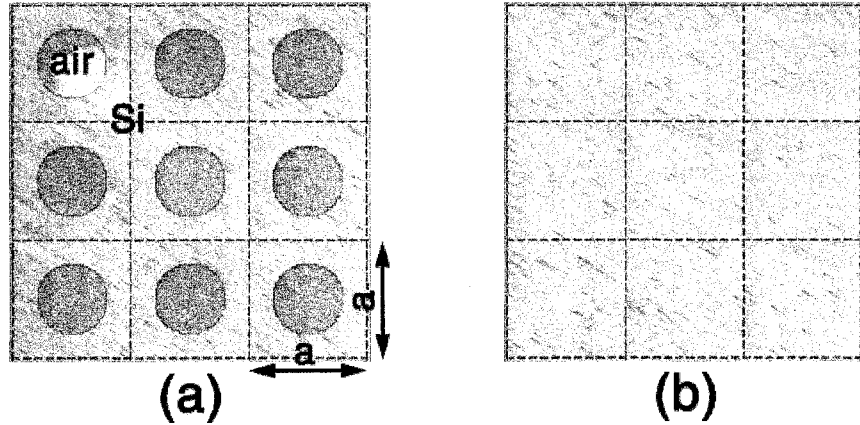


Figure 1.3: (a) Square lattice photonic crystal. (b) Si block, without air holes.

## 1.2 The Origin of The Photonic Band-Gap

The study of photonic crystals, and periodic dielectric structures in general, has a lot of analogy with the study of solid-state physics and semiconductor materials. As it is well known, the periodicity of electronic potential in semiconductor materials, due to the regular arrangement of atoms in a crystal lattice, results in the existence of the forbidden energy bands for electrons, the electronic bandgap. Similarly, the periodicity of a *dielectric* lattice of photonic crystals results in the photonics-bandgap, forbidden energy bands for photons. Therefore, photonic crystals are sometimes called *semiconductor for light*. The existence of the photonic bandgap in photonic crystals will be explained on the example of a 2-D photonic crystal based on a Si block perforated with a square lattice of air holes [Figure 1.3(a)].

Dispersion relation of pure Si block, shown in Figure 1.3(b), can be expressed as

$$\omega = k \cdot \frac{c_0}{n_{si}}, \quad (1.1)$$

where  $\omega$  is the frequency of light,  $k$  propagation constant,  $c_0$  speed of light in air and  $n_{si}$  refractive index of silicon. Assuming the *artificial* periodicity of the *Si* block, with periodicity  $a$ , the light line equation can be written in the normalized form common for

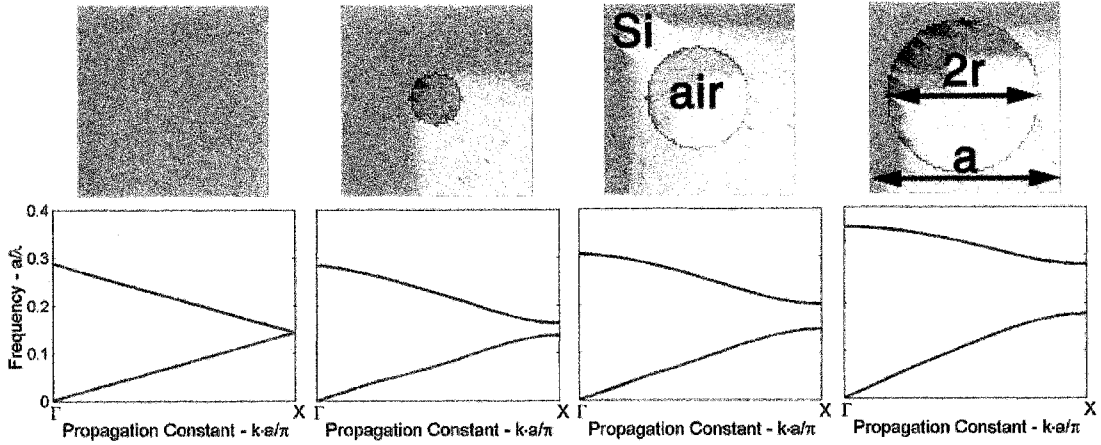


Figure 1.4: Dispersion diagrams for light propagating along the x-axis direction for various sizes of air holes in Si block. Normalized frequency in units  $a/\lambda = \omega a/2\pi c$  is shown on the y-axis and normalized propagation constant on the x-axis.

photonic crystals:

$$\frac{\omega a}{2\pi c_0} = \frac{1}{2n_{si}} \cdot \frac{ka}{\pi}. \quad (1.2)$$

This dispersion relation is shown in the first panel in Figure 1.4. The light line is shown in the *reduced scheme*, and is *artificially* folded back into the first Brillouin zone, assuming the artificial periodicity of the Si block.

By adding periodic lattice of holes into this Si block, dispersion is modified and the bandgap opens at the edge of the Brillouin zone. The evolution of the dispersion diagram, obtained using finite-difference time-domain calculations<sup>12</sup> (FDTD), is shown in Figure 1.4. As holes become bigger, the bandgap becomes wider and shifts towards higher frequencies. The latter can be attributed to the increased overlap between light and low-dielectric constant material (air) as holes becomes bigger.<sup>3</sup>

The mode profiles of two bands taken at the end of Brillouin zone ( $ka/\pi = 1$ ) are shown in Figure 1.5. It can be seen that the two modes have the same symmetry but they localize the energy in materials with a different dielectric constant. Because of that, they will have different eigen frequencies and the bandgap will open. Therefore, we conclude that the photonic bandgap is open due to periodicity and symmetry of the photonic crystal lattice.

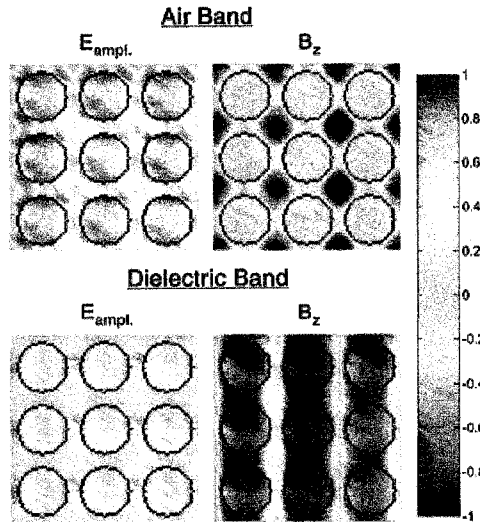


Figure 1.5: The field profiles of dielectric and air band. It can be seen that light is concentrated in the Si in the case of then dielectric band, and in the air hole region in the case of the air band.

So far we were concerned with light propagating along the x-axis direction only. For complete analysis of optical properties of uniform, un-patterned material (e.g., *Si* block), it is sufficient to study light propagation along one spatial direction only, since all directions are equivalent. This is not the case when studying multi-dimensional periodic dielectric lattices. The introduction of a periodic lattice reduces the symmetry of the system, and it becomes necessary to study light propagation along various directions in order to describe the optical properties of patterned media. Fortunately, as in the case of electronic bandgap, it is sufficient to study light propagation along high symmetry directions of the periodic photonic crystal lattice, only.<sup>13</sup> In the case of square lattice, these directions are labelled  $\Gamma X$ ,  $XM$  and  $\Gamma M$ . In Figure 1.6 we show the dispersion diagram for the modes propagating in 2-D square lattice photonic crystal. It can be seen that a complete bandgap exists between  $M$  point in the dielectric band and  $X$  point in the air band, and that it is narrower than the stop-band calculated along the  $\Gamma X$  direction (Figure 1.4).

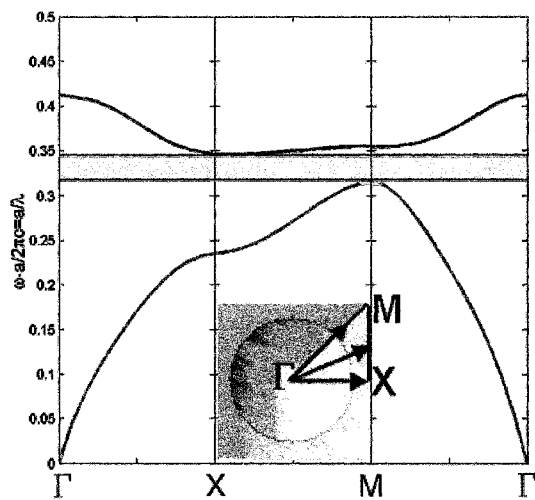


Figure 1.6: Band diagram calculated along high symmetry directions in 2-D photonic crystal lattice of square symmetry. The position of the first-order bandgap is indicated. The schematic of the irreducible first Brillouin zone is shown in the inset, along with the position of high symmetry points.

## Chapter 2

# Photonic Crystal Slabs

### 2.1 Introduction

In Chapter 1 we studied two-dimensional photonic crystals based on a square lattice, and we showed that there exists a frequency range in which the propagation of light is forbidden in any in-plane direction\*. While the theoretical treatment of 2-D photonic crystals is relatively easy, their fabrication procedure is not straightforward since they are infinite structures in the third dimension. Therefore, the concept of a planar photonic crystal was proposed to overcome this obstacle.<sup>8</sup> Planar photonic crystal is essentially a 2-D photonic crystal with a finite third dimension. One typical example is a membrane based photonic crystal shown in Figure 2.1. An optically thin semiconductor slab (thickness is roughly  $\lambda/2$ ) is surrounded with a low-refractive index material (usually air), and perforated with a 2-D lattice of holes. In such a structure, the localization of light in all three dimensions is made possible by the combination of two mechanisms: in the vertical direction, light is confined to the slab by means of total internal reflection (TIR) due to the **high index** contrast between the high-index slab and the low-index environment, while in the lateral direction light is controlled by means of distributed Bragg reflection due to the presence of 2-D lattice of holes. Another important example of planar photonic crystal is the one based on the **low-index** contrast between the semiconductor-based core and cladding, as in the case of AlGaAs material.<sup>14</sup>

In the planar photonic crystal shown in Figure 2.1 the third dimension is not periodic nor

---

\*In-plane direction is defined as a direction within a plane perpendicular to the direction of air holes.

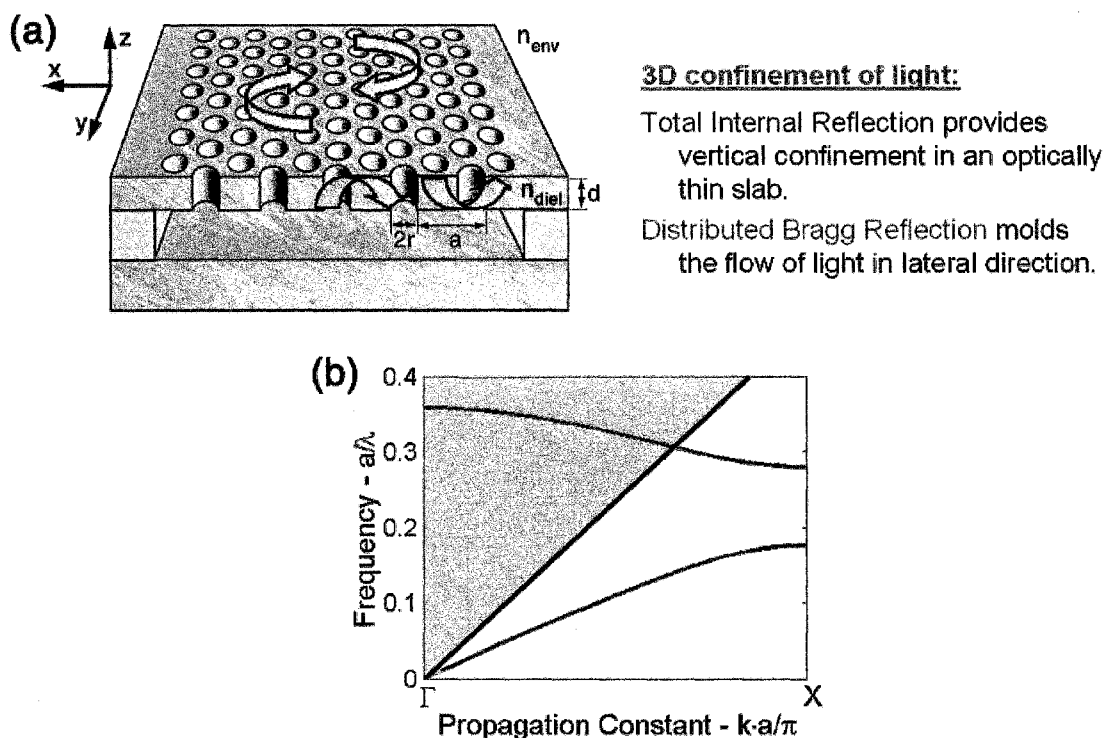


Figure 2.1: (a) Schematic of planar photonic crystal. Two mechanisms that make three-dimensional light localization possible are indicated. (b) Lightline (black solid line) and lightcone (gray region) overlaid on a dispersion diagram of the square lattice planar photonic crystal along the  $\Gamma X$  direction.

infinite, and therefore photons incident to the interface between the semiconductor slab and air with small angles (angles smaller than the critical angle for TIR) can escape from the slab and couple into the continuum of radiation modes. These photons leak energy from the slab and therefore represent the loss mechanism of the planar photonic crystal. In order to take these losses into account, we introduce the notion of the light cone (light line) in the analysis of PPCs. The region *above the lightline*, where the leaky modes exist, is represented in gray in Figure 2.1(b). Since radiative modes exist at all frequencies, including the bandgap region, they *close* the bandgap, and the complete bandgap does not exist in planar photonic crystals. The forbidden frequency range still exists, however, for the guided modes of the slab, that is for the photons confined in the patterned slab. Therefore, we conclude that in the case of planar photonic crystals, the bandgap is not complete and it exists only for the **guided modes** of the patterned slab. Because of that, any defects introduced into the photonic crystal lattice can couple the guided modes into the radiative modes and scatter light guided in the slab. These defects can be intentional, in the form of missing holes for example, or un-intentional, due to fabrication tolerances. Both of them will enhance coupling to the leaky modes and increase the losses of the PPC device. Therefore, care needs to be taken when designing and fabricating photonic crystals in order to minimize these losses. This is a very important issue and will be addressed in detail in Chapters 3 and 4.

In order to understand the operation of planar photonic crystals, full three-dimensional analysis is required since the waveguide incorporates the vertical confinement of light. In contrast to the infinite 2-D case, finite-thickness slabs can support modes with higher-order vertical oscillations, and, if the slab is made too thick, the presence of these modes can result in the closing of the bandgap. Therefore, the thickness of the slab is a critical parameter in this structure and needs to be modelled. 2-D analysis of vertically extended structure (infinitely thick slab) would result in band diagrams that are shifted toward the lower frequencies. The reason for that is that in the case of the slab waveguide guided modes are not completely confined in the slab, but also extend into the air. Therefore, the energy of the guided mode will be higher and the bands will be at higher frequencies than in the case of 2-D waveguide with infinitely long holes. This can be taken into account using the *effective refractive index* approach.<sup>15</sup> However, we find that an effective-index method can give good predictions for position of the band gap but it does not predict correctly the

shape of the bands in dispersion diagrams. Therefore, we have proposed an alternative 2-D method for the analysis of 3-D PPC structures, based on the use of frequency offsets.<sup>16</sup> The “effective” 2-D methods are very appealing, due to their simple implementation and less intense computational requirements, and are used by many groups. However, they are limited only to the phenomenological analysis of the properties of photonic crystals, and cannot be used in several important problems, like the analysis of the losses of waveguides and cavities.

The properties of planar photonic crystals, such as position and width of the bandgap, depend strongly on several important parameters: the type of lattice (e.g., triangular, square, honeycomb), the thickness of the slab ( $d$ ), the refractive index of both slab ( $n_{slab}$ ) and environment surrounding the slab ( $n_{env}$ ), the periodicity of the lattice ( $a$ ) and the size of the holes ( $r$ ). In the next two sections we will investigate the influence of these parameters on the properties of photonic crystal slabs.

## 2.2 Comparison between Square and Triangular Photonic Crystal Lattices

The structure that we analyze first is a silicon slab, suspended in the air, and patterned with square or triangular lattice of holes<sup>15,17,18</sup> (Figure 2.2). 3-D FDTD scheme was used to calculate the band diagrams. In both cases we analyzed a lattice unit cell by applying appropriate boundary conditions to its sides: Bloch boundary conditions to all four sides perpendicular to the plane of the slab, Mur’s Absorbing Boundary Conditions<sup>19</sup> (ABCs) to the top boundary, and mirror boundary condition at the middle of the slab. In that way we reduce the computation time by analyzing only one half of the unit cell. By changing the type of mirror symmetry we could select even (TE-like) or odd (TM-like) eigen modes of the photonic crystal structure. The spatial resolution that we used to discretize our structures was 20 computational points per lattice constant( $a = 20$ ). The thickness of the Si slab was  $d = 0.55a$  and hole radius was  $r = 0.4a$ . The index of refraction of Si is assumed to be  $n_{Si} = 3.5$ . Mur’s ABCs were applied at a distance of  $3 \cdot a = 60$  computational points away from the top surface of the slab, yielding the computation box of  $20 \cdot 20 \cdot 65$  cubical cells.

In the case of square PPC, lattice vectors are  $a_1 = a \cdot (1, 0, 0)$  and  $a_2 = a \cdot (0, 1, 0)$ , and

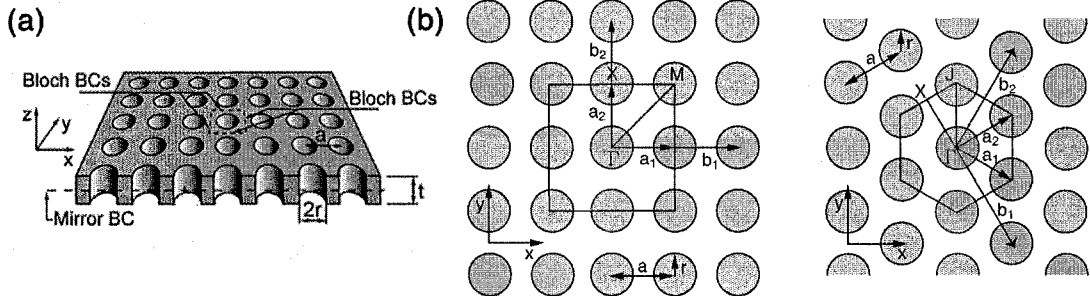


Figure 2.2: (a) Schematic view of the Si slab patterned with 2-D square lattice of holes. Unit cell of the PC and boundary conditions used in the 3-D FDTD calculation are also indicated. (b) Si slab perforated with 2-D square lattice of holes. Without loss of generality, lattice constant  $a$  in the figure is chosen to be  $a = \pi/a$  (dimensionless units), in order to conveniently show reciprocal lattice vectors. The square represents the first Brillouin zone, and  $\Gamma$ ,  $X$  and  $M$  are the high symmetry points. (c) Si slab perforated with 2-D triangular lattice of holes. This time we chose  $a = \frac{4\pi}{3a}$ . Hexagon represents the first Brillouin zone with high symmetry points indicated.

reciprocal lattice vectors are  $b_1 = 2\pi/a \cdot (1, 0, 0)$  and  $b_2 = 2\pi/a \cdot (0, 1, 0)$ . The square in Figure 2.2(b) represents the first Brillouin zone, and  $\Gamma$ ,  $X$  and  $M$  are the high symmetry points with coordinates (in reciprocal space):  $\Gamma = (0, 0, 0)$ ,  $X = (0, \pi/a, 0)$ ,  $M = (\pi/a, \pi/a, 0)$ . In the case of the triangular lattice PPC, lattice vectors in the real space can be expressed as  $a_1 = a \cdot (\sqrt{3}/2, -1/2, 0)$  and  $a_2 = a \cdot (\sqrt{3}/2, 1/2, 0)$ , and in the reciprocal space as  $b_1 = \frac{4\pi}{a\sqrt{3}} \cdot (1/2, -\sqrt{3}/2, 0)$  and  $b_2 = \frac{4\pi}{a\sqrt{3}} \cdot (1/2, \sqrt{3}/2, 0)$ . The hexagon in Figure 2.2(c) represents the first Brillouin zone, and the coordinates of high symmetry points are  $\Gamma = (0, 0, 0)$ ,  $X = \frac{2\pi}{a\sqrt{3}} \cdot (1/2, -\sqrt{3}/2, 0)$  and  $J = \frac{4\pi}{3a} \cdot (0, 1, 0)$ .

Band diagrams for the vertically even (TE-like) and odd (TM-like) eigen modes of the PPC structure with square and triangular symmetry are shown in Figure 2.3. As it can be seen, in both structures the first-order bandgap is open for the guided modes of the slab (modes below the light line) that have an even symmetry (TE-like). We again emphasize that the bandgap is formed only for the guided modes, as discussed above. The triangular lattice planar photonic crystal has a much wider bandgap than the square lattice, a result of the greater symmetry and the smoother Brillouin zone in that geometry. If we take into account fabrication tolerances (size and shape of the holes, thickness of the slab, etc.) it is possible that in the fabricated square lattice structure the bandgap will be closed. There-

Table 2.1: Design parameters of the photonic crystal used in order to have the bandgap centered around  $\lambda = 1.5\mu m$ .

lattice	PBG width	PBG position	midgap ( $f_0$ )	$a = f_0 \cdot \lambda$	$r$	$d$
square	0.031	(0.315, 0.346)	0.330	496nm	198nm	272nm
triangular	0.148	(0.291, 0.439)	0.365	547nm	219nm	301nm

fore, the triangular lattice is in many ways a more tolerant candidate for the realization of wide bandgap planar photonic crystal structures. However, in many cases it is not necessary, and sometimes is not even beneficial, to work with photonic crystals that have a wide bandgap, and thus allows for very strong light localization. This is most notable in the case of PPC cavities, and high quality factor cavity designs were realized even in square lattice PPC.<sup>20</sup>

In Table 2.1 we specify geometries of both square and triangular planar photonic crystals designed to operate at wavelength  $\lambda = 1.5\mu m$ .

## 2.3 Geometry-dependent Properties of Photonic Crystals

As we have seen in the previous section, properties of photonic crystals depend strongly on the lattice type. In this chapter we study the influence that hole size, thickness of the slab, refractive index of both slab and environment have on the properties of PPCs. A triangular lattice PPC is studied, but results can be generalized to the square lattice PPC as well.

### 2.3.1 Influence of the Hole Size

In Figure 2.4 we show band edges of the air and dielectric band calculated for various slab thicknesses and hole sizes. In panel (a) it can be seen that the bandgap becomes wider as the holes become bigger. Also, due to increased overlap with low-dielectric material (air), band edges are shifted towards higher frequencies when the hole size is increased. The air-band modes that localize their energy in the air-holes are more sensitive to changes in the hole size, and they experience larger blue-shift than the dielectric-band modes, when

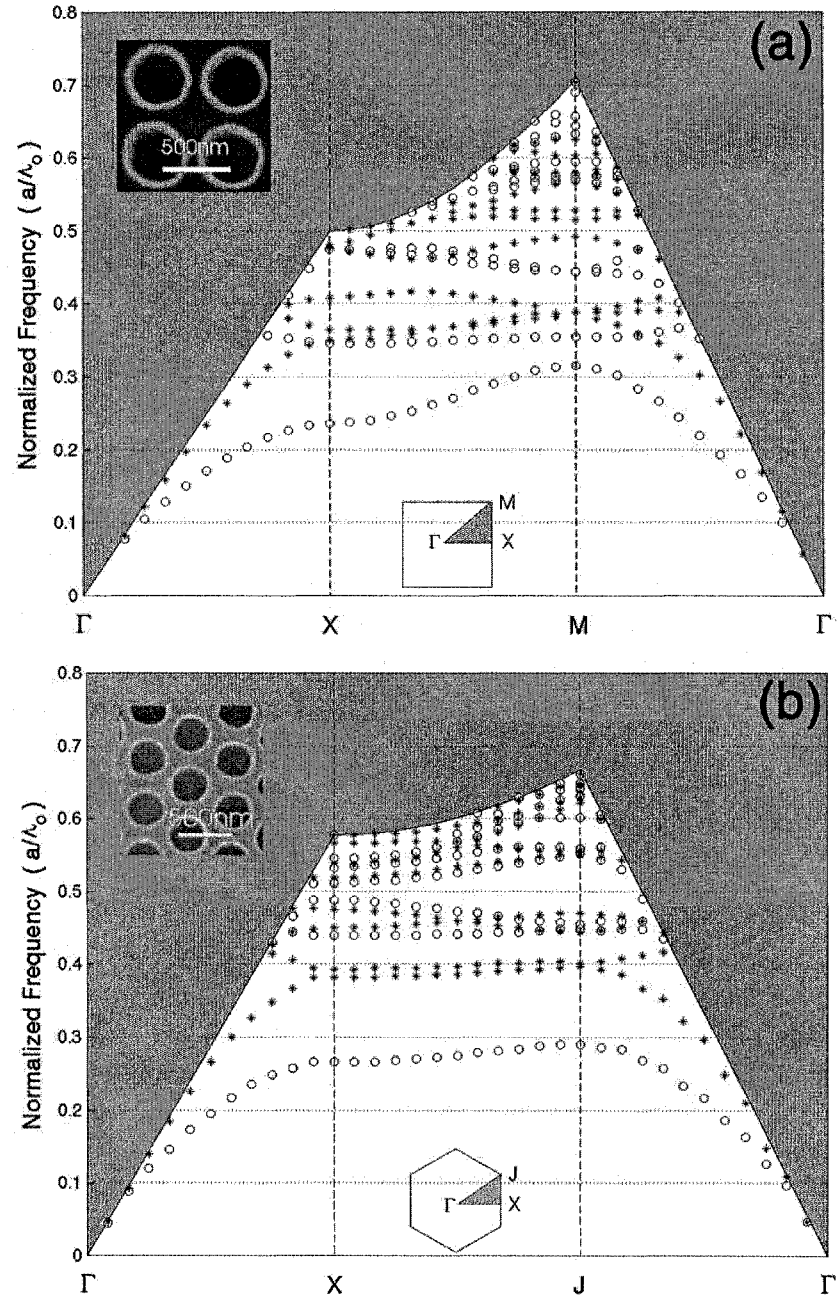


Figure 2.3: Band diagrams of eigen modes of Si slab perforated with 2-D lattice of holes of (a) square and (b) triangular symmetry. The x-axis represents different directions in the reciprocal lattice, and the y-axis normalized frequency in the units  $a/\lambda$ . The gray region represents the light cone. Even modes (TE-like) are represented with circles and odd (TM-like) with stars. Insets show the SEM micrographs of the fabricated photonic crystal structure, and the first Brillouin zones.

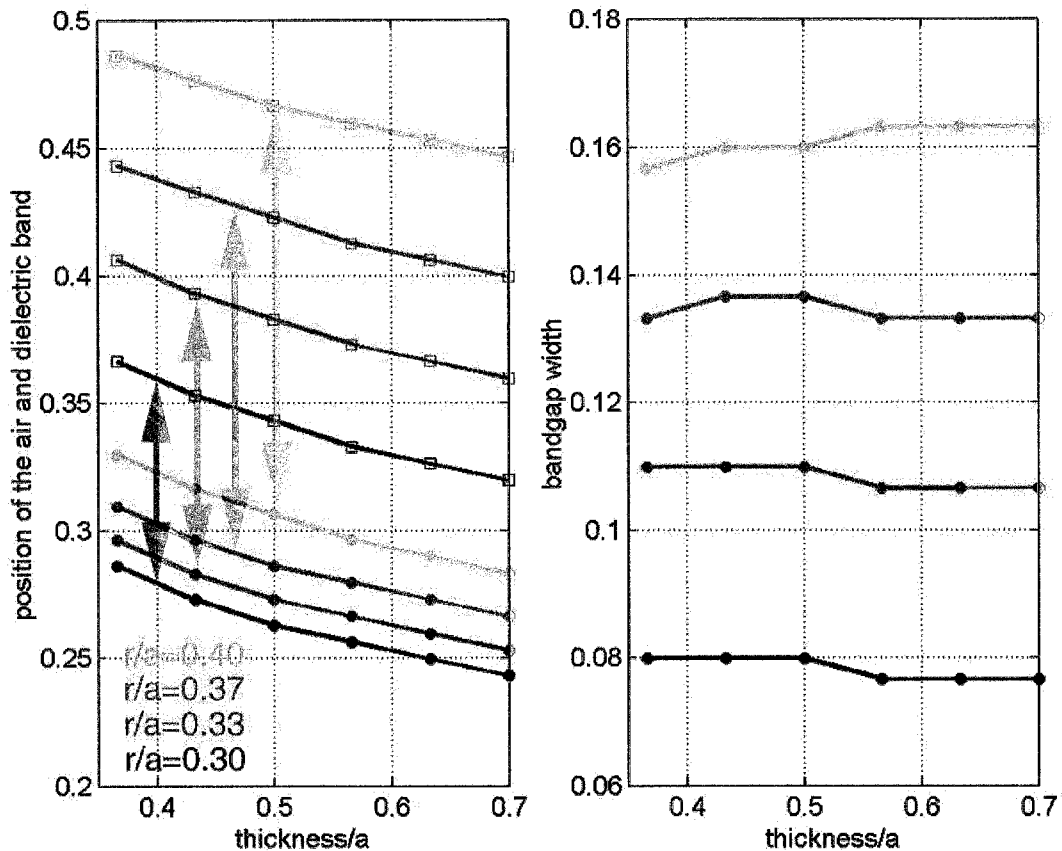


Figure 2.4: Bandgap position as a function of relative hole size ( $r/a$ ) and relative thickness of the slab ( $t/a$ ). (a) Positions of the band edges are shown: top of the dielectric band with full circles, and bottom of the air band with open squares. (b) The width of the bandgap for various geometries.  $n_{slab} = 3.5$  (Si) and  $n_{env.} = 1$  (air).

holes are made bigger. This results in widening of the photonics bandgap. When holes are made too big ( $r/a > 0.5$ ), the bandgap for TE-like modes can be closed and the bandgap for TM-like modes can be open.<sup>3</sup> On the other hand, when holes are too small the bandgap can also be closed, as we saw in Chapter 1. Slab thickness, in the range that we have explored, does not have strong influence on the width of the bandgap [Figure 2.4(b)], and it affects the position of the bandgap, only: due to reduced overlap with high-dielectric constant material, band-edges are shifted towards higher frequencies when the slab is made thinner.

### 2.3.2 Influence of the Refractive Index of Environment

In most common applications, planar photonic crystals are in the form of a free standing membrane suspended in the air. However, it is also of interest to explore the PPC properties when the air is replaced with material with a refractive index bigger than 1. For example, in Chapter 3 we will use PPC lasers as chemical sensors, and the operation of PPC membranes in chemicals with various refractive indices will be explored. Also, nanocavities based on PPCs can be backfilled with electro-optic or non-linear polymer, and their resonant frequency can be changed by applying strong electro-magnetic fields.

In Figure 2.5 we show the dependence of the dielectric-band and air-band edges when a PPC is immersed in materials with various refractive indices. The thickness of the PPC is  $d/a = 0.75$  and its refractive index  $n_{slab} = 3.4$ . The hole size is  $r/a \in \{0.3, 0.4\}$ . As expected, the band edges experience red-shift when the PPC slab is immersed in a material with higher refractive index. Also, the width of the bandgap decreases when  $n_{env.}$  increases. The reason is similar to decrease in the bandgap width when the holes of PPC are made smaller. The bottom of the air-band is more affected with increased  $n_{env.}$ , since air-band modes have larger spatial overlap with the environment. From Figure 2.5 we deduce that the bandgap will close when  $n_{env.} \approx 2$  in both structures. In the case of a crystal with  $r/a = 0.4$  the dependence of the band-edges on  $n_{env.}$  can be well approximated with

$$\left(\frac{a}{\lambda}\right)_{diel} = -0.0289 \cdot n_{env.} + 0.3255 \quad (2.1)$$

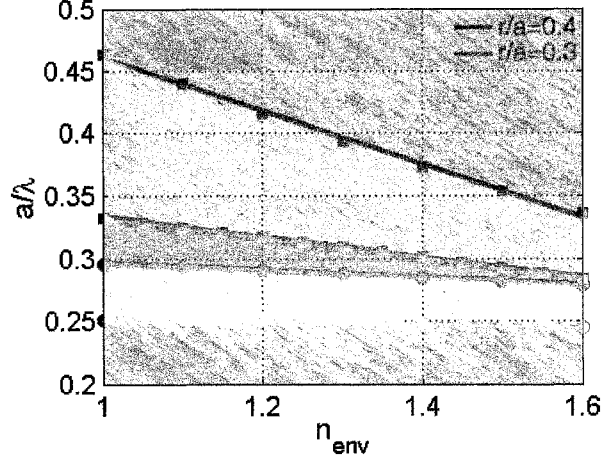


Figure 2.5: Air-band and dielectric-band edge dependence on the refractive index of environment ( $n_{env}$ ) surrounding PPC slab, for  $r/a = 0.3$  (red) and  $r/a = 0.4$  (blue).

$$\left(\frac{a}{\lambda}\right)_{air} = -0.2139 \cdot n_{env} + 0.6748. \quad (2.2)$$

When  $r/a = 0.3$  band-edges can be expressed as

$$\left(\frac{a}{\lambda}\right)_{dielectric} = -0.0104 \cdot n_{env} + 0.2621 \quad (2.3)$$

$$\left(\frac{a}{\lambda}\right)_{air} = -0.0812 \cdot n_{env} + 0.4144. \quad (2.4)$$

As expected, the structure with bigger holes is more sensitive to the changes in the refractive index of environment. From these equations we find that the sensitivity of the air-band edge is better than  $\Delta\lambda \approx 700 \cdot \Delta n$ , when  $r/a = 0.4$ . This suggests that by monitoring the shifts in the emission wavelength of a band-edge laser (that operates at the air-band edge) we could detect very small changes in the refractive index of the ambient. In Chapter 3 we will explore similar possibility but using confined cavity modes instead of extended band-edge modes.

### 2.3.3 Influence of the Refractive Index of the Slab

For some applications it is necessary to make PPCs in dielectric materials, that have a small refractive index. For example, if we want to make PPC devices that operate in the

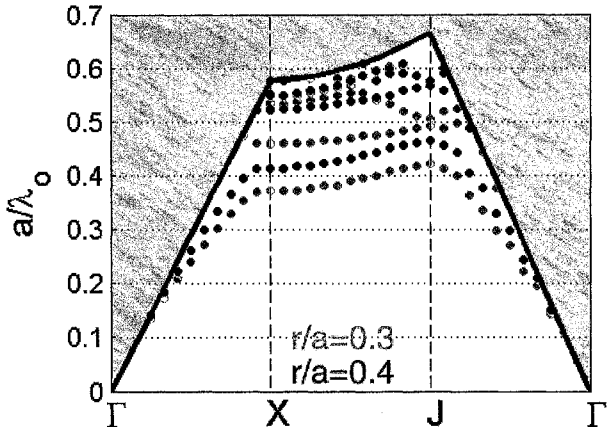


Figure 2.6: Band diagrams for PPC realized in  $\text{Si}_3\text{N}_4$  slab for two different hole sizes. Only TE-like modes are shown.

visible spectrum, we cannot use majority of semiconductor materials, due to their absorption in visible range. One promising candidate for PPCs that operate in the visible is silicon-nitride<sup>21</sup> ( $\text{Si}_3\text{N}_4$ ), with a refractive index of  $n_{\text{SiN}} \approx 2.02$ . In Figure 2.6 we show band diagrams for  $d/a = 0.55$ , and  $r/a = 0.3$  and  $r/a = 0.4$ . As expected, due to small refractive index contrast between core and environment, the band gap is narrow in these cases, particularly in the case of smaller holes.

## 2.4 Propagation of Light in Photonic Crystal Slabs

In previous sections we studied the existence of the bandgap in photonic crystals, and we investigated the influence of various design parameters on the position and width of the bandgap. This was an important task since in a majority of applications photonic crystals are used as *mirrors*, to confine light in space. However, by exciting the modes of photonic crystal with frequencies outside the photonic bandgap, light can propagate in the PPC. Then, due to strong dispersion of planar photonic crystals, phenomena associated with anomalous refraction of light like a *super-prism* and *self-collimation* can take place.<sup>16, 22–31</sup> In order to understand light propagation in patterned slabs, it is not sufficient to study

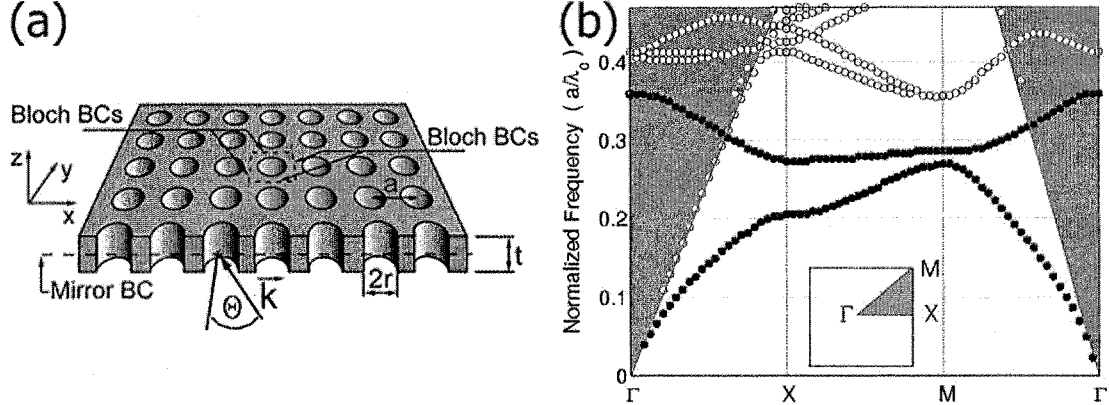


Figure 2.7: (a) Schematic view of the Si slab patterned with 2-D square lattice of holes. External light is incident to the slab at an angle  $\theta$ . Unit cell of the PC, with boundary conditions used in the 3-D FDTD calculation, is also indicated. (b) Band diagram for TE-like (vertically even) modes of the square lattice PPC. Grey region represents the light cone. Inset shows high symmetry points in the first Brillouin zone.

band diagrams along high-symmetry directions only, as it was done in previous sections, but a *complete band diagram* for all possible directions in the first Brillouin zone, needs to be investigated.

The planar photonic crystal that we study here is a silicon slab ( $n_{Si} = 3.5$ ) of thickness  $t = 0.57a$  and patterned with a 2-D square or triangular lattice of holes of radius  $r = 0.3a$ , where  $a$  is the periodicity of the lattice. The slab is surrounded by air on both sides. 3-D FDTD is used to calculate dispersion diagrams. The discretization used in our 3-D FDTD algorithm was  $a = 30$  computation points, this time. Better discretization in time and space in FDTD algorithm is needed in order to correctly predict the position and shape of the allowed bands of photonic crystal. We have analyzed only one half of the structure in the vertical direction, by applying mirror boundary condition at the center of the slab. Choosing the even mirror symmetry we analyzed TE-like (vertically even) modes only. Mur's absorbing boundary conditions were applied at 100 computational points away from the surface of the slab, yielding a computational domain of  $30 \cdot 30 \cdot 108$  cubic cells.

In Figure 2.7(b) we show a dispersion diagram of a square lattice PPC. The band diagram is calculated only along the high symmetry directions in the first Brillouin zone (BZ), and the light cone is represented by the gray region. Only the modes that lie outside the light cone are guided in the PPC without significant losses. We can see that this struc-

ture has a very narrow bandgap. However, the width of the bandgap is not what concerns us here. We instead hope to find unusual phenomena associated with the difference of the dispersion diagram of this structure from one of the unpatterned slabs. In order to do so, we have to find the *full* band diagram, for *all*  $k$  vectors in the I BZ, and not only along  $\Gamma X$ ,  $XM$  and  $\Gamma M$  directions.

Figure 2.8(a) shows such a dispersion diagram for the first two bands [black circles in the Figure 2.7(b)] for *all*  $k$  vectors in the I BZ. The band diagram was calculated from 325 equally spaced points in 1/8 of the I BZ [shaded region in the inset of the Figure 2.7(b)], the data were then fitted using polynomial of the fifth order, and finally mapped into the entire I BZ. The light cone is represented as unshaded mesh. From Figure 2.8(a) we conclude that Band 1 is below the light cone (guided) in the whole frequency range, while Band 2 is guided only for normalized frequencies  $a/\lambda < 0.306$ . Furthermore, Band 2 is almost flat and therefore light in that frequency range will be slowed down significantly. In Figure 2.8(b) and (c) we plot the equal-frequency contours for Band 1 and Band 2. The gradient of frequency change as a function of the in-plane  $k$  vector is indicated by vectors. Those vectors are oriented towards the  $\Gamma$  point in the case of Band 2 - an indication of the negative group velocity<sup>†</sup>. In addition, iso-frequency contours of Band 2 are almost perfect squares in the frequency range where Band 2 is guided. This is very different from the unpatterned Si slab, where iso-frequency contours of the guided modes are circles (Figure 2.9). This modification of the dispersion relation leads to very interesting, collimation-like effects, which we describe below.

#### 2.4.1 Self-collimation in Square Lattice PPCs

In Figure 2.10(a) we again show iso-frequency contours for Band 2, but this time only for frequencies that lie outside the light cone -  $a/\lambda \in (0.273, 0.306)$ . The light cone for  $a/\lambda = 0.306$  is represented with a dashed line. It can be seen that the equal frequency contours can be approximated by squares for  $a/\lambda \in (0.295, 0.306)$ . When the modes of the PPC are excited using an external light incident to the cleaved facet of the PPC [Figure

---

<sup>†</sup>Group velocity and phase velocity are oriented along opposite directions.

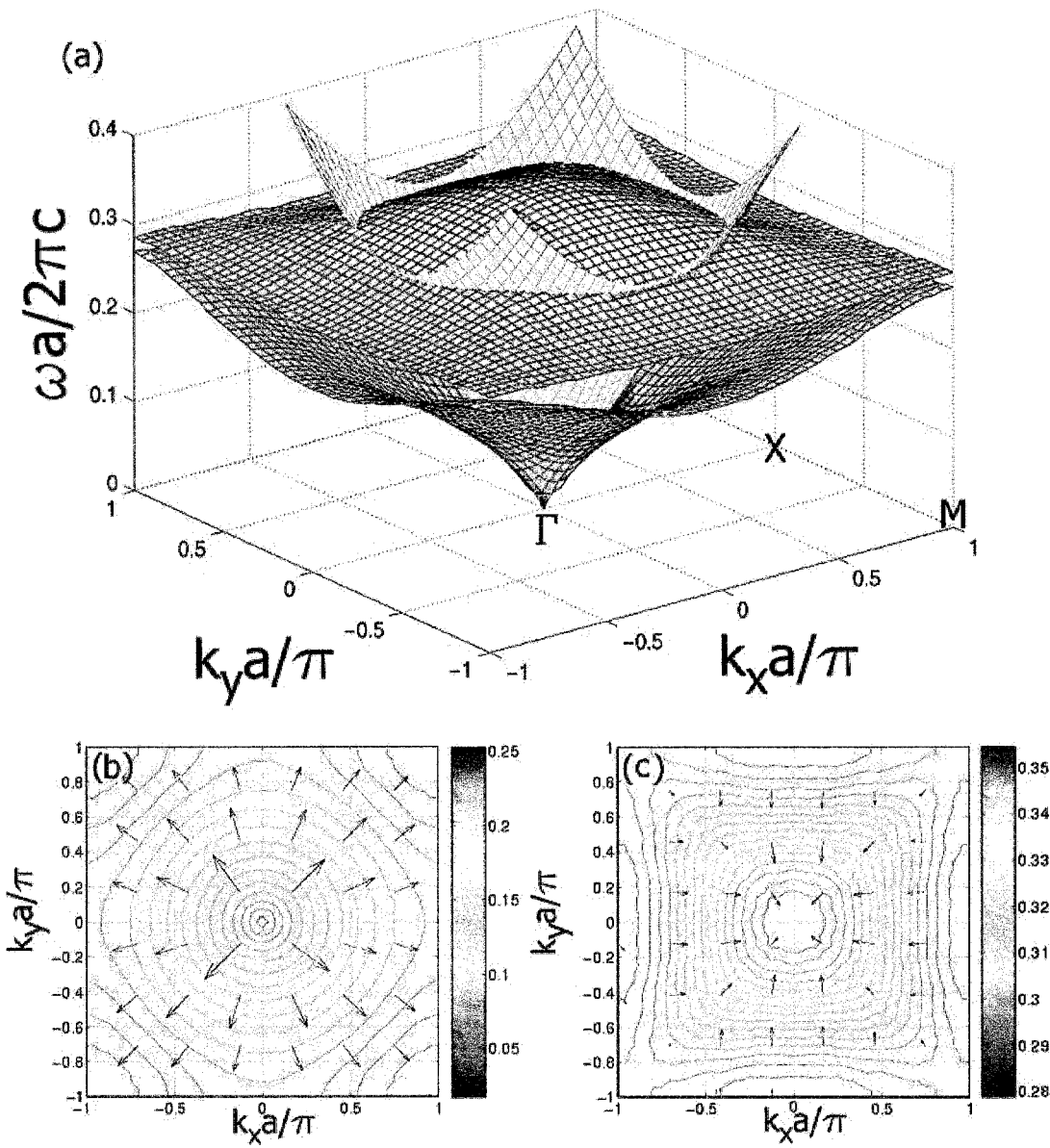


Figure 2.8: (a) The dispersion ( $\omega(k)$ ) relation for the first two bands of the square PPC, calculated for all  $k$  vectors in the first Brillouin zone. The light cone is represented as an unshaded mesh. (b) The iso-frequency contours for the first and (c) second band. The color represents different normalized frequencies -  $a/\lambda$ . The vectors represent the gradient of frequency change as the function of  $k_x$  and  $k_y$  components.

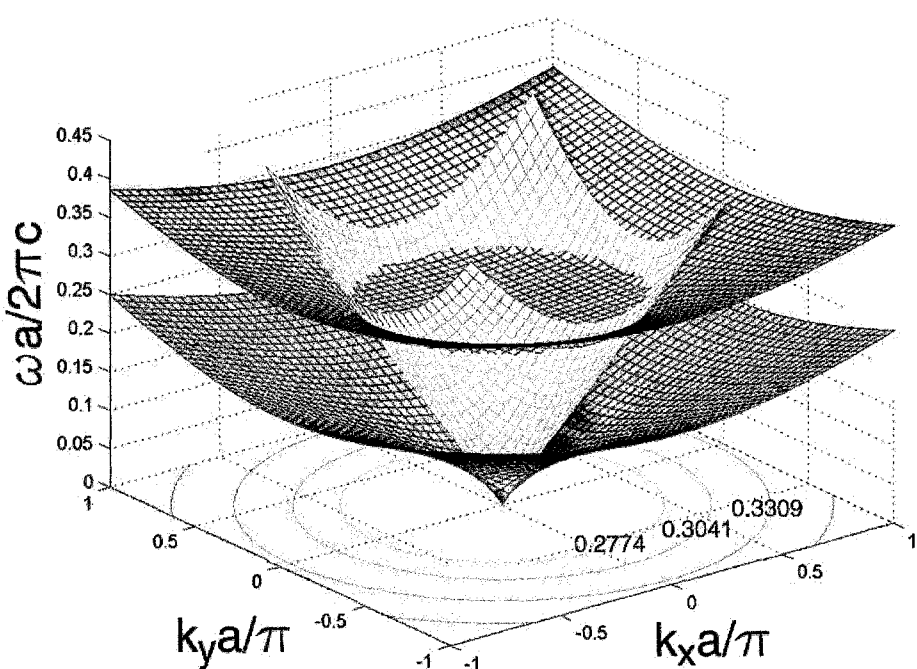


Figure 2.9: The dispersion of the first two bands supported in the unpatterned Si slab. The light cone is represented as an unshaded mesh. The iso-frequency contours in the case of the unpatterned slab are circles (shown for  $a/\lambda \in 0.2774, 0.3041, 0.3309$ ) since all in-plane directions are equivalent.

2.7(a)], both frequency and  $k$ -vector parallel to the boundary (cleaved facet) need to be conserved (up to the modulo of the reciprocal lattice vector). In our case the boundary is in the xOz plane, and therefore  $k_x$  and  $k_z$  need to be conserved. The energy of the excited mode will propagate with a group velocity that can be calculated as

$$\vec{v}_g = \vec{\nabla}\omega(\vec{k}) = \hat{x} \cdot \frac{\partial}{\partial k_x} \omega(k_x, k_y) + \hat{y} \cdot \frac{\partial}{\partial k_y} \omega(k_x, k_y), \quad (2.5)$$

and the direction of propagation (in the real space) will be perpendicular to the iso-frequency contour for that frequency (in the  $k$ -space). Therefore, if the input light has a range of  $k_x$  vectors, and all of them are, for example, between  $-k_0$  and  $k_0$  in Figure 2.10(a), then light in the PPC will propagate along the y-axis direction ( $\Gamma X$ ), as indicated in grey in Figure 2.10(a). In other words, the light beam in the PPC can be self-collimated. This property of square PPCs is entirely due to the fact that iso-frequency contours for Band 2 look like squares. In contrast to the PPC case, iso-frequency contours of an unpatterned Si slab are circles [Figure 2.10(b)]. When such a slab is excited with a range of  $k_x$  vectors, light in the slab diverges as schematically indicated by the gray region in Figure 2.10(b).

In our analysis we assumed that, for a given frequency,  $k_x$  is within one of the horizontal sides of the iso-frequency “squares” [Figure 2.10(a)]. However, the  $k_x$  component is determined by the wavelength of the incident light as well as the angle of incidence  $\theta$  [Figure 2.7(a)]. Therefore, we have to find the range of  $\theta$ s for which our assumption is valid. We start by noting that the  $k_x$  can be expressed as  $k_x = (2\pi/\lambda) \cdot \sin(\theta)$ . In order for  $k_x$  to belong to a horizontal side of a iso-frequency square it has to satisfy  $|k_x| \leq k_0(a/\lambda) \cdot \pi/a$ , where  $2 \cdot k_0(a/\lambda)$  is the length of the horizontal side of the square, and is a function of normalized frequency. Combining these two expressions we get

$$\frac{k_0(a/\lambda)/2}{a/\lambda} \geq |\sin(\theta)|. \quad (2.6)$$

The minimum value of  $k_0(a/\lambda)$  is  $k_{0,min} = k_0(a/\lambda = 0.306) = 2 \cdot 0.306 = 0.612$ , since the relation between the normalized  $k$ -vector and normalized frequency is  $k \cdot a/\pi = 2 \cdot a/\lambda$ , in the case of the light line. Then, the minimum of the expression at the left hand side of the

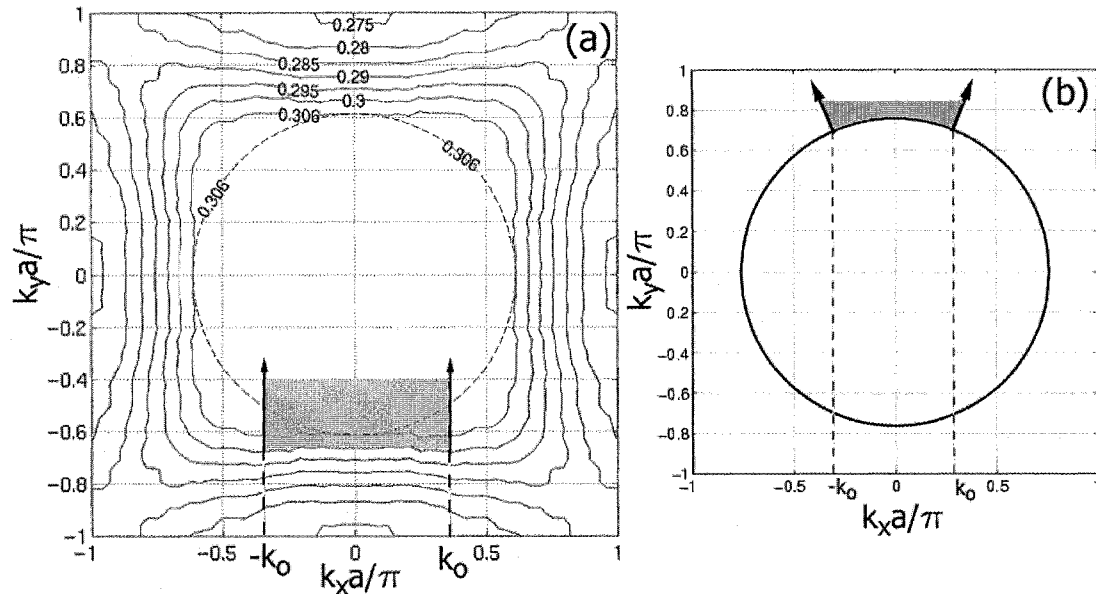


Figure 2.10: (a) The iso-frequency contours of the Band 2 of square lattice PPC. Only the region below the light cone is shown [ $\lambda \in (0.273, 0.306)$ ]. The light cone, for  $\lambda = 0.306$ , is represented by the dashed circle. The light of frequency  $a/\lambda = 0.3$  is self-collimated and propagates in the direction (in the real space) indicated by the gray color. (b) The iso-frequency contours of the unpatterned Si slab are circles. Light diverges at the angles shown in the gray color.

inequality (2.6) is

$$\frac{k_{0,min}/2}{(a/\lambda)_{max}} = \frac{0.612/2}{0.306} = 1. \quad (2.7)$$

and the inequality is satisfied for any angle  $\theta$ . That is, for any incident angle, light in the frequency range  $a/\lambda \in (0.295, 0.306)$  can be self-collimated within the PPC and propagate along the  $y$ -axis direction (in real space). However, this would be true if the iso-frequency contours were perfect squares. Then  $k_x$  could be anywhere on the horizontal side of the square. Since the iso-frequency squares are rounded at the corners, we have to assume a more conservative value  $k_{0,min} = 0.5$  [Figure 2.10(a)]. Then, the left hand side of (2.6) becomes

$$\frac{k_{0,min}/2}{(a/\lambda)_{max}} = \frac{0.5/2}{0.306} = 0.817, \quad (2.8)$$

and the sufficient condition for inequality (2.6) to be satisfied is  $|\theta| \leq \arcsin(0.817) \approx 54^\circ$ . Therefore, the square lattice PPC acts like a self-collimator for incident angles  $|\theta| \leq 54^\circ$  and  $a/\lambda \in (0.295, 0.306)$ . The amount of light that is coupled into the slab depends on the incident angle of the light. Also, the group velocity of any mode depends on the frequency of that mode, and is calculated to be in the range  $v_g \in (0.16, 0.25) \cdot c_0$  ( $c_0$  is the speed of light in air) when  $a/\lambda \in (0.295, 0.306)$  and  $|\theta| \leq 54^\circ$ . Modes with higher frequency will have higher group velocities, since Band 2 becomes more flat at lower frequencies.

In order to verify the predictions that self-collimation is possible in a square lattice PPC we have performed 3-D FDTD modelling of such a structure. The results presented in Figure 2.11 show the field evolution ( $B_z$  component) in the patterned (a, b) and unpatterned (c) Si slab. The structures were excited with a dipole source placed at the center of the slab. In the case of the unpatterned slab, characteristic dipole radiation in the form of “spherical” waves can be observed. The PPC structure shown in Figure 2.11(a) was excited with the dipole source which frequency ( $a/\lambda = 0.295$ ) was chosen to be in the frequency region of Band 2 where iso-frequency contours are squares [Figure 2.10(a)]. Because of that, it is expected that light is radiated predominantly in four TX directions, that is in directions that are perpendicular to four sides of iso-frequency “squares”. Indeed, a 3-D FDTD simulation of the structure [Figure 2.11(a)] shows such behavior. Therefore, we conclude that a square lattice PPC modifies the radiation of the dipole source in the way predicted by the above analysis of iso-frequency contours. It is also important to notice that this interesting phenomena is “taking place” outside the light cone. Therefore, the light is self-collimated

as it propagates in the PPC *without* any losses.

Effects similar to the one described above could be obtained by exciting Band 1.<sup>16</sup> For example, if  $k_x \approx \pi/2a$  and  $a/\lambda$  close to 0.19 [Figure 2.8(b)], light would again be well collimated, now in the  $\Gamma M$  direction. However, since the iso-frequency contours in this case are “rounded” squares, such collimation is weaker and some divergence is present [Figure 2.11(b)], but it is smaller than in the case of an unpatterned Si slab.

#### 2.4.2 Complete Band-diagram of Triangular Lattice PPC

The complete band diagram in the case of triangular lattice is shown in Figure 2.12 ( $r = 0.3 \cdot a$ ,  $t = 0.57 \cdot a$ ,  $a = 30$  computational points). The first three bands, calculated for *all*  $k$ -vectors in the first Brillouin zone, are shown in Figure 2.12, and individual bands along with their iso-frequency contours in Figure 2.13. The complete band diagram of the triangular lattice photonic crystal has a lot more structure than the square lattice one, as a result of higher symmetry of this structure. For example, iso-frequency contours of the third band have a characteristic star-shape what can be used to achieve self-focusing, spot-size conversion, and super-prism effects.

### 2.5 Conclusion

We studied dispersion properties of square and triangular lattice planar photonic crystals, and we investigated the influence of geometry of the lattice on the width and position of the bandgap. We found that a triangular lattice has a much wider bandgap than a square lattice, and that the width of the bandgap decreases as the holes in the photonic crystal lattice are made smaller and as the refractive index contrast between dielectric slab and environment is reduced. Also, we analyzed complete band diagrams of square and triangular PPCs, for all  $k$ -vectors in the first Brillouin zone, and we found that a photonic crystal lattice of square symmetry can be used to achieve the self-collimation of light beams.

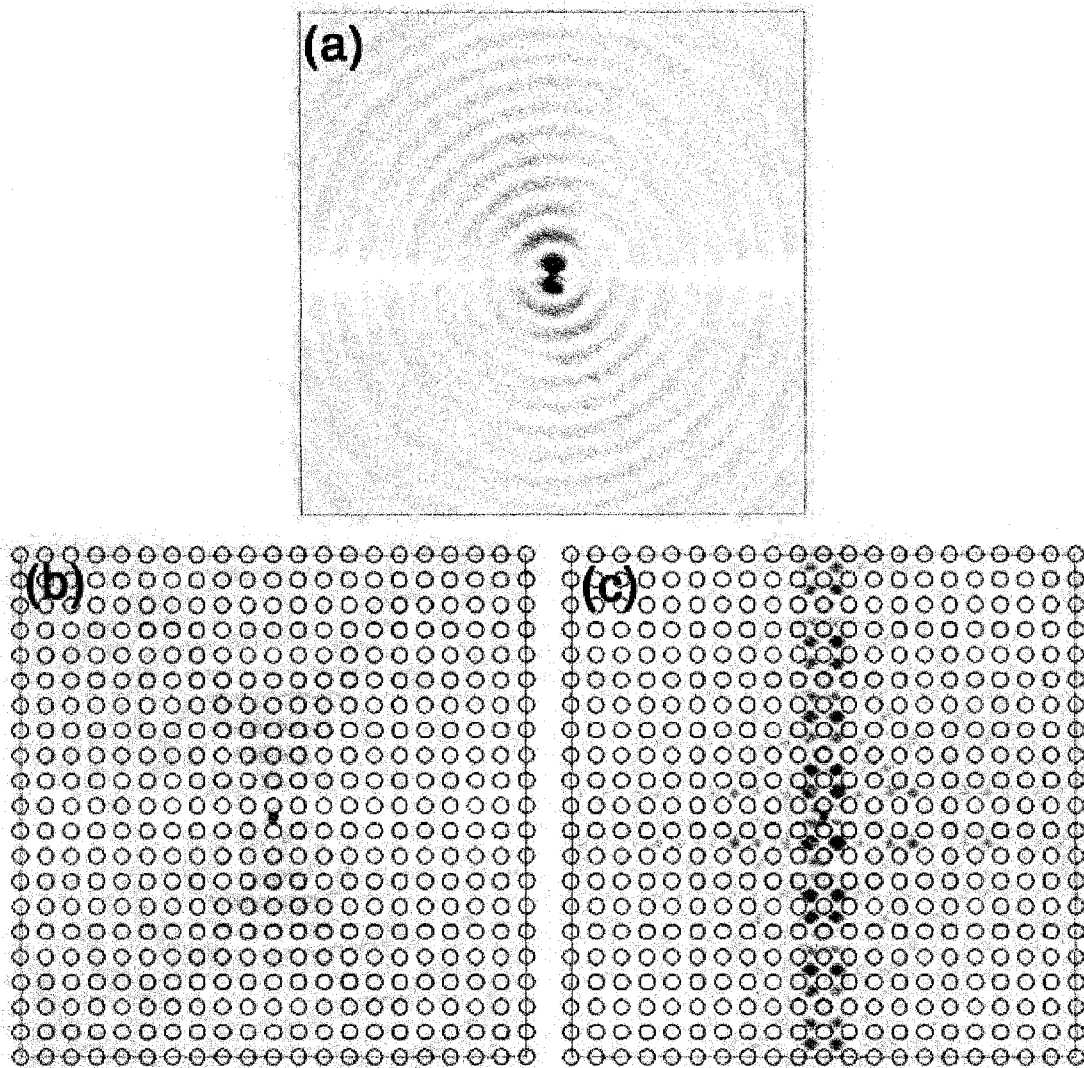


Figure 2.11: Evolution of the  $B_z$  component of the EM-field excited in the (a) unpatterned slab and (b), (c) slab patterned with square lattice PPC. Structures were excited with dipole sources (with  $E_x$  component) at frequencies (a)  $a/\lambda = 0.19$ , (b)  $a/\lambda = 0.19$  and (c)  $a/\lambda = 0.295$ . Self-collimation can be observed in the case (c) as predicted. In this case, light is radiated predominantly along TX directions. Radiation in  $y - axis$  direction is stronger because the structure was excited with  $E_x$  field only.

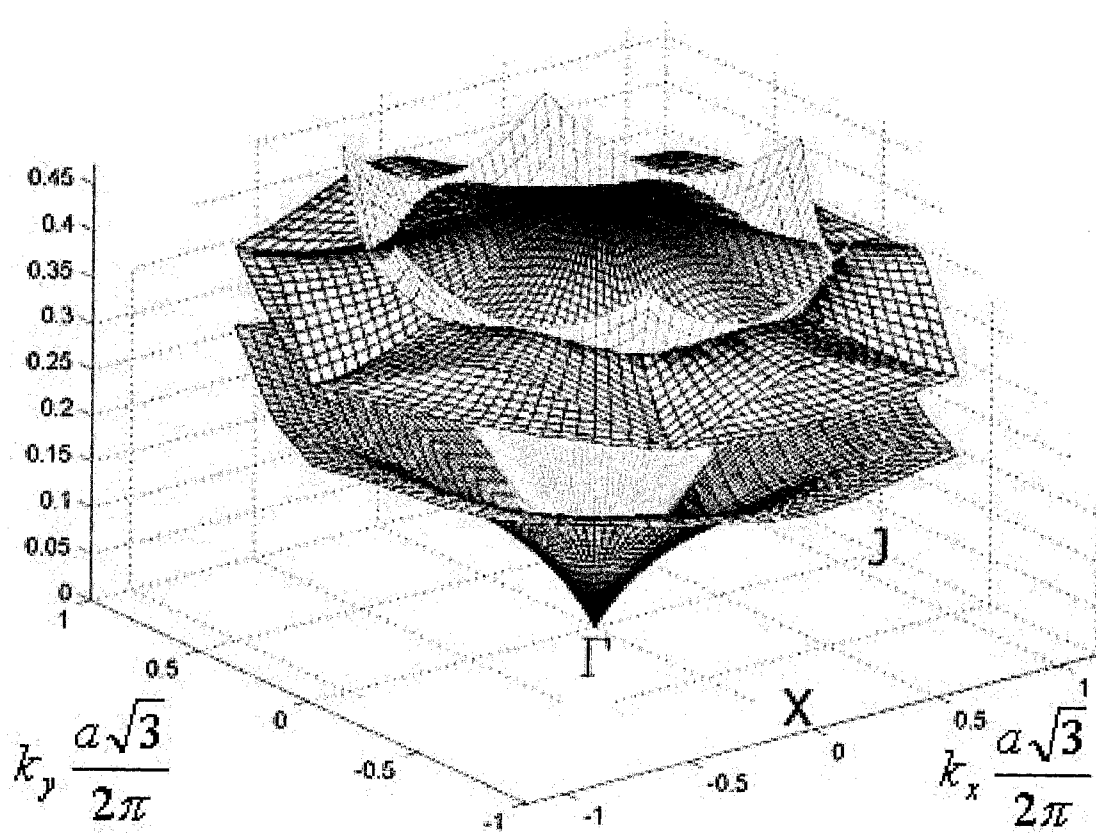


Figure 2.12: Band-diagram of the first three bands of a triangular PPC, calculated for all  $k$  vectors in the first Brillouin zone. The light cone is represented as an unshaded mesh.

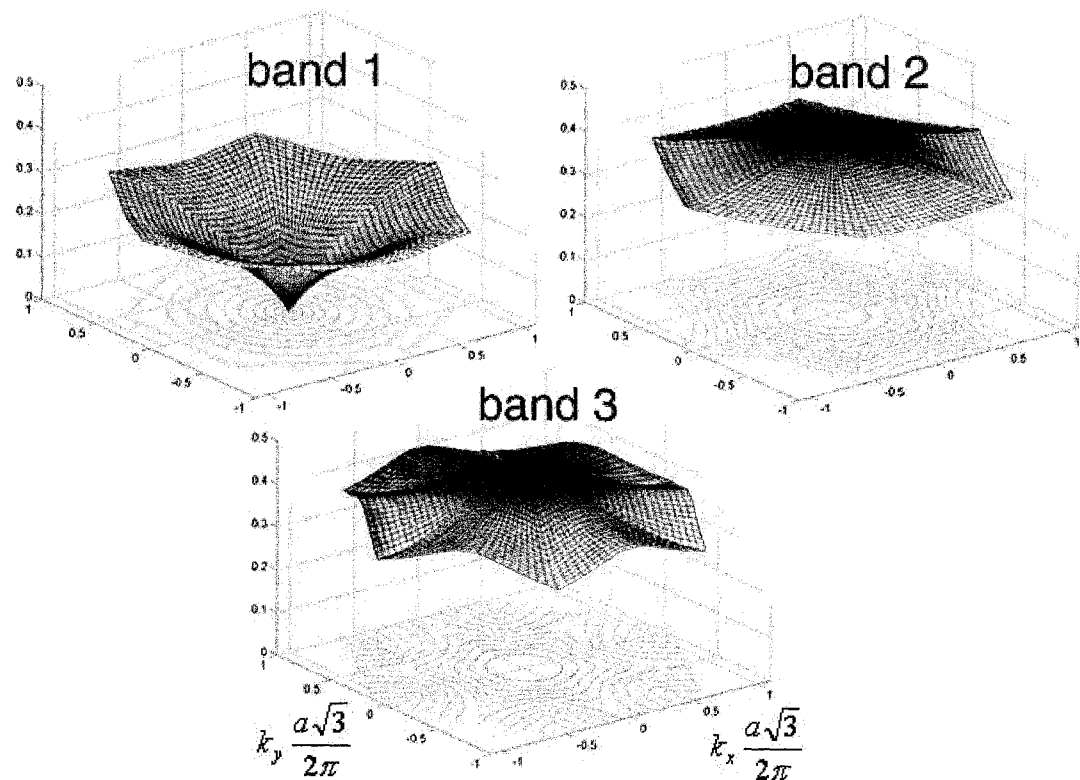


Figure 2.13: The bands of triangular lattice shown along with their iso-frequency contours.

## Chapter 3

# Planar Photonic Crystal Cavities and Lasers

### 3.1 Introduction

One of the most promising applications of planar photonic crystals is the realization of a compact and efficient optical nanocavity, with high quality factor ( $Q$ ) and small mode volume ( $V_{mode}$ ). Such a nanoscale optical resonator is of interest for a number of applications, both of practical and academic importance. For example, PC cavities can be engineered to concentrate light in the air, and they are natural candidates for investigation of interaction between light and matter on a nanoscale level. Some of the most interesting applications of planar photonic crystal nanocavities are

- 1. Low-threshold laser** (including threshold-less laser)

Due to small  $V_{mode}$  of PC cavities,  $Q/V_{mode}$  ratio can be large in these structures resulting in low-threshold powers of photonic crystal nanolasers.

- 2. Cavity QED experiments**

Again, large  $Q$  and small  $V_{mode}$  are important for quantum electrodynamics experiments. For example, strong coupling between neutral Cs atoms, or a single quantum dot, placed in the PC cavity with the cavity field has been predicted. Integration of several cavities can lead towards realization of quantum-optical networks.

- 3. Bio-chemical sensing/ single molecule detection**

Ultra-small quantities of bio-chemical reagents can be placed in the air region where field intensity is the strongest and their (strong) influence on the optical signature

of the resonator can be monitored. This can lead towards realization of integrated spectroscopy systems (e.g., on-chip Raman spectroscopy).

#### 4. Channel drop filters for WDM applications

PC nanocavities can have high Q factors ( $> 10,000$ ) and they can be highly integrated (less than  $5\mu m$  apart), which makes them promising candidates for realization of channel drop filters in dense wavelength-division multiplex systems.

In this chapter low-threshold PPC lasers<sup>32</sup> and their application in dense biochemical sensor arrays<sup>33</sup> will be studied in detail. Lasers with InGaAsP quantum well active material emitting at 1550 nm were optically pumped at room temperature, and lasing was observed at record-low pumping powers ( $\approx 200 \mu W$ ). The lasers that we developed permit the introduction of analyte within the peak of the optical field of the lasing mode. We have demonstrated the operation of photonic crystal lasers in different ambient organic solutions, and we have explored the design compromises for developing sensitive low-threshold spectroscopy sources.

Photonic crystal cavities can be formed by modifying one or more holes in the photonic crystal lattice.<sup>3</sup> By making one of the holes bigger or smaller (Figure 3.1), we form a potential well for the modes supported in bulk planar photonic crystal. This is similar to formation of potential wells in periodic electric potential studied in quantum mechanics. By making one of the holes bigger, we locally increase the amount of low-dielectric constant material (air) and therefore increase the energy of the modes supported in the bulk photonic crystal. Modes that were originally confined in the dielectric material (dielectric band modes) will now be pulled up into the band gap, and be trapped in the energy well formed by increasing the size of the hole. This bound state exists close to the dielectric band and in its nature is similar to an acceptor level in semiconductors. Therefore, modes created by modification of dielectric band are called *acceptor modes*. Similarly, by reducing the size of one of the holes, we form bound states close to the air band - *donor modes*.<sup>34</sup> Acceptor and donor modes are shown in Figure 3.1.

In case of 2-D photonic crystal, with infinitely many PC layers around the defect, light can be completely trapped to the defect. However, in cavities defined in photonic crystal slabs, modes will suffer from radiation losses due to the coupling into the continuum of

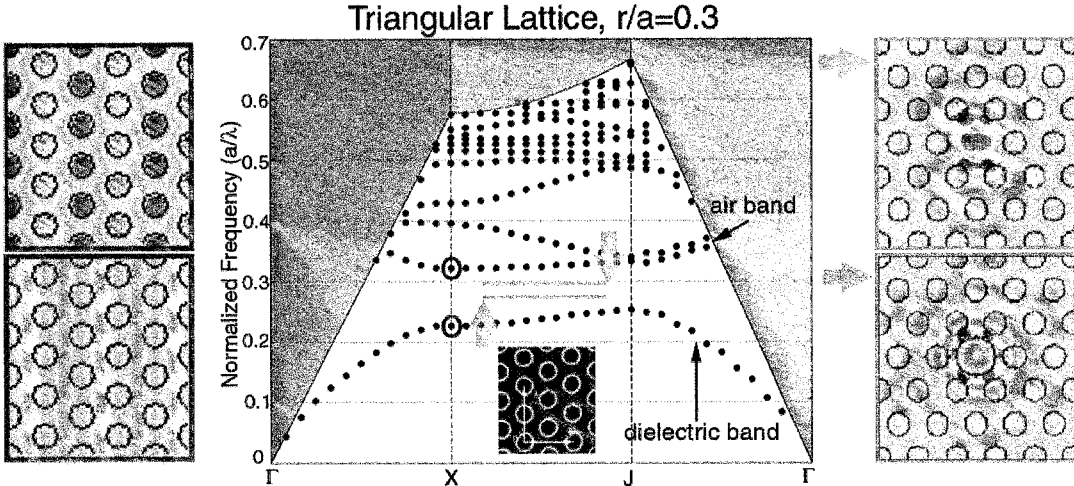


Figure 3.1: Dispersion diagram for the modes supported in the triangular lattice planar photonic crystal ( $r/a = 0.3$  this time). Mode profiles for one component of the  $E$  field in the dielectric (red) and air (blue) band, taken at the  $X$  point, are also shown.

radiation modes that exist within the light cone.\* These components contribute to the *out-of-plane* losses of the cavity, as shown in Figure 3.2(a). At the same time, light can leak laterally due to the finite number of the photonic crystal layers surrounding the cavity [Figure 3.2(b)], contributing to the *in-plane* losses of the resonator.

The efficiency of a resonator, described by a quality factor ( $Q$ ), can be expressed as the ratio of energy stored in the cavity and energy lost (emitted) from the cavity in one cycle:

$$Q = 2\pi \frac{W_{stored}}{W_{lost}}, \quad (3.1)$$

This quality factor can be broken into lateral quality factor ( $Q_{lat}$ ) and vertical quality factor ( $Q_{vert}$ ) that take into account in-plane and out-of-plane losses, respectively.

$$\frac{1}{Q} = \frac{1}{Q_{lat}} + \frac{1}{Q_{vert}}, \quad (3.2)$$

By adding more photonic crystal layers around the cavity, the lateral leak can be completely suppressed and we can assume that  $Q_{lat}$  can be arbitrary high.<sup>15</sup> Therefore, the

---

\*Since the cavity mode is localized in the real space it is extended in the reciprocal  $k$  space, as governed by the uncertainty principle, and therefore it consists of  $k$ -vector components that are positioned within the light cone.

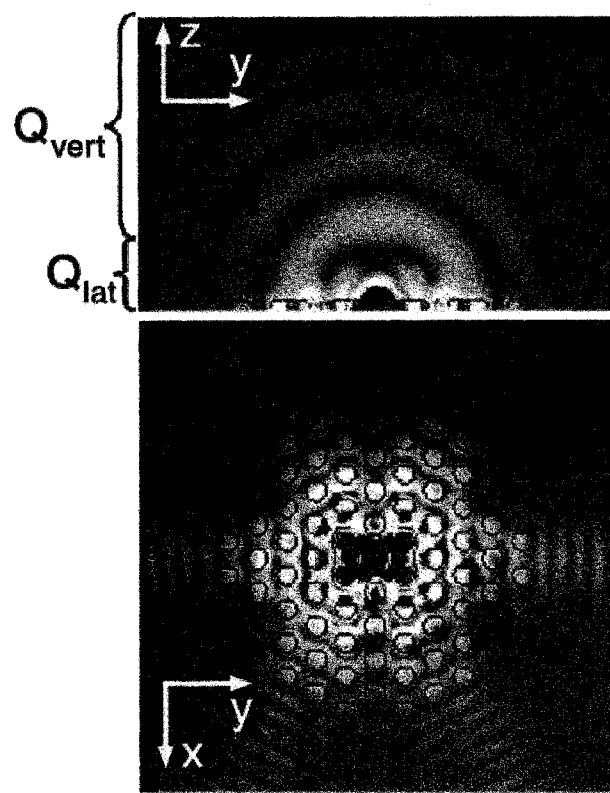


Figure 3.2: One of the dipole modes supported in a single defect cavity. In-plane and out-of-plane energy leaks can be observed.

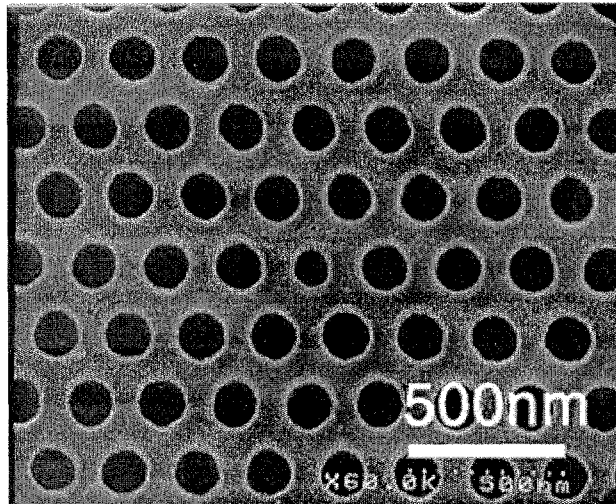


Figure 3.3: Single defect cavity fabricated in AlGaAs, and designed to operate at  $\lambda = 852$  nm.

ultimate  $Q$  is limited by  $Q_{vert}$ . Unfortunately, the simplest photonic crystal cavity, formed by reducing the size of one of the holes, known in literature as *single defect* cavity, suffers from large radiative losses (small  $Q_{vert}$ ). The best quality factor that one can achieve with this cavity is limited to  $\approx 2,000$ .<sup>35,36</sup> This  $Q$  is obtained in a cavity with  $r/a = 0.3$  when the radius of the defect hole is slightly reduced to  $r_{def}/a = 0.2$ . Such a cavity fabricated in AlGaAs material system, designed to operate at  $\lambda = 852$  nm is shown in Figure 3.3. This cavity design is not robust since the defect hole is only slightly smaller than bulk PPC holes, and any fabrication related fluctuations can form unintentional defects and spoil the  $Q$  of the cavity. At the same time, quality factor of  $Q \approx 2,000$  is not spectacular, and better  $Q$  is needed for all applications proposed in the beginning of this section. The problem of high-Q cavity design has recently attracted a lot of research attention and several designs were proposed and characterized experimentally.<sup>20,32,35,37–44</sup> Also, operation of PPC lasers based on various PPC nanocavities have been reported by several groups.<sup>20,32,43,45–62</sup>

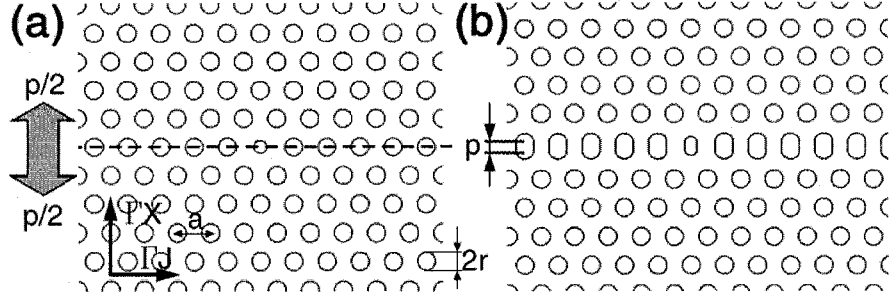


Figure 3.4: (a) Conventional single defect cavity ( $p = 0$ ). When structure is “cut” along the dashed line, and two PPC half-planes are dislocated along  $\Gamma X$  direction by  $p/2$ , (b) high-Q cavity can be formed ( $p = 0.25 \cdot a$ ).

### 3.2 High-Q Cavity Design

The high-Q cavity geometry that we proposed is based on fractional edge dislocations in the single defect triangular lattice photonic crystal.<sup>35</sup> Our planar photonic crystal is based on a free-standing membrane: high dielectric constant slab (refractive index  $n = 3.4$ ) is perforated with 2-D lattice of holes with periodicity  $a$  and is suspended in the air. The cavity consists of a defect hole (radius  $r_{def}$ ) that is smaller than surrounding holes (radius  $r$ ) which define the photonic crystal mirror. The row that contains the defect hole is elongated by moving two photonic crystal half-planes a fraction of a lattice constant apart in the  $\Gamma X$  direction (Figure 3.4). Each half-plane is moved by  $p/2$ , yielding total dislocation of  $p$ .

It was shown that in such photonic crystal cavity, with  $r/a = 0.275$ ,  $r_{def}/a = 0.2$  and  $d/a = 0.75$  ( $d$  is thickness of the slab), it is possible achieve Q factors as high as 11,000 by tuning the dislocation parameter  $p$ . The Q was maximized when  $p/a = 10\%$ . These high Q values were obtained while maintaining a very small mode volume of  $V_{mode} \approx 0.1(\lambda/2)^3$ . These cavities were originally designed for cavity QED experiments, where strong-coupling between atoms introduced into the high field region of the cavity and light trapped in the cavity was to be investigated.<sup>35</sup> However, it is clear that the presence of a hole at the point of maximum field intensity is not desirable in low-threshold laser designs, since the overlap with the gain region, provided by quantum wells is decreased. Therefore, we have revisited the problem of cavity design in order to investigate the influence of the defect hole size ( $r_{def}$ ) on the Q factor of the cavity.<sup>63</sup>

In order to improve the lateral confinement of light, we decided to analyze structures

with slightly bigger holes ( $r/a = 0.3$ ). This results in a more compact cavity, since fewer layers of photonic crystal can be used to efficiently confine the light. On the other hand, bigger holes in the photonic crystal mirror increase the scattering of light in the vertical direction and therefore result in decreased Q factors. As the first step, we calculated the band diagram of the bulk photonic crystal with parameters  $r/a = 0.3$ ,  $d/a = 0.75$ , and  $n_{slab} = 3.4$ , and we found that a bandgap exists for vertically even modes (TE-like) for the normalized frequencies in the range  $a/\lambda \in (0.2508, 0.3329)$ . 3-D FDTD was used to calculate this dispersion diagram, as described in the previous chapter. The discretization used in FDTD algorithm was  $a = 20$  computational points. Next, we modelled various high-Q cavity designs in order to find their eigen modes. A single defect donor cavity in a triangular lattice photonic crystal without the fractional edge dislocation is known to support two doubly-degenerate, linearly polarized, dipole modes.<sup>4,15</sup> However, as we stretch the photonic crystal lattice by introducing a fractional dislocation, these modes start to interact and the degeneracy between them is lifted. In Figure 3.5 we show the results of 3-D FDTD analysis of the structure with  $p/a = 10\%$ ,  $r_{def} = 0.2a$ ,  $r = 0.3a$  and  $d = 0.75a$ . Two dipole modes, labelled LQ and HQ, are found to exist in the cavity<sup>†</sup>. The mode at longer wavelength can have an order of magnitude better Q factor value and therefore is called HQ (high-Q) mode.

In Figure 3.6 we show the dependence of the eigen-frequency and Q of HQ dipole mode on the stretching (dislocation) of the central row ( $p/a$ ) and on the size of the defect hole ( $r_{def}/a$ ). It can be seen that by increasing the dislocation, the splitting between the two dipole modes increases. Also, as the defect hole becomes larger, the modes shift towards higher frequencies. This shift occurs since a larger hole in the center of the cavity leads to an increased overlap between the optical field and air. One more interesting feature is that splitting between LQ and HQ modes does not depend strongly on the size of the central hole, and is mostly dependant on the amount of dislocation introduced.

The mode of interest for laser applications is the HQ mode, since it has an order of magnitude higher Q and therefore will reach threshold first. The quality factors of LQ modes are limited to several hundreds and therefore are not of practical importance. In Figure 3.7 we show dependence of the vertical ( $Q_{vert}$ ) and lateral ( $Q_{lat}$ ) quality factors of

---

<sup>†</sup>Additional modes are found close to the air-band, as well. Those modes are not localized to the defect hole, but are instead attributed to the waveguide modes of the elongated central row.

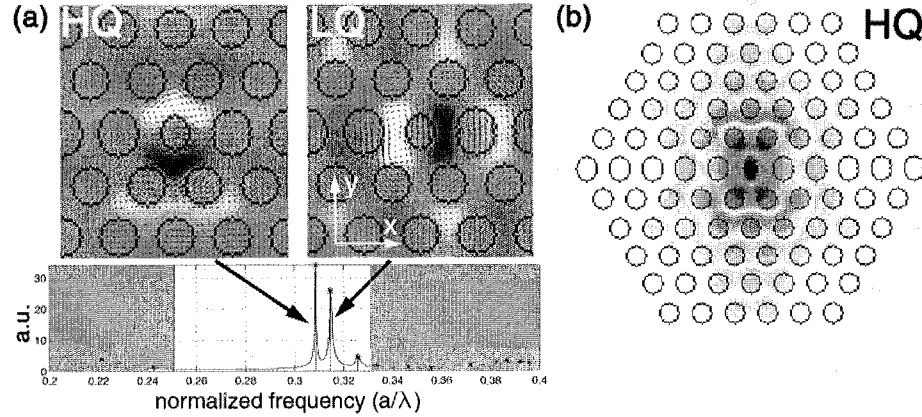


Figure 3.5: Defect modes of the cavity with  $p/a = 10\%$  and  $r_{def} = 0.2a$ . (a) Cavity supports two dipole modes, and their profiles are shown ( $B_z$  component and vector of the  $\vec{E}$  field). Spectrum of the modes supported in the cavity, obtained using 3-D FDTD, is also shown. The bandgap is shown in white. (b) Amplitude of the E field is shown. It can be seen that light is localized in the small defect hole.

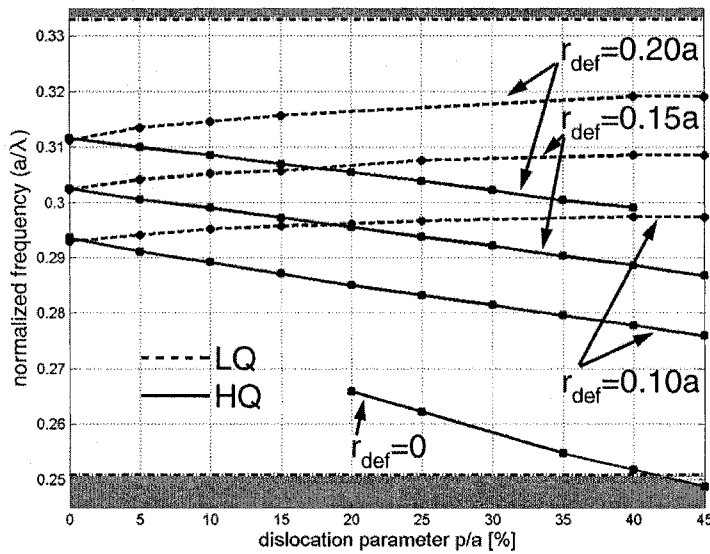


Figure 3.6: Dependence of the position of the two dipole modes of the cavity on the amount of dislocation introduced ( $p$ ), and the size of the defect hole ( $r_{def}$ ).

the HQ mode on the amount of fractional edge dislocation ( $p$ ), for various sizes of central defect hole ( $r_{def}$ ). In our calculations, cavity was surrounded with five layers of photonic crystal, as shown in Figure 3.5(b). The lateral Q-factor (in-plane Q-factor) depends on the position of the mode within the bandgap, and can be improved by adding more photonic crystal layers around the cavity. The ultimate Q-factor that we can achieve is therefore limited by  $Q_{vert}$ .

Figure 3.7 tells us that the best Q that we could hope to achieve in the modelled cavity geometry is around 7,000. In comparison, we were able to achieve Qs as high as 11,000 when  $r/a = 0.275$ . As expected, due to the increased size of the bulk photonic crystal holes ( $r/a = 0.3$ ), light scattering in the vertical direction increases, and therefore the Q-factors are smaller. The optimal design (Q-factor maximized) requires more dislocation as  $r_{def}$  decreases. This can be understood by looking at spatial frequencies that exist in the Fourier spectrum of the HQ mode. In order to increase the Q of the cavity, components that lie within the light cone need to be minimized. This can be achieved by changing the size of the air-region in the cavity in order to balance the energy that exists in each lobe of the mode[Figure 3.5(b)], and in that way minimize its DC component.<sup>64</sup> The change of the area occupied by the defect hole, induced by stretching of the central row, is  $\Delta A = 2r_{def} \cdot p$ . From this equation it follows that in order to achieve the same influence on the mode larger  $p$ 's are needed when  $r_{def}$  is made smaller. In other words, for big defect hole small change in  $p$  has big influence on the mode since most of the light is located in the hole.

Another important figure of merit of any laser design is the gain provided by the laser cavity. As the defect hole diameter is decreased and the amount of dislocation is increased, we expect a better overlap between the optical cavity mode and the quantum wells, and therefore reduced laser threshold. However, it is important in our application that central defect hole is as large as possible so that we can achieve strong interaction between light emitted from the laser and material (nanoparticles, single molecules, chemical fluids, gasses, etc) placed in the strong optical field of the laser. Therefore, we have chosen  $r_{def} = 0.15a$  and  $p = 0.25a$  as a good compromise for our initial laser sensor design.

By introducing different material into the photonic crystal holes, or by immersing our lasers in various chemicals (liquids, gasses) altogether, refractive index of the surrounding is changed. Therefore, it is of interest to determine the change in the Q and eigen-frequency of the cavity resonances as the cavity is back-filled with reagents ( $n > 1$ ). In Figure 3.8(a)

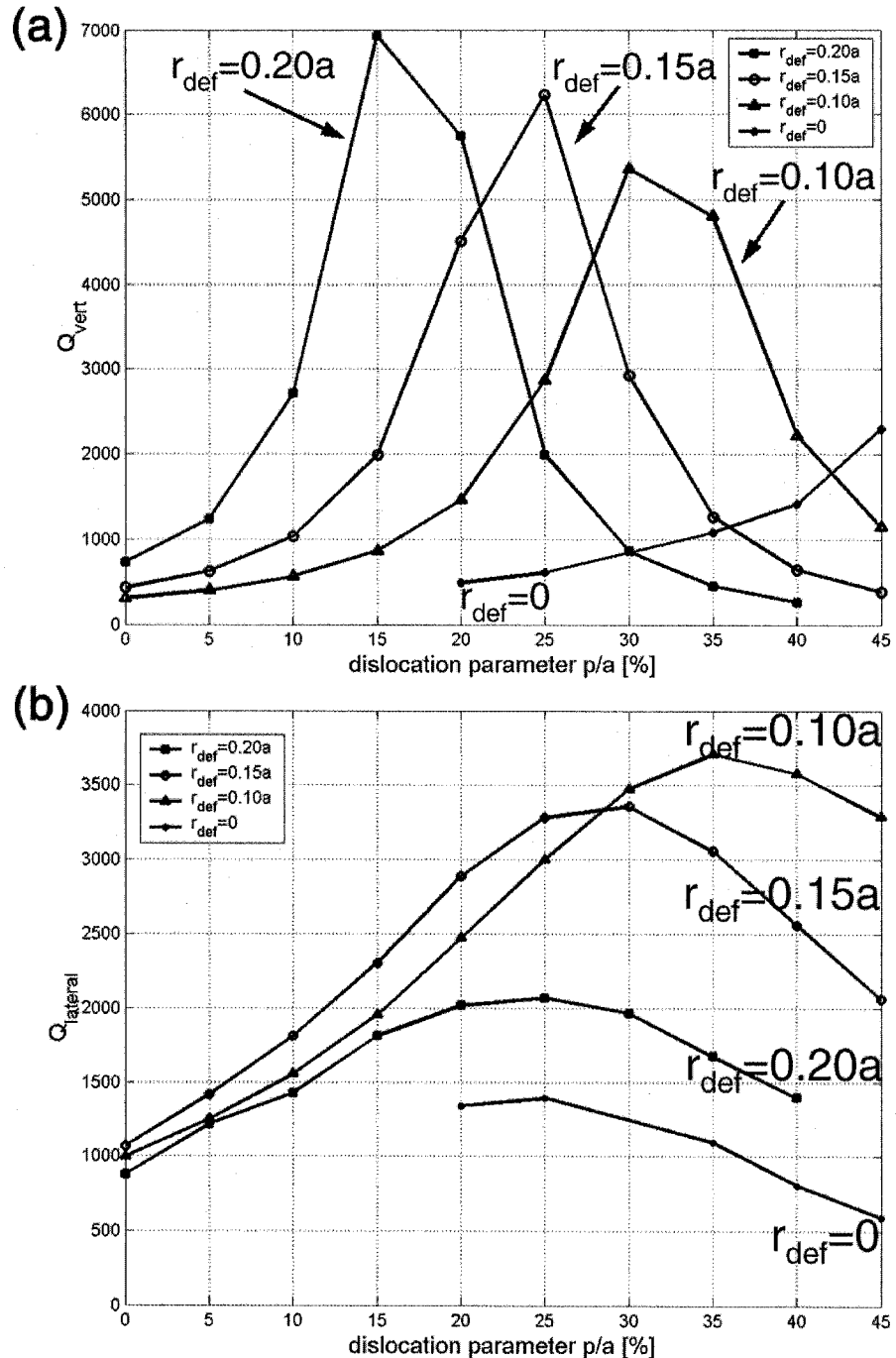


Figure 3.7: Dependence of the (a) vertical and (b) lateral quality factor of the HQ mode on the amount of dislocation ( $p$ ) and the size of the defect hole ( $r_{def}$ ). Only five layers of photonic crystal surrounding the defect hole was used.  $Q_{lateral}$  can be improved by adding more photonic crystal layers.

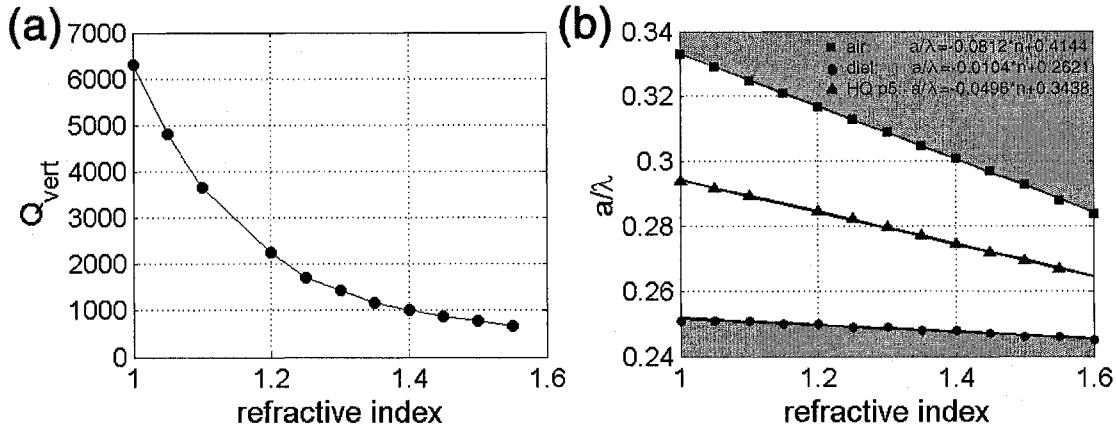


Figure 3.8: Dependence of the (a) Q factor and (b) eigen-frequency of cavity resonance on the refractive index of analyte introduced in the cavity with  $p/a = 25\%$ .

we observe that the highest  $Q$  that we could hope to achieve in the modelled cavity design occurs at an ambient refractive index  $n_{env} = 1$  (air), and this value deteriorates as the refractive index of the ambient surrounding the photonic crystal cavity is increased. This decrease in  $Q$  is a result of the weaker vertical confinement of light by total internal reflection, and can be compensated for by increasing the thickness of the photonic crystal slab.

It is interesting to note that the frequency of the resonant mode, as well as the band edges of the photonic crystal mirror, depend linearly on the refractive index of the environment ( $n_{env}$ ) [Figure 3.8(b)]. From linear fits of the dependence of the resonant frequency on  $n_{env}$ , we can estimate the sensitivity of the cavity, and we find that the wavelength shift of the resonance is approximately  $\Delta\lambda \approx 266 \cdot \Delta n_{env}$ , where  $\Delta n_{env}$  is the change in refractive index. The simplest method of optically sensing ambient material uses wavelength shifts in the laser spectrum when the laser is immersed into a solution or exposed to a material to measure its refractive index. In this method, the sensitivity of the sensor depends on the smallest change in refractive index that can be optically detected. In passive devices, this is related to the width of the cavity resonance peak, which in turn is determined by cavity quality  $Q$ . If we assume that our cavity is embedded in a typical polymer ( $n_{env} = 1.4$ ) a wavelength shift that is still observable from cavity with  $Q = 1,000$  is  $\Delta\lambda = 1.55$  nm, what corresponds to change in refractive index of  $\Delta n \approx 0.0056$ . On the other hand, once we

Table 3.1: Applications of high-Q cavities

application	material	wavelength	periodicity
-------------	----------	------------	-------------

channel drop filter for WDM	SOI	1550 nm	440 nm
low-threshold laser for nano-spectroscopy	InGaAsP	1550 nm	440 nm
cavity QED - strong coupling experiment	AlGaAs	852 nm	240 nm

introduce optical gain into the cavity, as in the case of the proposed laser spectrometer, the linewidth of emission is significantly narrowed (in our case  $\Delta\lambda \approx 0.12$  nm), and sensitivities to  $\Delta n < 0.001$  can be measured even in cavities with modest Q factors. Figure 3.8 suggests that the edge of the air band is even more sensitive to changes in the refractive index than the cavity mode itself (Chapter 2). Therefore, band-edge lasers<sup>46,50,52,57,65</sup> might be even better choice for applications where high sensitivity to the changes of refractive index are needed. However, band-edge lasers operate at extended bulk PPC modes, with large mode volumes, and therefore are not suitable for applications where high spatial sensitivity is needed (e.g., single molecule detection).

The high-Q cavity described so far can be used for various applications, but we were mostly interested in three major applications summarized in Table 3.1. The material of choice, wavelength of interest and characteristics lattice constant for each of these applications is also shown in Table 3.1, and fabricated structures are shown in Figure 3.9. In next section we present the details of fabrication procedure for lasers made in InGaAsP material. Fabrication procedure for devices made in silicon-on-insulator is explained in Chapter 4 when we study photonic crystal waveguides.

### 3.3 Low-threshold Planar Photonic Crystal Nanolaser

In this section we explain the fabrication and experimental characterization of lasers realized in InGaAsP material system. InGaAsP quantum well material was grown on InP substrate using metal-organic chemical vapor deposition (MOCVD). Optical gain is provided by four 9 nm thick, compressively strained, quantum wells with an electronic bandgap at  $\lambda_{bg} = 1.55$   $\mu$ m, separated by 20 nm thick InGaAsP barriers ( $\lambda_{bg} = 1.22$   $\mu$ m). Because of the compres-

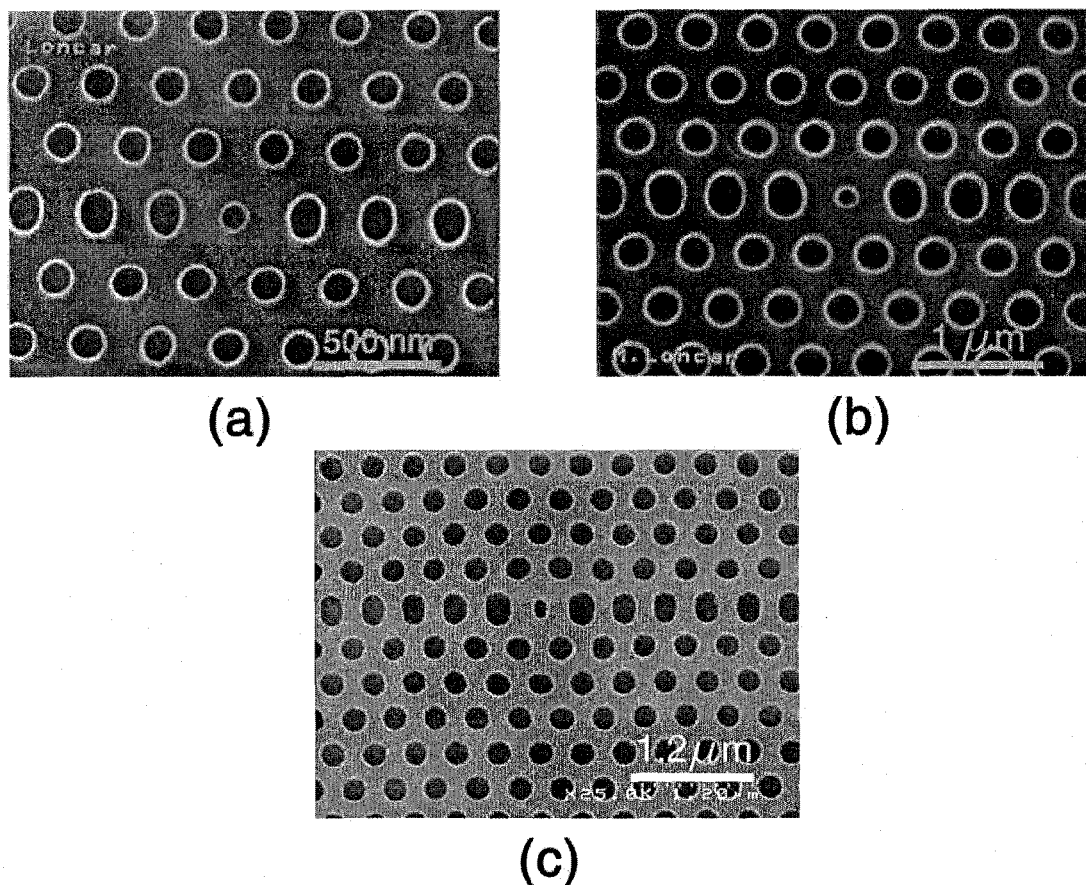


Figure 3.9: High-Q cavity designs based on fractional edge dislocations fabricated in (a) AlGaAs, (b) SOI, (c) InGaAsP.

Table 3.2: InGaAsP wafer structure

layer	composition	layer description	$\lambda_{bandgap}(\mu m)$	strain	thickness [nm]
12	InP	cap			50
11	InGaAsP	electron confinement	1.22		117
10	InGaAsP	QW	1.55	0.85% compress.	9
9	InGaAsP	electron confinement	1.22		20
8	InGaAsP	QW	1.55	0.85% compress.	9
7	InGaAsP	electron confinement	1.22		20
6	InGaAsP	QW	1.55	0.85% compress.	9
5	InGaAsP	electron confinement	1.22		20
4	InGaAsP	QW	1.55	0.85% compress.	9
3	InGaAsP	electron confinement	1.22		117
2	InP	sacrificial layer			1000
1	InGaAs	etch stop			20
	InP	substrate			

sive strain, the coupling is the strongest to the TE polarized modes of the slab. This is desirable since in triangular lattice PPC the bandgap is larger for TE-polarized light. This active material is placed in the center of a 330 nm thick InGaAsP slab ( $\lambda_{bg} = 1.22 \mu m$ ), with 1  $\mu m$  thick sacrificial InP layer underneath the slab. An InGaAs etch stop is introduced above the InP substrate, and the active quaternary material is designed to operate at  $\lambda = 1.55 \mu m$ . The wafer structure is shown in Table 3.2.

### 3.3.1 Fabrication Procedure

Fabrication procedure consists of electron-beam lithography, followed by several dry- and wet-etching steps. Ideally, only one mask layer would be needed to define patterns in InGaAsP material of interest. However, due to poor etching selectivity between e-beam resist and InGaAsP we had to use the *mask amplification* method. Total of three mask layers were used before the patterns are defined in InGaAsP. The etch mask consists of 40 nm Au evaporated on top of 100 – 140 nm thick dielectric layer (Figure 3.10). For dielectric we used  $SiO_2$ ,  $Si_3N_4$  or  $SiON$ .  $SiO_2$  and  $Si_3N_4$  were deposited at room temperature using RF sputtering and  $SiON$  (silicon-oxi-nitride) was deposited using plasma enhanced CVD

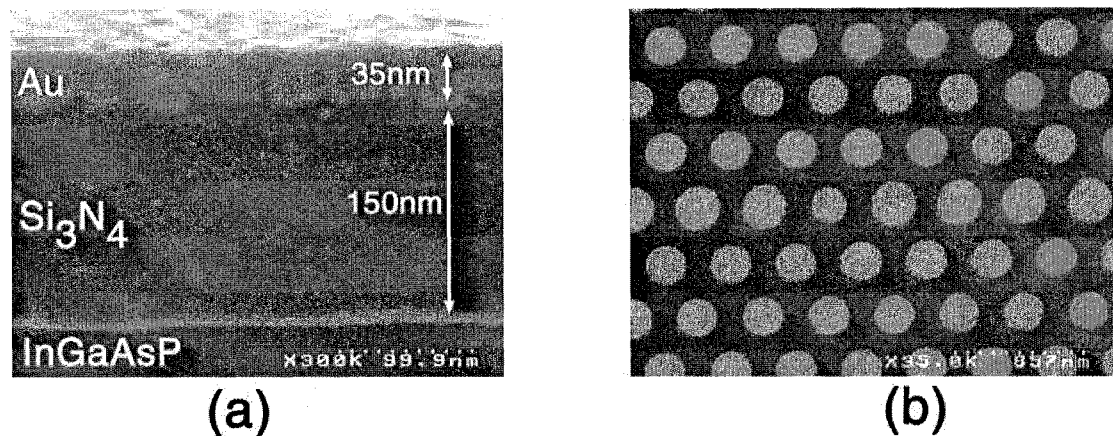


Figure 3.10: (a) Mask used for fabrication of high-Q cavities of the first generation. Mask consists of PMMA, Au and  $Si_3N_4$ . (b) Patterns in PMMA after e-beam lithography. Au can be seen at the bottoms of the holes in the PMMA.

(PECVD) system at  $200^{\circ}C$ . All three masks performed more or less the same in our etching chemistry, but in this section we will describe fabrication procedure assuming  $Si_3N_4$  layer as the dielectric mask layer.

Fabrication procedure begins by RF sputtering of  $100 - 150$  nm of  $Si_3N_4$  and is followed by thermal evaporation of 40 nm of Au. Then, 120 nm of polymethyl methacrylate (PMMA), electron-beam (e-beam) sensitive resist, is deposited on top of the Au layer by spin coating. 2% solution of PMMA diluted in chlorobenzene (molecular weight 950K) was used. PMMA was baked on the hot-plate at  $150^{\circ}C$  for 30 – 40 min. E-beam lithography was performed using converted Hitachi S-4500 scanning electron microscope (SEM). Electron beam voltage was 30KeV, and the dose used to define the pattern in PMMA was  $\approx 300\mu C/cm^2$ . Number of different cavity geometries was beam-written at the same time. By varying the electron dose and the periodicity of the lattice we could span the entire design space of the PPC nanocavities by changing  $a$ ,  $r$ ,  $r_{def}$  and  $p/a$  independently. Upon completing e-beam lithography, PMMA was developed for 30s in PMMA developer and rinsed for 15s in isopropyl alcohol (IPA). This procedure removes the areas exposed by the e-beam, leaving behind positive mask in PMMA. PMMA developer that we used is the mixture of 2-ethoxyethanol:methanol with 3:7 ratio. In Figure 3.10(b) we show one of the structures after e-beam writing and PMMA developing.

Ion beam etching (IBE) is used to transfer the mask from the PMMA into the Au (Figure 3.11).  $Ar^+$  ions are accelerated towards the sample with beam voltage  $V_B = 500V$ , and the beam current is  $I_B = 10mA$ . After  $t = 3min$  the mask is transferred from the PMMA into Au. In Figure 3.11(d) we can see that after the ion milling Au is completely perforated, and the pattern is partially transferred into the  $Si_3N_4$  as well. Also, it can be seen that after the pattern is transferred into the Au layer, the mask quality deteriorates. Similar results were observed at higher beam voltages as well (1,500V). In order to explore this problem, we have evaporated Au using two different evaporators, as well as tried different metal layers (Cr). However, poor results remained to exist. It is interesting to note that the problem was somewhat geometry related as well, and was less apparent in the case of square lattice photonic crystal lattice. Therefore we have attributed this problem to the erosion of PMMA. This problem was solved in the second generation of fabricated samples by excluding the Au mask layer and ion milling step altogether (Section 4 of this chapter).

After milling, we used reactive ion etching (RIE) to transfer the mask from Au into  $Si_3N_4$ , using mixture of 25 sccm of  $C_2F_6$  and 5sccm of Ar as a gas chemistry. This etch step was done at pressure  $P = 35mTorr$  with RF power of  $P_{RF} = 70W$ , and the built-up DC voltage  $V_{DC} \approx 320V$ . It takes about  $t \approx 4min$  to etch 100 – 130 nm of  $Si_3N_4$ , Figure 3.12 shows SEM micrograph of the sample after RIE step.

At the end, the patterns were transferred into the InGaAsP using inductive-coupled plasma RIE etching. We used the mixture of Ar and Cl to perform this final etch step. It is well-known that InP-based materials are hard to etch unless the temperature of the sample is elevated to about  $200^\circ C$ . Due to lack of the heated chuck in our ICP RIE system, the sample was heated locally by very strong plasma. The ICP-RIE etch starts with 15sec treatment with 10sccm of Ar ( $P = 1mTorr$ ), and is followed by 15sec etch in  $Cl/Ar$  chemistry. The etch-parameters are pressure  $P = 1mTorr$ , ICP power  $P_{ICP} = 800W$ , RF power  $P_{RF} = 155W$  and gas mixture of  $Cl:Ar=15sccm:10sccm$ . In spite of short etch time we were able to etch about  $1.3\mu m$  into the InGaAsP/InP material. However, the etch is not optimized, and first 50 – 100 nm is somewhat rough while the rest has very smooth side-walls. The sidewalls are straight throughout the thickness of the InGaAsP slab.

Finally, the remaining  $Si_3N_4$  mask is removed in a HF acid and the InGaAsP membrane is released from the substrate by wet etching in 4:1 HCl:water solution at  $4^\circ C$ . HCl goes into the photonic crystal holes, and selectively attacks InP sacrificial layer, leaving In-

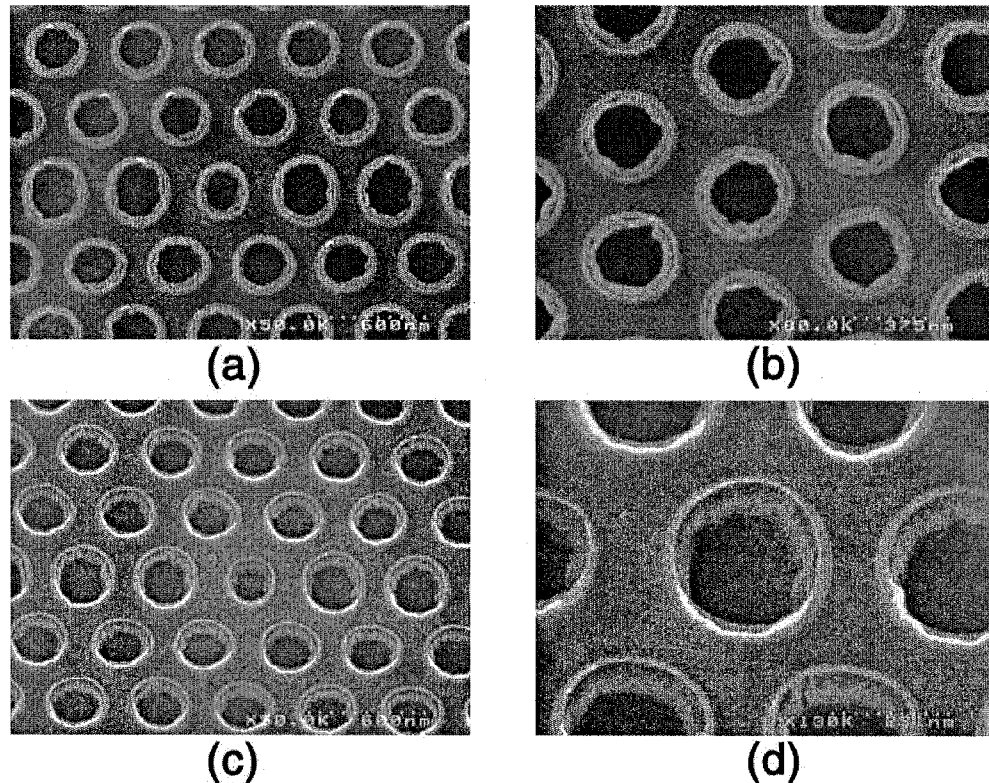


Figure 3.11: SEM micrographs of the cavity after the ion milling step: (a), (b) are top views, and (c) and (d) view at  $30^\circ$  angle.

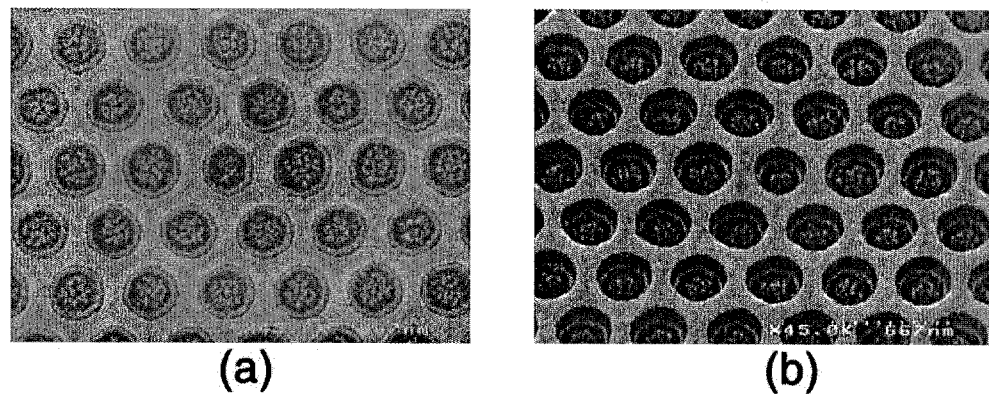


Figure 3.12: SEM micrograph of the sample after RIE. (a) Top view and (b) at  $30^\circ$  angle.

Table 3.3: Process parameters for fabrication of the first generation samples

IBE	RIE	ICP RIE
$V_{beam} = 500V$	$P_{RF} = 70W$	$P_{ICP} = 800W$
$V_{acc} = 100V$	$U_{DC} = 320V$	$P_{RF} = 155W$
$I_{beam} = 10mA$	$P_{process} = 35mTorr$	$P_{process} = 1mTorr$
$P_{process} = 2e - 4Torr$	$C_2F_6$ flow = 25sccm	$Cl$ flow = 15sccm
Ar flow = 1.7sccm	Ar flow = 5sccm	Ar flow = 10sccm
etch time = 3min	etch time = 4min	etch time = 15sec

GaAsP membrane and InGaAs etch-stop layer intact. However, since HCl does not attack InP isotropically, but rather along well defined crystal planes, it is not straightforward to release the membrane from the substrate. Therefore, care needs to be taken when designing the cavities in order to facilitate wet-etching step.

The whole fabrication procedure is summarized in Figure 3.13, and details of each fabrication step are tabulated in Table 3.3.

In Figure 3.14 we show some of the fabricated structures. Each pattern consists of six different cavities that have received the same electron-dose during the e-beam lithography step, and therefore should have similar hole size ( $r$ ) and lattice constant ( $a$ ). The only difference between the cavities in one structure is the value of the dislocation parameter  $p$  that assumed values in the range  $p/a \in (0, 0.25)$ . Fifty different structures were fabricated on the same sample, and they were arranged in the matrix with 5 rows and 10 columns, yielding the total of  $5 \cdot 10 \cdot 6 = 300$  cavities [Figure 3.14(d)]. In our experiments we tested several structures, but in this work we show results for three structures (total of 18 resonators). The structures are labelled  $a_2$ ,  $b_1$  and  $b_4$ , according to their position within 5x10 matrix of fabricated structures.

In Figure 3.15 we show scanning electron microscopy (SEM) micrographs of four cavities that lased, as described in the following section. In order to determine the exact geometry of these nano-laser, we performed detailed image-analysis of the SEM micrographs of these four cavities. We used pattern recognition procedure to determine the area of *all* holes that make photonic crystal mirrors, and to estimate the radius of each hole<sup>†</sup>. The results

---

<sup>†</sup>The details of pattern recognition procedure are discussed in Section 4 of this chapter

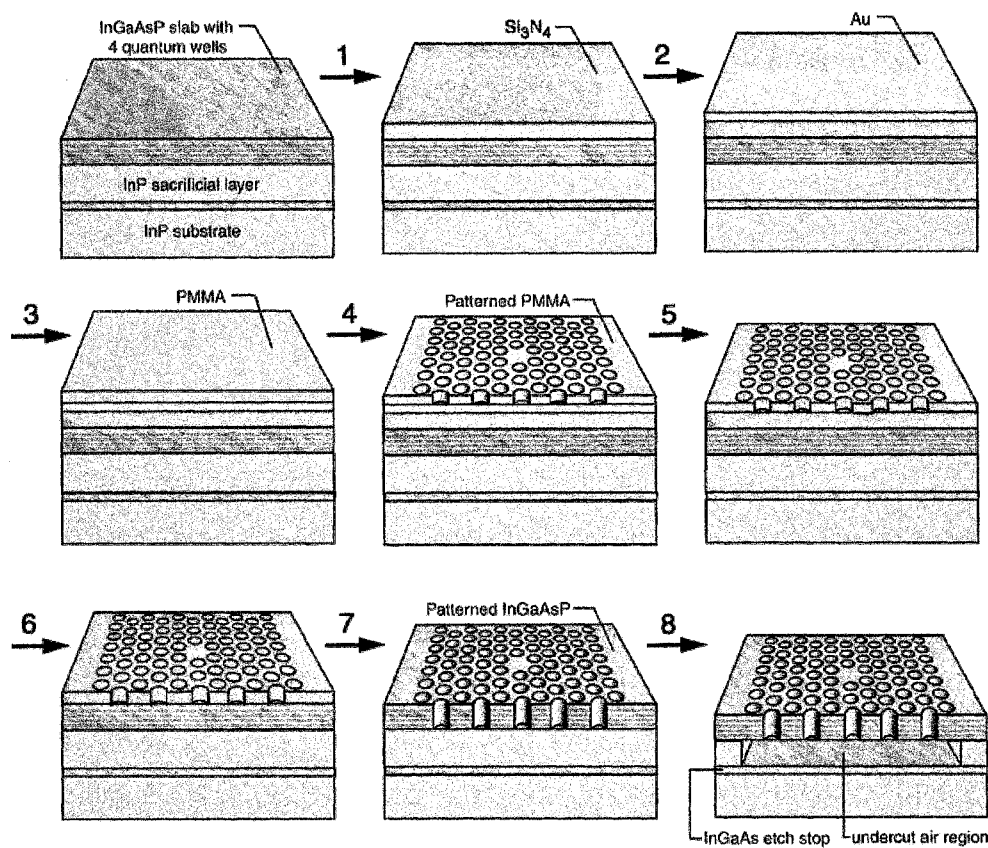


Figure 3.13: Fabrication procedure for PPC lasers made in InGaAsP material. RF sputtering (1) is used to deposit dielectric and is followed by deposition of Au mask (2). E-beam lithography consists of PMMA deposition (3), e-beam writing (3) and PMMA developing (4). Patterns are transferred from PMMA into Au using IBE (5) and then into Si<sub>3</sub>N<sub>4</sub> using RIE (6). Finally, cavities are etched into InGaAsP using ICP-RIE (7) and the membrane is released from the substrate in HCl (8). Final structure is a free standing InGaAsP membrane with four quantum wells (thin red layers).

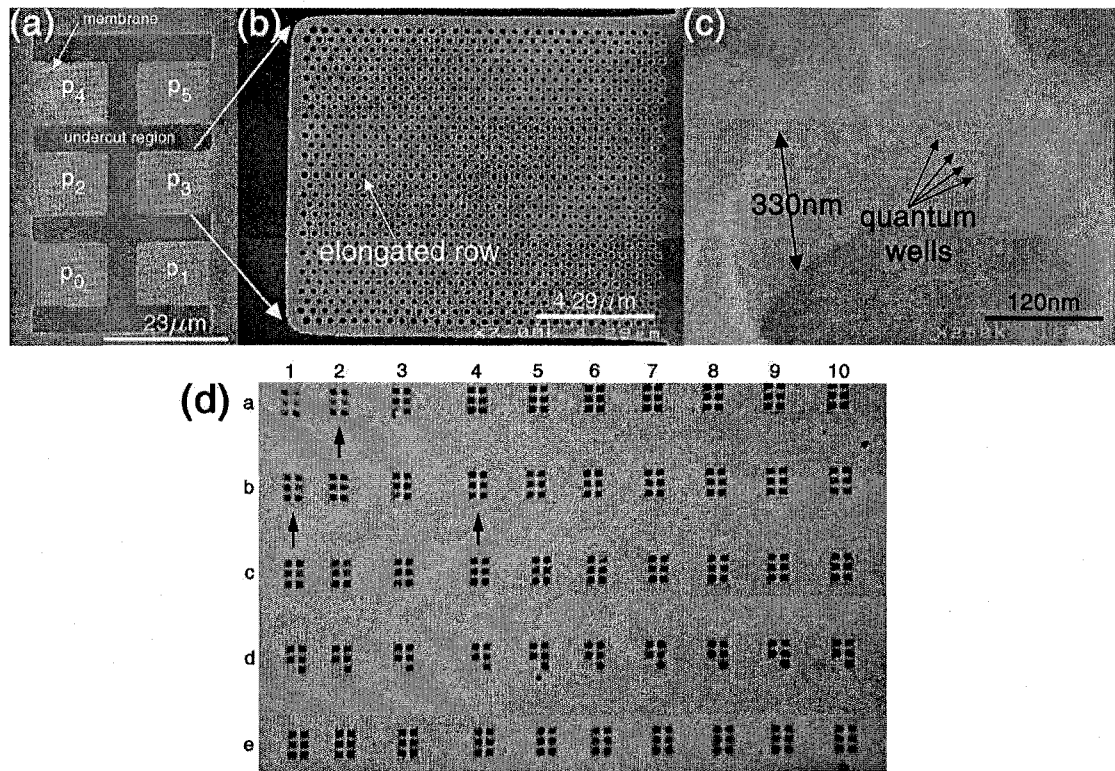


Figure 3.14: SEM micrograph of the structure  $b_4$ . Each structure consists of (a) six different cavities with different elongation parameters:  $p_0 = 0$ ,  $p_1 = 0.05 \cdot a$ ,  $p_2 = 0.1 \cdot a$ ,  $p_3 = 0.15 \cdot a$ ,  $p_4 = 0.2 \cdot a$  and  $p_5 = 0.25 \cdot a$ . (b) Blow-up of  $p_3$  cavity, and (c) of a single hole (tilted). Quantum wells and undercut air region can be seen. (d) Optical image of all 50 fabricated structures. Structures for which we show experimental data are indicated by arrows.

Table 3.4: Geometry of four nano-lasers tested in the experiment

	$r$	$r/a$	$r_{def}$	$r_{def}/a$
$a_2, p_4$	126 nm	0.290	$\approx 50$ nm	0.115
$b_1, p_5$	125 nm	0.290	$\approx 71$ nm	0.162
$b_4, p_5$	139 nm	0.320	$\approx 73$ nm	0.168
$b_4, p_4$	138 nm	0.317	$\approx 73$ nm	0.168

are shown in Figure 3.15 and summarized in Table 3.4. In case of  $b_4$  structure, that we show the most experimental data for, the average hole size is found to be  $r \approx 140$  nm, and average periodicity of the photonic crystal lattice  $a = 435$  nm. This geometry yields relative thickness of  $d/a = 0.76$  and relative hole size  $r/a = 0.32$ . This is slightly different geometry than the one that we analyzed in the Section 2 of this chapter. Due to increased hole size, Q-factors of fabricated structures are expected to be smaller than those reported in previous section. Moreover, Q-factors are expected to be even further decreased due to increased scattering of light at the rugged hole walls<sup>§</sup> (Figure 3.15).

### 3.3.2 Characterization of High-Q Cavities

Fabricated structures were tested at room temperature using micro-photoluminescence approach ( $\mu$ PL). Due to poor heat sinking in our membrane-based devices, optical pumping was performed in pulsed regime, with limited duty cycles. The experimental setup is shown in Figure 3.16. As the pump we used diode laser emitting at  $\lambda = 830$  nm. In most cases structures were pumped with 1% duty cycles, using 10ns pulses with  $1\mu s$  periodicity, or 30ns with  $3\mu s$  periodicity. The pump beam was focused through 100x objective lens onto the sample surface to obtain a spot size of about  $2.5 \cdot 1.5 \mu m^2$ . The emission from the cavities was collected through the same lens, and the spectrum of the emitted signal was analyzed with an optical spectrum analyzer (OSA). Flip-up mirrors were used to obtain the optical images of the excitation pump-spot and the cavity modes.

---

<sup>§</sup>The fabrication procedure can be improved/simplified by using chemically assisted ion beam etching (CAIBE) instead of combination of RIE and ICP RIE. Cl-based CAIBE is known to have good selectivity of etching between InGaAsP and PMMA, when etching is done at higher temperatures ( $\approx 200^\circ C$ ).

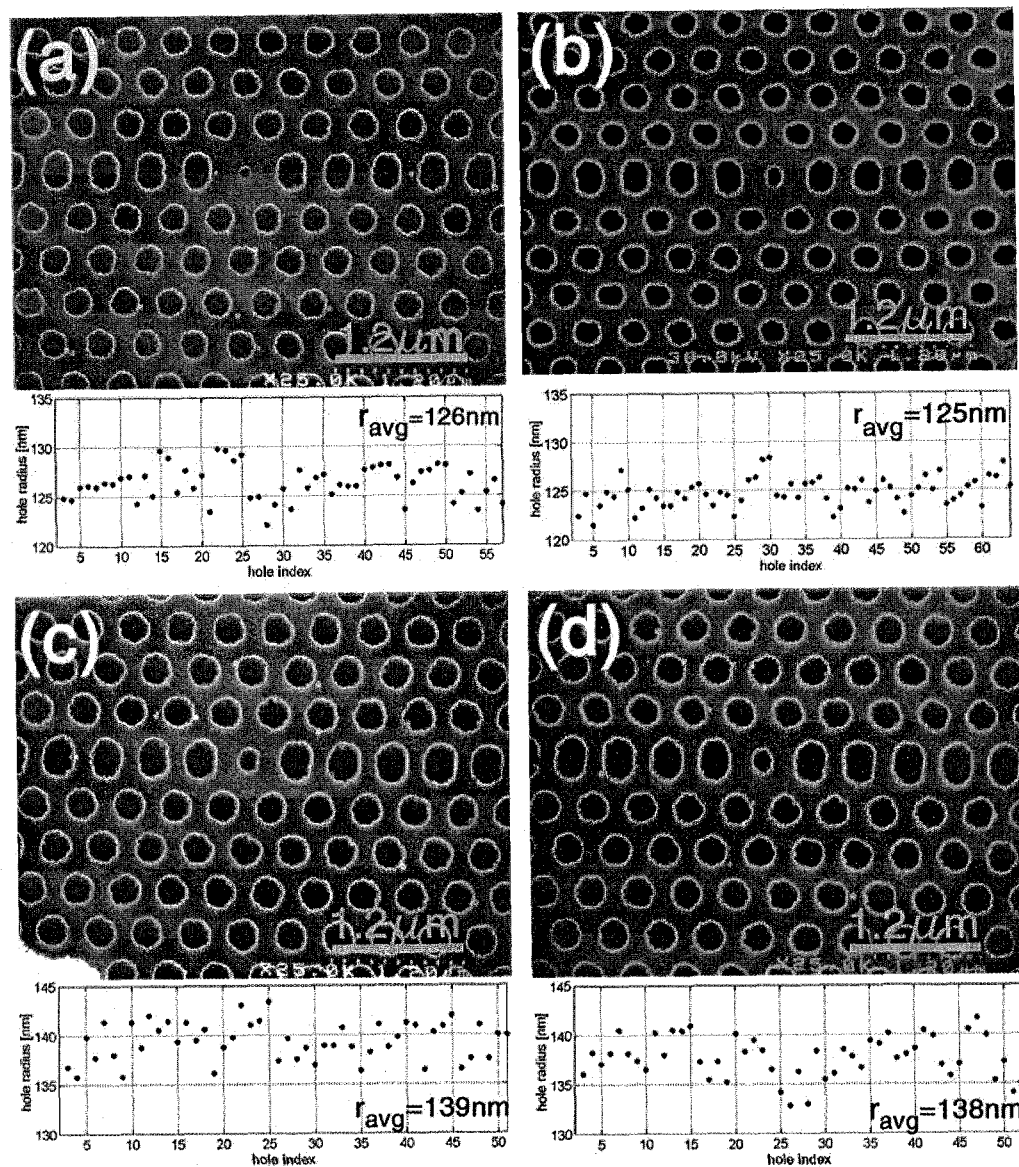


Figure 3.15: SEM micrographs of (a)  $a_2 p_4$ , (b)  $b_1 p_5$ , (c)  $b_4 p_4$  and (d)  $b_4 p_5$  along with the distribution of hole sizes in the bulk photonic crystal mirrors surrounding each cavity.

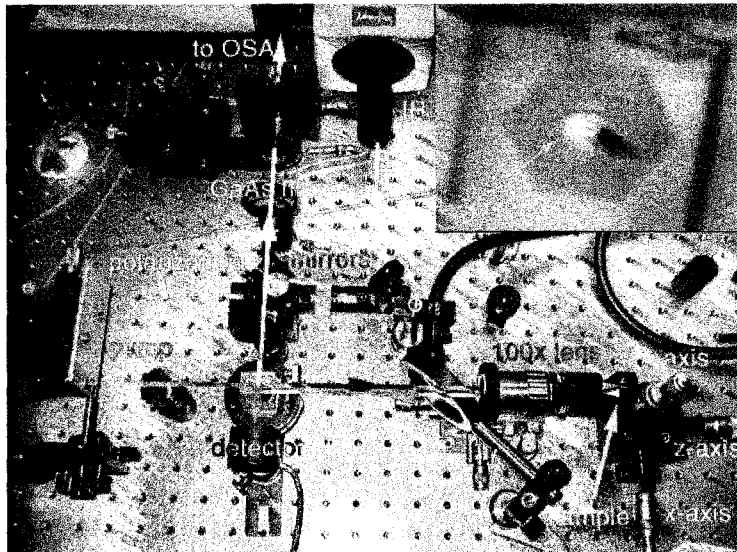


Figure 3.16: Experimental setup. Pump beam ( $\lambda = 830$  nm) is focused on the sample using high-power NIR lens (100x). Si detector behind beam splitter (BS) is used to monitor the pump power. Emission from the sample is collected using the same lens, and is analyzed with an optical spectrum analyzer (OSA). The emission from photonic crystal resonators can also be monitored with an infrared camera (IR) using a pair of flip-up mirrors. Inset shows the size of the pump beam.

First we measured the emission from the unprocessed InGaAsP material and obtained the gain spectrum of the active material. We found that emission exists between 1300 nm and 1650 nm, with a maximum at around 1550 nm [Figure 3.17(a)]. Assuming the lattice constant of  $a = 436$  nm (as in the case of the most of the fabricated structures) this wavelength range corresponds to normalized frequencies of  $a/\lambda \in (0.264, 0.335)$ , which is within the bandgap of the bulk photonic crystal mirrors surrounding the cavity. The emission from the quantum wells is modified when the slab is suspended in the air, even without presence of the PPC lattice. Fabry-Perot resonances observed in Figure 3.17(b) are due to cavity formed between etched facets of the membrane.

As the next step we tested all six cavities in  $b_4$  structure in order to characterize their resonant modes. We found two prominent resonant peaks in these cavities, all positioned within the bandgap of photonic crystal mirror<sup>¶</sup> (Figure 3.18). We also observed that the

---

<sup>¶</sup>Relatively large linewidths of the resonances are due to the resolution bandwidth of OSA in this case ( $RB = 5$  nm). When measurements are taken with smaller resolution ( $RB < 1$  nm), linewidths are much narrower and limited by the Q of the cavities.

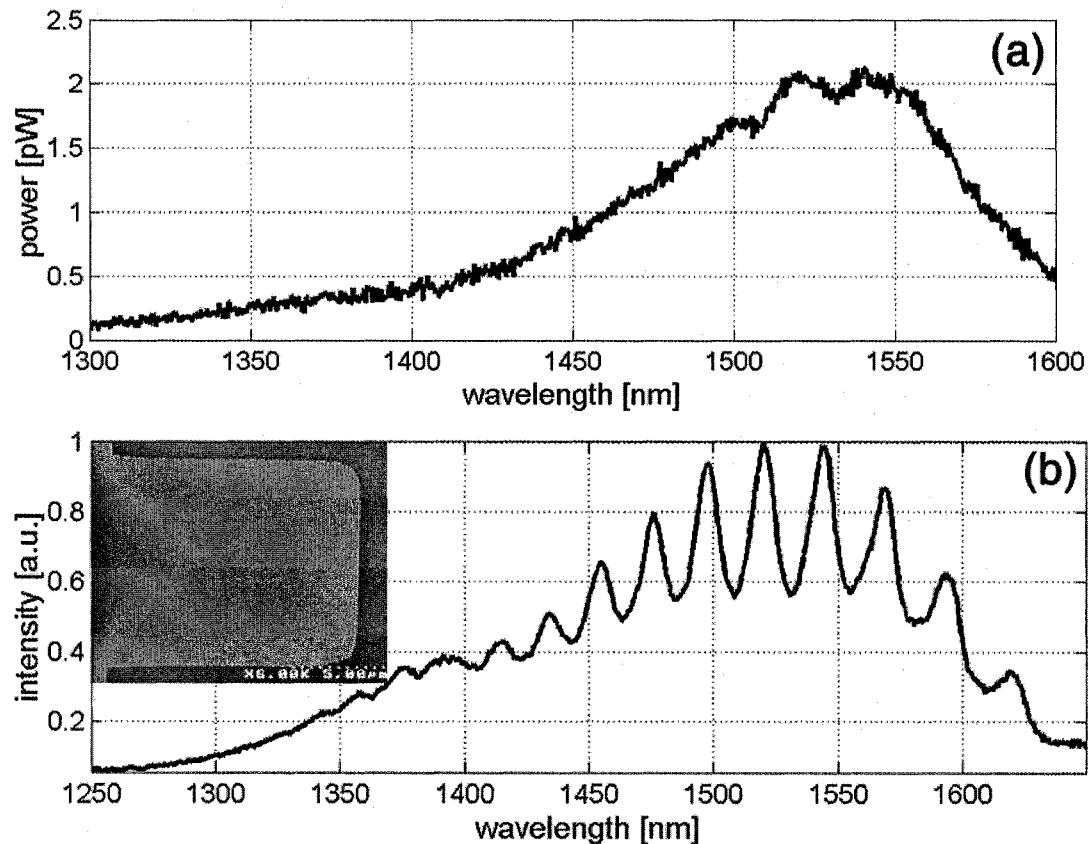


Figure 3.17: (a) Emission from unprocessed InGaAsP material and (b) from rectangular membrane suspended in air. Fabry-Perot resonances, due to rectangular cavity formed between etched facets, can be seen.

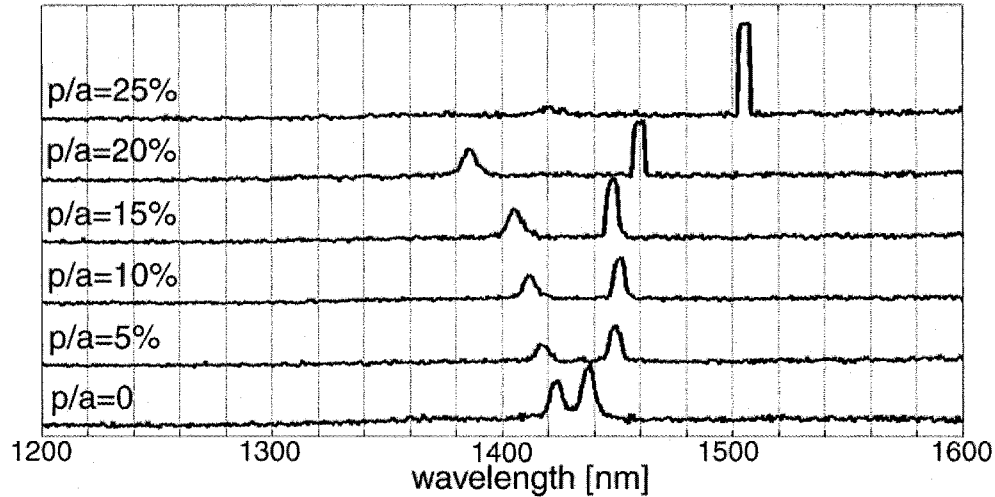


Figure 3.18: Structure  $b_4$ . Position of resonant modes detected in cavities  $p_0 \div p_5$  as a function of the elongation parameter  $p$ .

positions of these resonances depend strongly on the value of the elongation parameter  $p$ . This is the signature of the HQ and LQ modes of our cavity, as observed in theoretical treatment presented in previous section. Originally double degenerate dipole modes of a simple single defect cavity ( $p_0$ ) become split apart as dislocation is introduced, and the splitting between two modes increases as amount of dislocation increases. LQ mode positioned at higher frequencies (shorter wavelength) is shifted towards shorter wavelengths, while HQ mode is shifted towards longer wavelengths, as the central row becomes more stretched. The experimentally observed mode-splitting is the signature of HQ and LQ modes of the cavity, and is the first indication that observed resonances correspond to HQ and LQ modes. Slight variations in the case of structure  $p_5$  (peaks jump towards longer wavelengths) might be attributed to the non-uniform defect hole size. Indeed, as we observed in previous subsection, positions of HQ and LQ resonances are strongly dependent on the defect hole size. In addition, LQ and HQ modes are split even in the case of  $p_0$ , even though theory predicts double-degenerate modes in that case. This can be attributed to the broken symmetry of the structure due to the fabrication-related disorders.

In previous section we predicted that HQ and LQ cavity modes are linearly polarized with orthogonal polarizations. In order to verify that observed resonances are HQ and LQ modes of the cavity, we checked their polarization properties. By introducing polarization

plate into the PL signal path (Figure 3.16) we could analyze polarization of the emitted photoluminescence signal. The results are shown in Figure 3.19. It can be observed that two resonances are linearly polarized with orthogonal polarization. Moreover, the mode at longer wavelength (smaller frequencies) is polarized along x-axis, and the one at shorter wavelength along y-axis, as expected in the case of HQ and LQ mode, respectively. In Figure 3.19 we also show the position of the two modes as calculated using 3-D FDTD method. The results of numerical analysis are in excellent agreement with experiments, and they predict existence of the HQ and LQ modes at almost exactly the same wavelengths as the ones found experimentally. Bigger linewidths observed in numerical simulation are due to the methodology of FDTD algorithm<sup>||</sup>. However, agreement between theory and experiments is still very good.

Based on the polarization properties of the observed resonances, their strong dependence on the amount of stretching of the central row, their position within the bandgap of photonic crystal mirror as well as an excellent agreement with theoretical predictions, we conclude that the resonances that we observe are localized dipole modes of our nanocavity. The resonance at shorter wavelength is LQ mode of the cavity, and the one at longer wavelength is the HQ mode. According to theoretical predictions, for  $r_{def} \approx 0.15a$  (the case of fabricated structures), the Q is maximized when  $p = 0.25a$ . Therefore, we expect that the cavity  $p_5$  has the highest Q factors of all the fabricated structure and it is the best candidate for realization low-threshold laser.

### 3.3.3 Room Temperature Laser

As the next step, we investigated the dependence of the PL signal on the input pump power. In order to prevent overheating, the structures were pumped with limited duty cycles (1% – 3%). Since our cavities have high Q factors and very small mode volumes it is expected that the lasing action will occur even at the room temperature. In Figure 3.20 we show the dependence of detected peak output optical power as a function of peak input optical power - light-light (L-L) curve - for HQ resonant mode of  $p_5$  cavity in structure  $b_4$ .

---

<sup>||</sup>In order to have sufficient resolution in frequency domain, many time-steps are needed and FDTD simulation needs to be done for a long time (e.g., days/weeks). In most cases this is not practical and shorter calculations are performed, resulting in poor frequency resolution

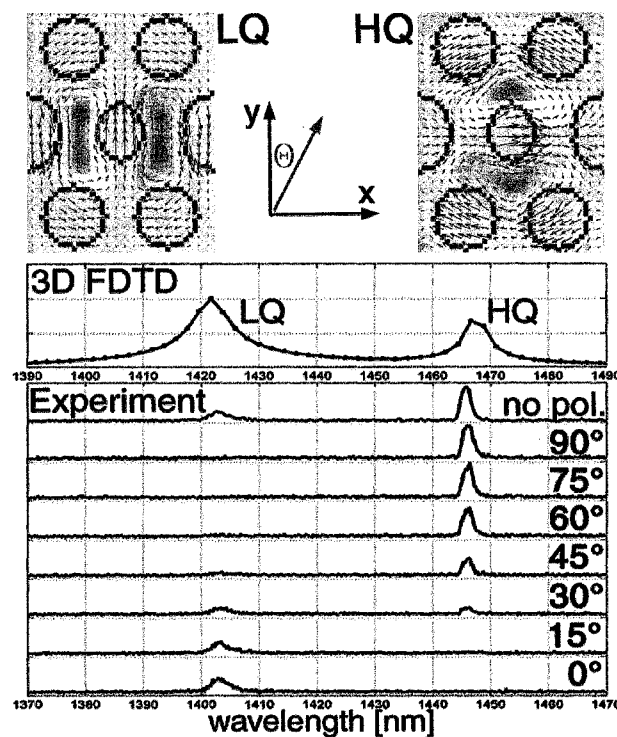


Figure 3.19: Structure  $b_4$ , cavity  $p_3$ . Polarization dependence of the resonant modes.  $0^\circ$  corresponds to the y-axis direction. Figure also shows mode profiles ( $B_z$  component), polarization ( $\vec{E}$ ) and position in the spectrum of the LQ and HQ modes, the result of 3-D FDTD analysis.

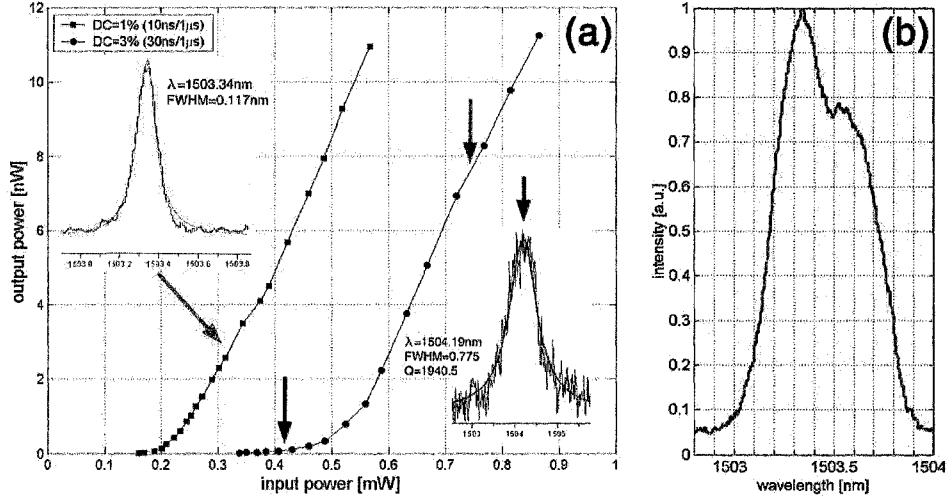


Figure 3.20: Cavity  $b_4$ ,  $p_5$ . L-L curve for two different duty cycles (DC). The pulse periodicity was  $1\mu\text{s}$  in both cases. Spectra taken above threshold for  $DC = 1\%$  (red) and below threshold for  $DC = 3\%$  (black arrow) are shown as insets. (b) Wavelength chirp in case of  $DC = 3\%$ .

The peak input power is the amplitude of the pump beam at the sample surface. The reflection from the sample is not taken into account, and actual power that “pumps” quantum wells is smaller. This is important to keep in mind when comparing pump powers reported in literature. When structure  $p_5$  is pumped with 1% duty cycle characteristic lasing curve is observed, with the threshold power as low as  $P_{th} = 214\mu\text{W}$ . In the same figure we show the spectra above the threshold. The linewidth above the threshold is reduced to only 0.117 nm, and was limited by the resolution of or OSA (0.1 nm). The existence of the threshold and linear region in L-L curve, and the linewidth narrowing above the threshold are indication of the lasing action in our nanocavities. Therefore, we conclude that the cavity  $p_5$  in structure  $b_4$  is lasing when pump power is bigger than  $214\mu\text{W}$ . This is the smallest threshold power reported so far in the case of photonic crystal lasers based on quantum well materials.

When duty cycle is increased to 3%, the threshold power increases to  $520\mu\text{W}$ . We have attributed this increase in the threshold power to poor heat dissipation of our nano-laser and its increased temperature. Quality factor in the case of  $p_5$  structure was estimated from below threshold luminescence measurements to be around  $Q \approx 2,000$  (Figure 3.20). How-

ever, it should be mentioned that by estimating Q factors of the cavity from below-threshold characteristics, we **underestimate** actual Q-value. This is due to additional losses introduced in the cavity due to the re-absorption of light in the active region (quantum wells). We expect actual Q-values to be higher and in the range of 6,000 as predicted by theory. In Figure 3.20(b) we show the spectrum of the lasing HQ mode above the threshold when  $DC = 3\%$ . Wavelength chirping is apparent, and is most likely due to the overheating of the sample when cavities are pumped with high power, or due to the variation of the refractive index due to the carrier dynamics, when structures are pumped with longer pulses (30ns in this case).

In Figure 3.21 we also show L-L curve for  $p_4$  cavity in the  $b_4$  structure. It can be seen that threshold is higher in this case, and it is around  $P_{th} = 950\mu W$ . There are several reasons for increased threshold: gain provided from quantum wells is smaller at this wavelength ( $\lambda = 1457.5$  nm) than in the case of  $p_5$  cavity ( $\lambda = 1504$ ) since gain peaks at  $\lambda \approx 1550$  nm; second, for  $r_{def} \approx 0.15a$  Q factor of  $p_4$  cavity is smaller than Q factor of  $p_5$ , as shown in Section 2; finally,  $p_5$  structure has more dielectric material in the cavity region (bigger dislocation), and the mode-overlap with the gain material is better than in the case of  $p_4$  structure. In the inset of Figure 3.21 we show spectrum of the HQ peak of the  $p_4$  cavity (set  $b_4$ ), taken at the threshold. Full-width half-maximum of the resonance is  $FWHM = 0.34$  nm, and that corresponds to Q factor of  $Q \approx 4,300$ . This is in good agreement with our theoretical predictions of  $Q_{p4} = 4,000$ . However, since the spectrum is taken at the threshold, it is possible that the linewidth is narrowed due to gain provided by quantum wells. Therefore, this high Q value that we measure should be taken with caution, and more detailed analysis needs to be conducted in order to get reliable estimates for Q-factors. For example, structures defined in passive materials (e.g., SOI) can be characterized in order to get unambiguous estimates of Q-factors.

Based on the experimental results presented so far, we can conclude that in spite of the unusual design of our nanocavities (air hole pierced at the center of the laser where the cavity field is the strongest) and reduced overlap with the quantum well (gain) region, our structures lase at low threshold powers. We have attributed this to high quality factors and small mode volumes of our cavities (big  $Q/V_{mode}$  factor). In order to even further reduce threshold powers, it is beneficial to increase Q of the cavities. This can be accomplished by

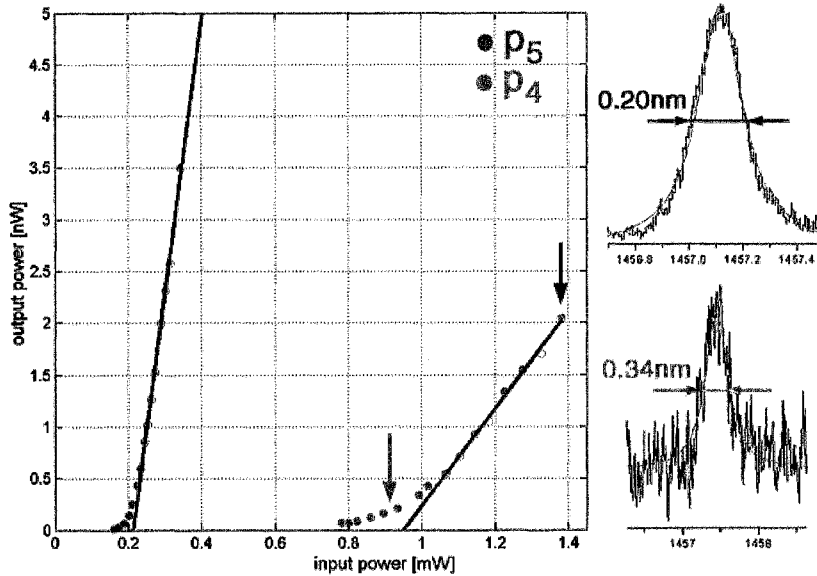


Figure 3.21: Cavity  $b_4$ . L-L curves for structures  $p_5$  and  $p_4$  pumped with  $DC = 1\%$ . Reduced differential quantum efficiency in the case of  $p_4$  structure is due to the smaller Q factor. Spectra for  $p_4$  structure, at and above threshold, are also shown.

reducing the size of photonic crystal holes and thereby reduce out-of-plane scattering. In addition, the defect hole should be made smaller in order to increase mode overlap with the dielectric and increase the gain in the cavity. As it can be seen in Table 3.4, cavity  $p_5$  from set  $b_1$  satisfies these conditions. Therefore, we expect to observe small threshold power in the case of this cavity. In Figure 3.22 we show the positions of the resonant modes in the cavity  $b_1 p_5$ . The spectra are taken for two different pumping levels, and line-narrowing can be observed as laser is pumped harder. It can be seen that HQ resonance is positioned at  $\lambda = 1560$ , almost exactly at the position of the maximum gain ( $\lambda = 1550$  nm). Q-factor of the LQ mode was estimated to be  $Q_{LQ} = 505$ . In Figure 3.23 we show L-L curves for this structure, taken on two different days. It can be seen that threshold power in this structure is smaller than in the case of structure  $b_4$ ,  $p_5$  shown in Figure 3.20.

In Figure 3.24 we show L-L curve for  $a_2$   $p_4$  cavity, as well as tuning characteristics of structure  $a_2$ . This cavity also supports two modes, and the one at longer wavelength (HQ mode) lases. Since both holes in the bulk photonic crystal mirror surrounding the cavity and the central defect hole are smaller in this case (Table 3.4), resonances are shifted towards longer wavelengths. A photoluminescence spectrum taken above threshold, as well

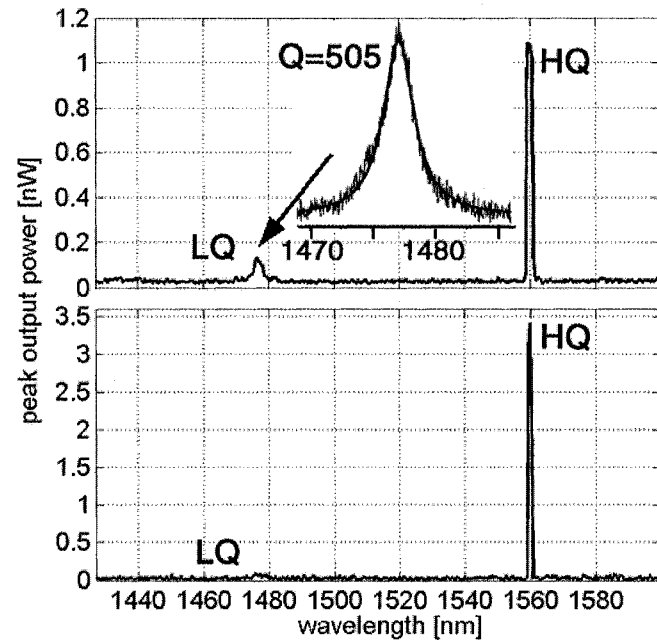


Figure 3.22: Structure  $b_1$ , cavity  $p_5$ . Photoluminescence spectra taken at (a) low and (b) high pumping levels. Linewidth narrowing (HQ mode) and gain clamping can be observed. Q-factors of LQ mode are estimated to be around  $Q_{LQ} = 505$ .

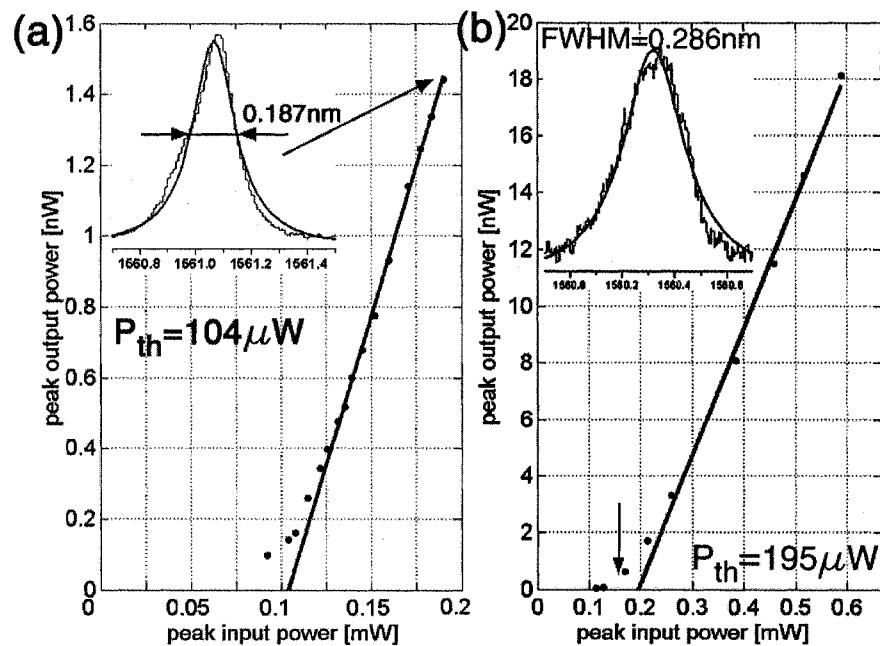


Figure 3.23: L-L curve of structure  $b_1$   $p_5$  taken at different pumping levels.  $DC = 1\%$ .

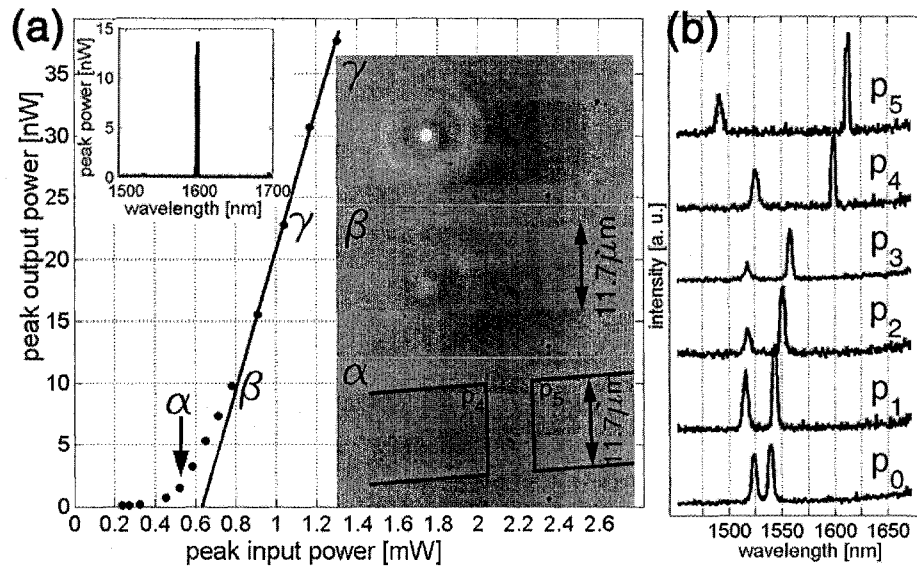


Figure 3.24: Structure  $a_2 p_4$ . (a) L-L curve. Lasing action occurs from HQ mode positioned at  $\lambda = 1598$  nm. Insets show spectrum above threshold, and mode profiles of the lasing mode for several pump levels. The boundaries of the structure can also be seen. The mode is very well localized to the center of the cavity. (b) Tuning properties of  $a_2$  structure, as a function of the elongation parameter  $p$ .

as the mode profiles taken at different pumping levels, are shown in the inset. The size of the light spot emitted from the nano-laser is on the order of  $3.9\mu\text{m}^2$ , a strong indication that this laser has a small mode volume. When the pump beam is only slightly moved from the center of the cavity (less than  $1\mu\text{m}$ ), the strong signal shown in Figure 3.24 disappears. This result is qualitative confirmation that we are indeed observing well-localized, small mode-volume, resonant mode of our nanocavity. In order to obtain quantitative estimation of the mode size as well as an image of the mode profile near field scanning optical microscopy (NSOM) can be used as a powerful tool.<sup>66</sup>

### 3.4 Photonic Crystal Lasers as Chemical Sensors

The construction of compact spectroscopic tools for the optical analysis of ultra-small ( $< 10^{-15}$  liter) sample volumes remains an important goal in the development of integrated

microfluidics systems. Miniaturization of appropriate light sources and detectors can enable very compact and versatile “laboratory on a chip” devices, in which many analytical functions can be monolithically combined. One of the device integration platforms which is ideally suited to enable such integration of ultra-small and efficient optical components is the membrane based planar photonic crystal, defined in high refractive index contrast materials by standard lithography and semiconductor fabrication processes. Compact lasers, high-Q cavities, waveguides and prisms have been fabricated and demonstrated in semiconductor slabs of silicon, GaAs or InGaAsP. These devices have been used to generate, concentrate and route light efficiently within nanophotonic chips.

So far, the applications of planar photonic crystals have been restricted to large-scale integration of optical wavelength division multiplex (WDM) components for telecommunications. Here, we propose application of planar photonic crystal cavities in the development of chemical sensors, with high spectral resolution and excellent sensitivity to changes in the absorption or refractive index of their surrounding. By combining an unconventional cavity geometry with optical gain at 1550 nm, we have defined ultra-small sensor elements which can emit a very narrow spectrum. Our porous cavity design permits the introduction of analyte directly into the high optical field of the laser cavity, and, due to the ultrasmall mode volume of our lasers, permits the sensitivity to optical changes within femtoliter volumes. The introduction of absorbing or fluorescing molecules into such cavities is expected to have a large influence on the optical signature, and the high fields obtained in the cavity can be used for spectroscopy of the cavity contents (e.g., Raman or absorption spectroscopy). This will enable the sensing and analysis of individual organic molecules or self-assembled quantum dots, and offers a unique opportunity to achieve strong interaction between light and molecules on a nano-scale level. We propose to use these lasers for high-resolution spectroscopy with single-molecule sensitivity.

The cavity geometry that we have chosen for our chemical sensors is based on a fractional edge dislocations introduced in the previous sections. The cavity design is shown again in Figure 3.25 and it can be seen that the energy of the mode is mostly confined to the central defect hole. In order to increase the interaction between light and the material within that hole, a larger defect hole diameter is preferred. However, increase of the hole size reduces the gain provided by the light emitting quantum wells within the laser cavity and thereby increases the threshold of our laser. Therefore, a trade-off between the optical

overlap with the analyte cavity and the optical gain is needed, as pointed out in section 2 of this chapter. We decided to use the cavity with  $r/a = 0.3$ ,  $d/a = 0.75$ ,  $r_{def}/a = 0.15$  and  $p/a = 0.25$  since this design was shown to have reasonably high Q while maintaining small defect hole size.

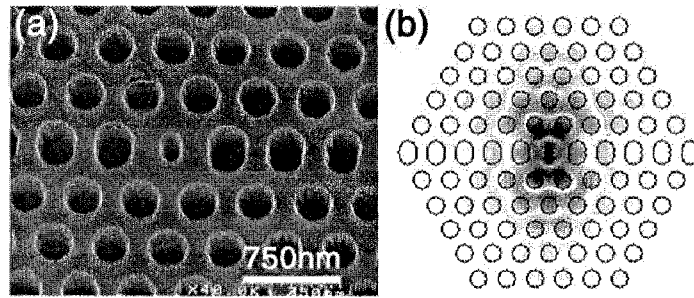


Figure 3.25: Scanning electron micrograph and calculated field distribution of a photonic nanocavity laser sensor.

### 3.4.1 Fabrication of Photonic Crystal Bio-Chemical Sensors

To demonstrate our biochemical sensors, photonic crystal nanolasers were fabricated in the same InGaAsP quantum well material as the one described in previous section (Table 3.2). Optical gain was provided by four 9 nm thick, compressively strained quantum wells, placed in the center of a 330 nm thick InGaAsP slab. The emission from the quantum wells was in the range  $\lambda \in (1300, 1600)$  nm, and these were embedded within a free standing membrane, patterned with a photonic crystal lattice. This time, we controlled the precise emission wavelength either by scaling the lattice parameter, or by changing the size of the defect hole introduced into the lattice to form the cavity. The structures were tested using micro-photoluminescence approach, and were optically pumped at room temperature with 30ns pulses of  $3\mu s$  periodicity ( $\lambda_{pump} = 830$  nm). In this work we used the same photoluminescence setup as the one described in the previous section.

Fabrication procedure was slightly modified in order to improve the quality of fabricated structures. In this case, the RIE process was modified by replacing  $C_2F_6$  gas with  $CHF_3$ .  $CHF_3$  is known to have good etch selectivity between  $Si_3N_4$  and PMMA. Therefore, we

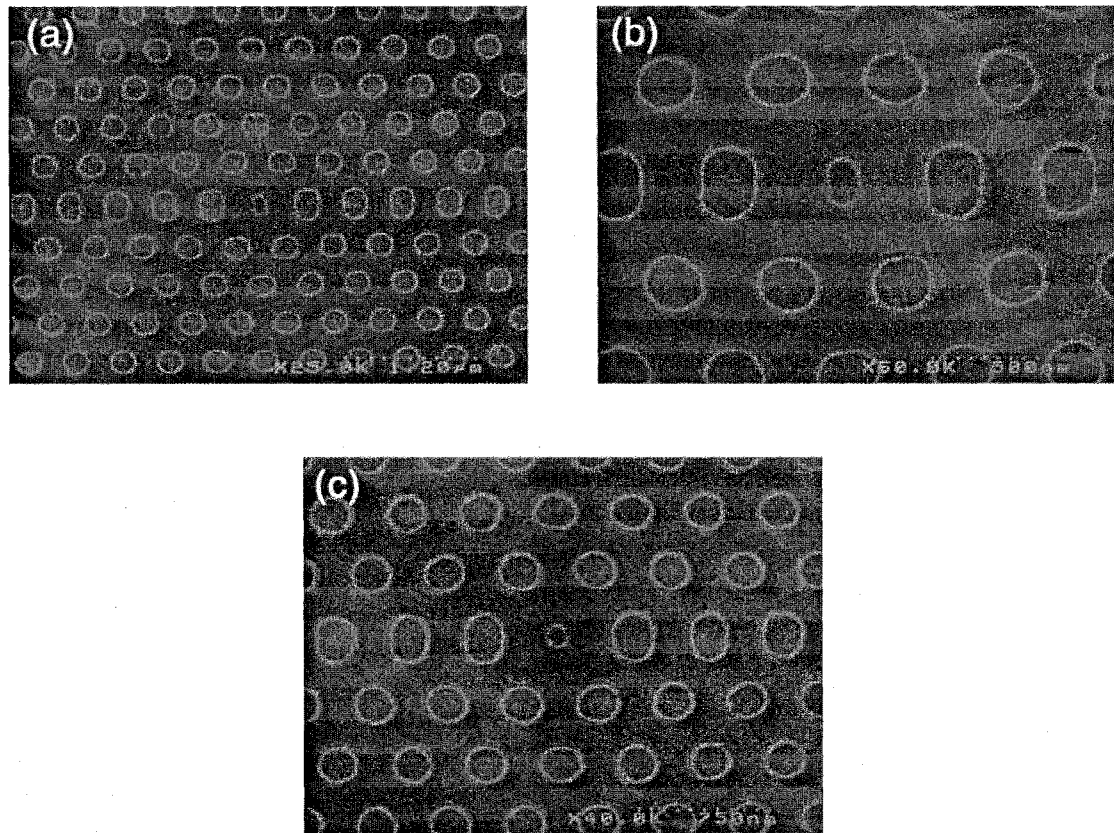


Figure 3.26: SEM micrograph of structures B: $r_2c_5$  (a, b) and C: $r_5c_2$ small (c) after reactive ion etching using PMMA as the mask and  $CHF_3$  as the reactive gas.

were able to etch  $Si_3N_4$  using PMMA as the only mask, and *problematic* Au layer and milling step were not necessary any more. Patterns were again defined in PMMA by means of e-beam lithography and then they were transferred into  $Si_3N_4$  using RIE. 20 sccm of  $CHF_3$  reactive gas was used and chamber pressure was kept at 16 mTorr. RF power used in this RIE step was 90 W and built-up DC voltage was  $U_{DC} = 480$  V. The etch was done for 3 minutes. Results of this improved RIE step, for several structures that we have tested experimentally, are shown in Figure 3.26. It can be seen that the quality of the etch has improved, but some PMMA erosion is still present. Finally, patterns are transferred from  $Si_3N_4$  into InGaAsP using ICP RIE using the same conditions as in the previous section. The membrane was released from the substrate using HCl.

In order to make structure more mechanically robust and less susceptible to the vibrations, we have redesigned the trenches around the cavity so that the membrane is supported

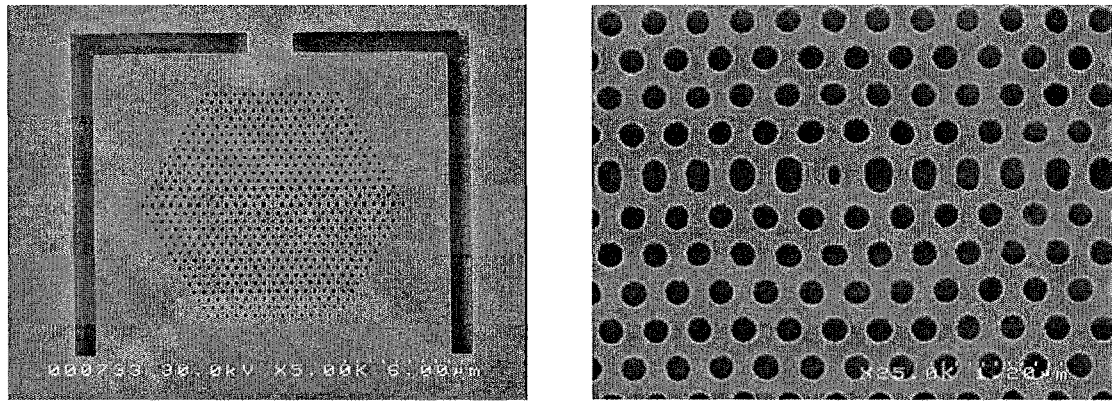


Figure 3.27: SEM micrograph of high-Q planar photonic crystal cavity, defined in the suspended membrane.

at two sides (Figure 3.27). Since HCl attacks sacrificial InP layer only along well defined crystal plains, undercutting of the structures that are supported at both sides turned out to be more complicated. In some situations it was impossible to remove InP completely underneath the membrane. This can be seen as light gray region underneath the membrane in Figure 3.28 and at the bottom and top of the figure. This is particularly serious problem in the case of structures with small photonic crystal holes. This problem can be fixed by beam-writing the patterns at angles different from major crystal planes.

As shown in the previous sections, the properties of photonic crystal devices depend strongly on the periodicity of the lattice but also on the size and shape of all the holes in the photonic crystal lattice. Therefore, it is necessary to control these parameters and to minimize fabrication related disorders. In order to quantitatively characterize the quality of our fabrication process we have used simple pattern recognition technique. The procedure is based on detection of the edges of photonic crystal holes in the SEM image of the structure. Panels (b) and (c) in Figure 3.29 show the holes detected in SEM micrograph shown in Figure 3.27(a), and panel (d) shows distribution of the hole radii. The radius of each hole is estimated by calculating the area of the hole, assuming the circular shape of the holes. The average lattice constant is estimated as the average periodicity in each row of holes shown in Figure 3.29(c). The resolution of this procedure ultimately depends on the resolution of

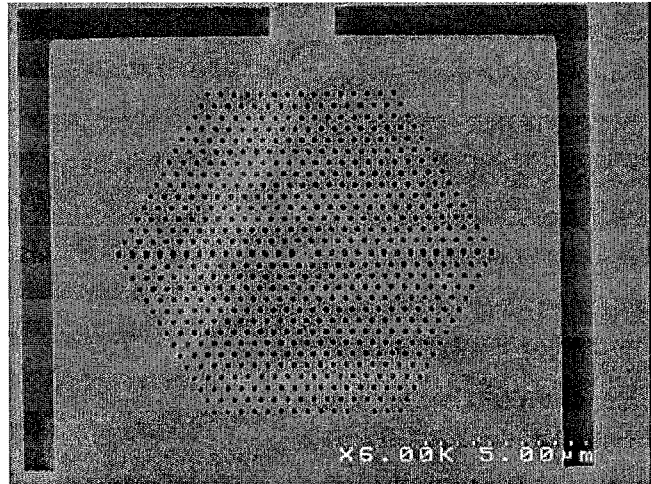


Figure 3.28: Membrane not completely released from the substrate. The light gray region at the bottom and top of the figure, as well as the diagonal line at the left side of the figure are regions where sacrificial InP was not completely removed. Q-factors can be spoiled significantly if non-undercut region is close to the cavity region.

the SEM image, as well as on the magnification used to obtain the SEM image. In case of Figure 3.29(a) the resolution was  $\approx 4$  nm. As it can be seen fluctuation of the hole radius ( $\approx \pm 4$  nm) and that is within the resolution of our technique. A quasi-periodic fluctuation of the hole size observed within each row (hole in the middle of the row are slightly bigger than the holes at the ends of the row) can be attributed to the proximity effect - the holes in the center receive bigger effective dose. This can be corrected by reducing the size of the holes or the dose that holes in the center receive. By comparing the quality and uniformity of these fabricated structures with those described in the previous section (Figure 3.15) we conclude that new fabrication procedure has much better uniformity and reproducibility.

Our simple hole-detection procedure can be used to compare theoretical and experimental results for our high-Q cavities. For example, we used the information from Figure 3.29(c) to generate an input structure for 3-D FDTD algorithm and to numerically model *real* structure, with all imperfections taken into account. Then, the only discrepancy between experimental and numerical results comes from the discretization of FDTD algorithm and the assumption that the walls in our etched structures are straight.

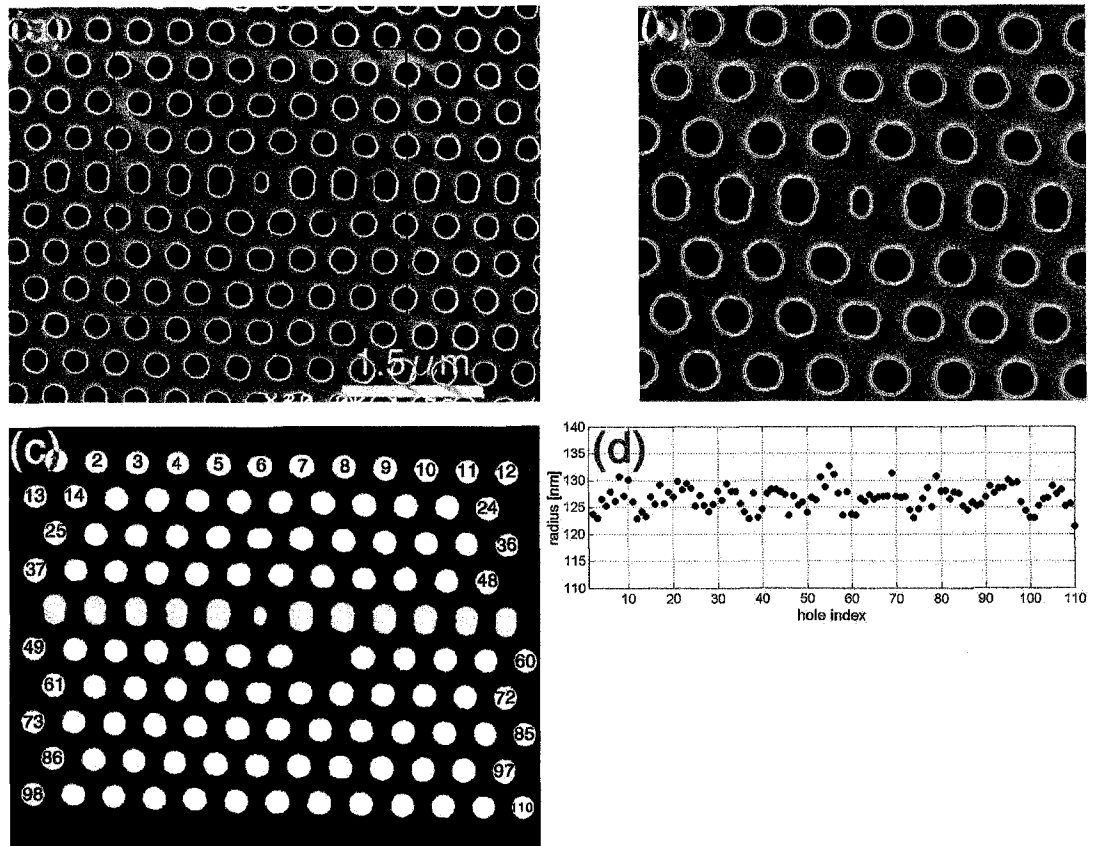


Figure 3.29: Pattern recognition. (a) SEM micrograph of one of the structures. (b) Blow-up of the region indicated by square. Edges of the holes detected in this step are shown in red. (c) Detected holes are shown in white and their area is calculated and used to estimate (d) the radius of each hole.

### 3.4.2 Chemical Sensing

Our porous cavity design permits the introduction of analyte directly into the high optical field of the laser cavity. When the overlap between that introduced analyte and the optical field generated in the laser cavity is optimized, the sensitivity of a fabricated nanocavity sensor can be maximized. Photonic crystal nanocavities can support high optical fields with very small mode volumes, and such structures are expected to be ideal for the analysis of reagent volumes below  $10^{-16}$  liters. The introduction of absorbing or fluorescing molecules into such cavities is expected to have a large influence on the optical signature, and in turn the high fields obtained can be used to excite nonlinear effects and can be used for spectroscopy on the cavity contents.

The simplest method of optically sensing ambient material uses wavelength shifts in the laser spectrum to measure refractive index of ambient. In this method, the sensitivity of the sensor depends on the smallest change in refractive index that can be optically detected. In *passive* devices, this is related to the width of the cavity resonance peak which in turn is determined by cavity quality  $Q$ . However, a laser linewidth can be much narrower than the passive cavity resonance, and even smaller shifts in the lasing wavelength can be detected by taking advantage of the spectral narrowing from stimulated emission above laser threshold.

To test the influence of a change in ambient refractive index on the laser spectrum of a cavity, we have backfilled our photonic crystal lasers with isopropyl alcohol and methanol. Figure 3.30 shows position of the resonances from six different lasers after immersion in air, isopropyl alcohol (IPA) and methanol. It can be seen that wavelength shifts of up to 67 nm can be observed when a cavity is immersed in IPA. This red-shift corresponds to a change in refractive index from 1.0 to 1.377, and yields roughly 1 nm spectral shift for a 0.0056 change in refractive index. When IPA is replaced with methanol ( $n = 1.328$ ), the laser resonance experiences a blue shift of  $\approx 9$  nm, which is again in good agreement with predicted shift of  $\approx 13$  nm from our theoretical predictions (Figure 3.8). We have also investigated the dependence of the cavity resonance wavelength on the lithographic laser geometry, particularly the lattice constant ( $a$ ) and the dislocation ( $p/a$ ) in the photonic crystal cavity. Resonances experience red shifts of  $\approx 80$  nm when the periodicity is changed from  $a = 446$  nm (dashed lines) to  $a = 460$  nm (solid lines). This lithographic tuning of the emission wavelength can be used to ensure an overlap of the cavity resonance peak with the InGaAsP quantum

well emission gain curve even when the cavities are immersed in a reagent. Laser threshold curves before and after immersion into alcohol are also presented in Figure 3.30. After immersion, the laser threshold power for the cavity measured was reduced since the emission wavelength was shifted to match the maximum gain of the quantum wells. However, the differential quantum efficiency of the immersed cavity is slightly lower, which may reflect the lower laser cavity Q after immersion.

In order to explore the sensitivity of our lasers on the changes in the refractive index of environment we used fluids with known refractive index\*\*, in the range  $n_{env} \in (1.295, 1.335)$  (specified at  $\lambda = 1.5 \mu m$ ) with step  $\Delta n_{env} = 0.005$ . A new sample was fabricated, with total of 9x8 cavities [nine rows (R) and eight columns (C)]. Here we report the results for three different cavities, labelled  $R_6C_5$ ,  $R_7C_5$  and  $R_7C_3$  according to their position within the 9x8 matrix. Cavities in column 5 ( $C_5$ ) have fractional edge dislocation  $p/a = 20\%$ , whereas cavities in column 3 ( $C_3$ ) have dislocation of  $p/a = 10\%$ . Structures in row 6 ( $R_6$ ) have lattice constant  $a = 427 \text{ nm}$ , and structures in row 7 ( $R_7$ ) have lattice constant  $a = 454 \text{ nm}$ . In Figure 3.31(a) we show dependence of the frequency of the resonant HQ mode as a function of the refractive index of environment ( $n_{env}$ ). It can be seen that frequency shifts depend linearly on  $n_{env}$ , as predicted by numerical analysis presented in Section 2. The experimentally obtained sensitivities (slopes) are in good agreement with numerical results. However, 3-D FDTD result presented in Section 2 is obtained for structure with  $p/a = 25\%$  and therefore direct comparison between our numerical and experimental results is not possible. Also, shifts that the cavity resonances experience when  $n_{env}$  is changed will depend strongly on the size of the holes in PPC mirror ( $r/a$ ) as well as on the size of the defect hole ( $r_{def}/a$ ). For example, it is expected that structure with bigger  $r/a$  will be more sensitive to the changes in  $n_{env}$ ††.

While relation between  $a/\lambda$  and  $n_{env}$  is useful for comparison between theory and experiments, relation between  $\lambda$  and  $n_{env}$  is of more practical importance. That dependence is shown in Figure 3.31(b) and we can see that the emission wavelength depends almost

---

\*\*Refractive index fluids are based on mixture between perfluorocarbon and chlorofluorocarbon.

††In Chapter 2 we found that air-band edge in structure with bigger holes is more sensitive to changes  $n_{env}$ .

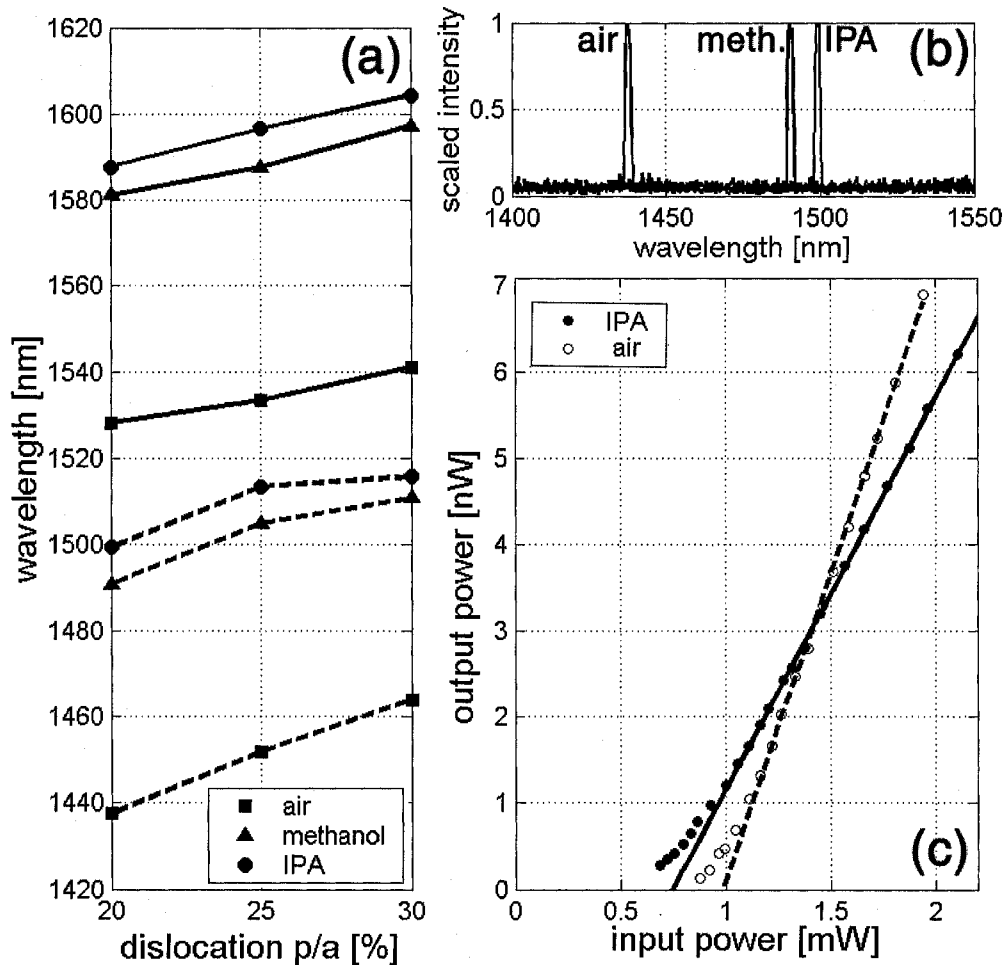


Figure 3.30: (a) Sensor response measured from 6 nanocavities with a lattice parameter of  $a = 446$  nm (dashed lines) and  $a = 460$  nm (solid lines) as a function of  $p/a$  dislocation parameter. The three curves correspond to the laser wavelength with air, methanol and IPA backfilled into the cavity. (b) Spectrum change and (c) threshold curve change of laser before and after filling with IPA.

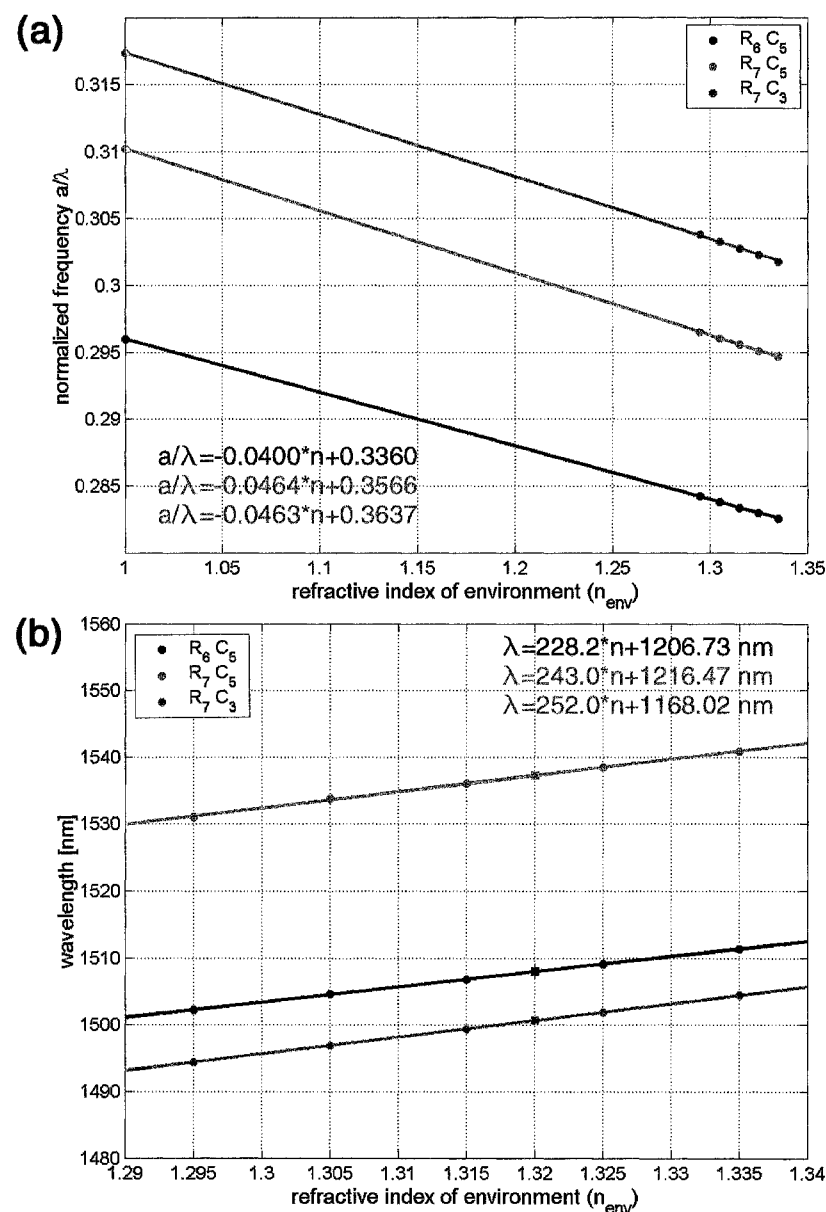


Figure 3.31: Dependence of (a)  $a/\lambda$  and (b)  $\lambda$  of HQ mode on refractive index of the environment ( $n_{env}$ ). Three different cavities, labelled  $R_6 C_5$ ,  $R_7 C_5$  and  $R_7 C_3$ , were tested.

linearly on the refractive index of environment. The sensitivity of the laser emission wavelength on the changes in  $n_{env}$  is  $\Delta\lambda = 243 \cdot \Delta n_{env}$  in case of structure  $R_7C_5$ , and this is very close to sensitivity obtained using 3-D FDTD model ( $\Delta\lambda = 266 \cdot \Delta n_{env}$ ). In our experiments we changed  $n_{env}$  in steps  $\Delta n_{env} = 0.01$ . The data points represented by square in Figure 3.31(b) correspond to  $\Delta n_{env} = 0.005$ . It can be seen that they also follow the predicted linear trend, and red shift of  $\approx 1.2$  nm is measured (structure  $R_7C_5$ ) when  $n_{env}$  is changed from 1.315 to 1.32.

### 3.4.3 Dense Integration of Laser Sensors

We have also tested structures with different defect hole sizes ( $r_{def}/a$ ) within the same photonic crystal platform in order to explore the integration multi-wavelength photonic crystal lasers with lithographically predetermined spectra. These devices are particularly interesting as compact multi-wavelength light sources, but are also useful if many reactions have to be monitored at the same time. Individual reactions can be observed in laser cavities which have predetermined spectral signatures, and optically read by observing changes in the collective spectrum of a multiwavelength laser array. In Figure 3.32 we show both the structure and accompanying spectra of three optical cavities fabricated within a common photonic crystal slab with  $a = 446$  nm and  $r = 134$  nm. The sizes of the defect holes which define the optical cavities were varied from  $r_{small} = 74$  nm,  $r_{mid} = 85$  nm and  $r_{big} = 97$  nm, and a detailed view of one of the cavities is shown in the inset. The distance between the cavities is 10 lattice periods or  $\approx 4.5\mu m$ . This distance can be even further reduced (to about  $2\mu m$ ) since the radiation of the HQ dipole mode of the cavity is predominantly along y-axis direction [Figure 3.25(b)] and therefore the cross-talk between two adjacent cavities is minimal.

To characterize our highly integrated lasers, cavities were pumped individually, and well-confined spectra were obtained from each of these cavities. The lasing wavelength of the cavities could be tuned from  $\lambda = 1420$  nm (for  $r_{big}$ ) to  $\lambda = 1550$  nm (for  $r_{small}$ ). It is important to emphasize that the emission from each nanocavity could be observed only when the pump beam was positioned exactly on top of the nanocavity. Even slight variations in the position of the pump beam resulted in turn-off of the laser.

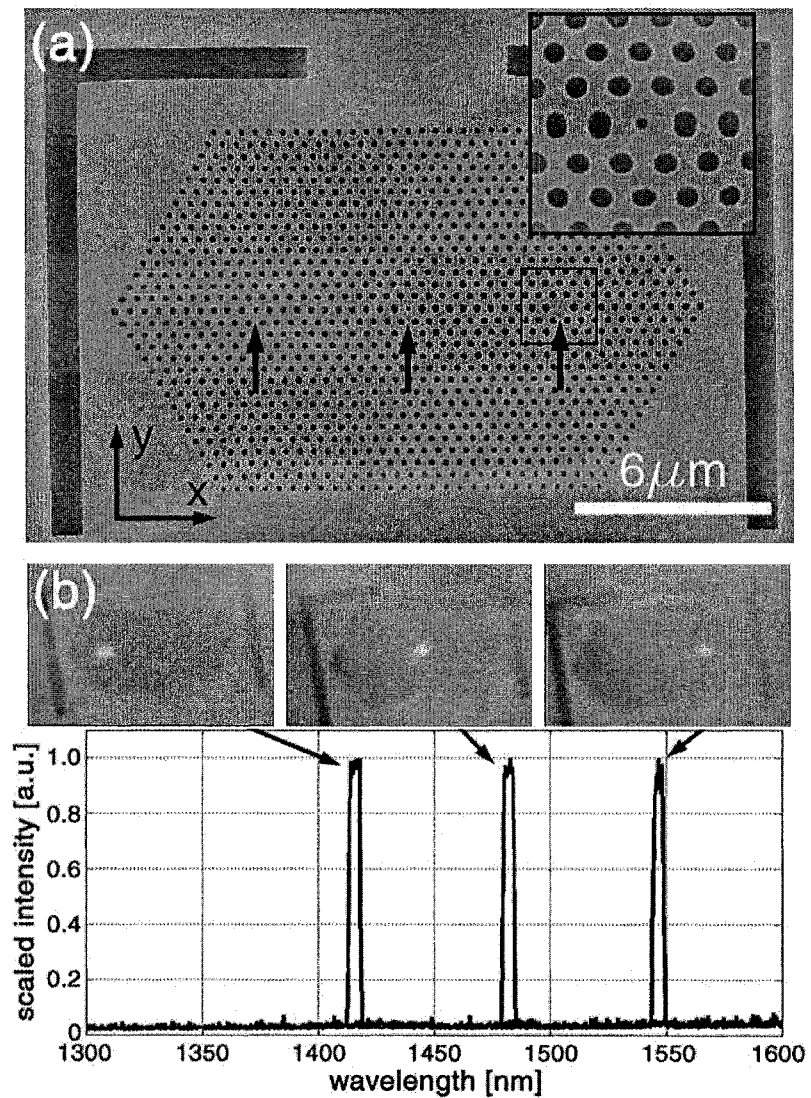


Figure 3.32: (a) Fabricated structure consists of three cavities integrated within the same photonic crystal mirror. Defect holes are indicated by arrows, and their size increases from right to left. (b) Resonances detected in each cavity. Mode experience blue-shift as the size of defect hole increases. Positions of pump-beam are shown.

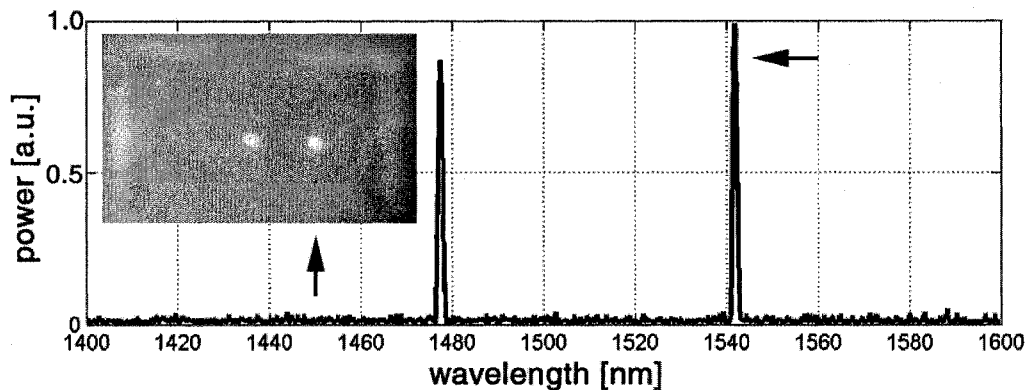


Figure 3.33: Simultaneous emission from two adjacent nano-lasers pumped simultaneously using big pump spot. Insets show near-field image of the light emitted from nanolasers.

We were also able to achieve simultaneous emission from two adjacent nano-lasers by de-focusing the pump beam so that the pump spot covers the whole structure shown in Figure 3.32(a). The results are shown in Figure 3.33. Emission from cavities with defect hole radius  $r_{small}$  and  $r_{mid}$  was detected. As it can be seen, by lithographic tuning the nanocavities and by the choice of pump position, it is possible to achieve simultaneous lasing at two different wavelengths with comparable output powers. By adjusting position of the pump beam we were also able to choose between the two lasers, and enhance the signal from one laser while suppressing the other one. Insets show the near field image of the emitted signal obtained using our NIR camera. This time, pump beam is cut-off with filter (GaAs wafer) and cannot be seen in the image, and the light detected with camera is the light emitted from the quantum wells. As expected, the strong emission exists at positions of our nanocavities, only.

### 3.5 Conclusions and Future Work

In this chapter we have presented the design, fabrication and characterization of high-Q photonic crystal nano-cavities. 3-D FDTD method is used as a design tool, and cavities were fabricated in various material systems (InGaAsP, AlGaAs, and silicon on insulator). Nanocavities made in InGaAsP active material were tested at room temperature, and were

optically pumped with pulsed laser source. Lasing is observed from the high Q dipole modes of these nanocavities. In spite of the unusual design of our structures, which have a hole etched through the position of maximum field intensity and therefore reduced overlap with gain material, we observe low threshold powers in our devices. We have attributed this to the small mode volume and the high Q factors inherent to our device design. Polarization and lithographic tuning properties of two dipole modes supported in the cavity are in excellent agreement with theoretical FDTD predictions. The mode profile taken by our IR camera shows that the lasing resonance is well localized to the center of our cavity.

In nanolaser that we have developed high-intensity optical field is localized in the air. This is fundamentally different from the majority of semiconductor lasers, since they confine the light in the high-index material. Therefore, our lasers are ideally suited for investigation of interaction between light and matter placed in the high optical fields. For example, our high Q laser cavities with small mode volumes provide us with opportunities for integrated optical spectroscopy systems. We have demonstrated this concept and showed that changes in refractive index of the ambient surrounding the laser cavities can be measured by observing the shifts in emission wavelengths of the lasers. Small changes in refractive index can be detected within samples of femtoliter volumes, and such devices can be integrated into large arrays to permit the analysis of many reagents at the same time. Since InGaAsP can serve both as a laser gain material as well as a material for light detection, it is possible to develop compact and integrated spectroscopy systems for detection of chemical and biological molecules. For example photonic crystal nanocavities with modest Q-factors can be included to detect changes in the output signal of adjacent laser diodes. We have integrated our nanolasers with microfluidic systems defined in soft materials (PDMS) in order to enable delivery of small quantities of reagents. This will lead towards realization of highly integrated optoelectronic/microfluidic *laboratory on the chip* systems. Possible applications of the system that we have developed are protein detection by monitoring wavelength shifts due to refractive index changes, detection of sugar level in blood using absorption spectroscopy, on-chip Raman spectroscopy for chemical analysis, etc.

Spectroscopy for chemical or biological analysis is typically performed in the UV/Visible and the mid-IR wavelength ranges. This is a result of the availability of sources, detectors, and fluorescent dyes, but is also determined by the energy ranges at which bonds and molecular vibrations of molecules are excited. The  $1.55\mu m$  range, although convenient from the

availability of efficient laser material, is not usually considered to be an interesting range for direct absorption measurements. Therefore, we are working on development of photonic crystal lasers that emit at visible wavelengths (red), using AlGaInP material. An additional benefit from reducing lasing wavelength is the improvement of the Raman excitation efficiency of molecules, which is typically inversely proportional to the pump wavelength.

## Chapter 4

# Planar Photonic Crystal Waveguides

### 4.1 Introduction

The optical waveguide is one of the most important components of integrated optical systems, and it has the role that a wire has in an electronic system. In order to achieve compact, low-loss and fast optical systems, waveguides should be:

#### 1. Low-loss

To efficiently transmit information between different parts of the system, as well as to minimize cross-talk between different channels (waveguides) and to improve the security of the system.

#### 2. Dispersion-less

High-speed applications require broad-band waveguides with little dispersion.

#### 3. Single-mode

#### 4. Compact

For example, the capability to efficiently negotiate sharp bends is an important feature of optical waveguides since large bends consume a lot of chip “real-estate”.

Realization of optical systems in high refractive index contrast materials (e.g., silicon on insulator) offers an opportunity to satisfy these requirements. Two most researched types of optical waveguides designed in these systems are *silicon wire* and *photonic crystal waveguide*. Silicon wire is a conventional device, whose operation is based on the total internal

reflection between the Si core and air/ $SiO_2$  cladding. Recently there has been significant progress in both theoretical and experimental treatment of these structures, and efficient guiding and bend-turning in silicon wires have been reported when some sort of resonator is inserted in the waveguide bend.<sup>67,68</sup> Photonic crystal waveguide, on the other hand, is a novel type of waveguide whose operation is based on distributed Bragg reflection due to the presence of the periodic dielectric lattice.<sup>69</sup> The most interesting property of the PC waveguide is the possibility of making sharp bends, with acceptable transmission efficiency around the bend.<sup>70–75</sup> This is due to the fact that a photonic crystal acts like an excellent mirror and therefore, light in the bend cannot leak outside the waveguide. In addition, planar photonic crystals offer a great promise for the realization of waveguides with *engineered* dispersion properties,<sup>76</sup> that can be used to realize compact delay lines,<sup>77</sup> interferometers, etc. Also, by combining interesting dispersion properties of PPC waveguides<sup>18,78–80</sup> with dispersion properties of (nonlinear) materials, it becomes possible to enhance nonlinear phenomena<sup>81–83</sup> of the materials as well as to propagate pulses confined both in space and time.<sup>84</sup> The latter is very interesting for realization of ultra-fast systems.

The idea of using line defects in photonic crystals to guide light was proposed by Meade et al.,<sup>85</sup> while Mekis et al. have developed the theoretical foundation of understanding 90° bends in the two-dimensional photonic crystals.<sup>69</sup> The disadvantage of using photonic lattices constructed from dielectric rods surrounding an air waveguide is that there is no mechanism for low-loss vertical confinement of the light within the waveguide at optical frequencies. A more favorable geometry is the planar photonic crystal within which a line defect of missing holes can be defined. Here, we present the theoretical analysis, fabrication and experimental characterization of waveguides based on planar photonic crystals that incorporate two-dimensional photonic crystal geometries for lateral confinement of light, and total internal reflection for vertical confinement.

## 4.2 Design of Planar Photonic Crystal Waveguides

### 4.2.1 Single Line Defect Waveguide

When we introduce a line defect into the photonic crystal by removing an entire line of holes from the two-dimensional crystal lattice (Figure 4.1), we form the simplest photonic crystal

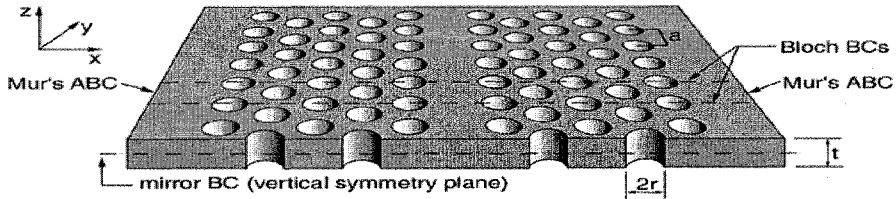


Figure 4.1: Schematic of the single line defect waveguide. Unit cell and boundary conditions used in the FDTD calculation are indicated.

waveguide. By forming such a defect, we are adding “donor impurities” to the photonic crystal, and as a result modes from the air band are pulled down into the bandgap and form defect states. Energy can now propagate only along this line defect, and this results in the waveguiding of light. Propagation in the lateral direction is suppressed since the defect mode is within the bandgap of the photonic crystal, and propagation in the vertical direction is prevented since the mode is below the light line. In our case waveguides are extending along  $y$ -axis in 3-D space. Due to the periodicity of the lattice, the waveguides analyzed here have discrete translational symmetry with periodicity  $a$ .

Single line defect waveguides were analyzed using the 3-D FDTD algorithm. Discretization was again 20 points per interhole spacing ( $a = 20$ ). Since a waveguide has reflection symmetry in vertical ( $\sigma_{xy}$ ) and lateral ( $\sigma_{yz}$ ) direction (Figure 4.2), we could reduce computation time by analyzing only one quarter of the structure by applying mirror boundary conditions in the middle of the slab and in the center of the waveguide. Bloch boundary conditions were applied in the  $y$ -direction, at the boundaries of the waveguide unit cell. For analysis of the square lattices, Mur’s ABCs were applied in the vertical direction, at a distance  $3 \cdot a = 60$  computational units away from the surface of the waveguide, and in the lateral direction, after 5 layers of photonic crystal. The half-thickness of the slab was  $t = 5$  points. Therefore, the computational domain consisted of  $110 \cdot 20 \cdot 65$  cubic cells. The advantage of using absorbing boundary conditions over the supercell approach is that we can map out not only the guided modes of the structure, but also the leaky modes - modes that satisfy vertical resonance in the waveguide but lie above the light line. In the case of triangular PC waveguides, Mur’s ABCs were also used in the vertical direction. In this case, we analyzed 8 layers of photonic crystal, so that total computational box consisted of  $141 \cdot 20 \cdot 65$  cubic cells.

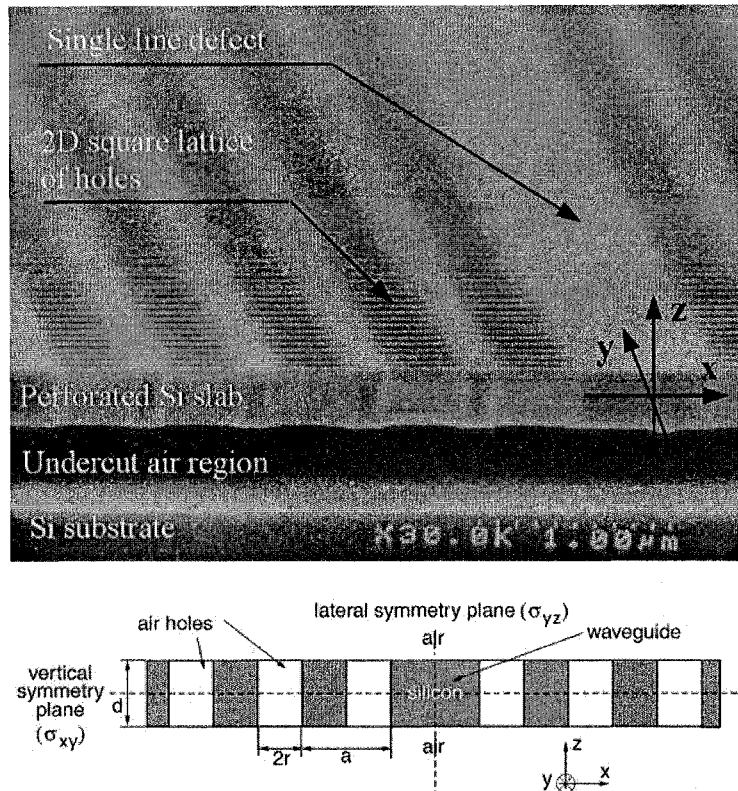


Figure 4.2: (a) Cross section of the fabricated square lattice waveguide suspended in the air and (b) schematic of the waveguide viewed end-on. Reflection symmetry planes are  $\sigma_{xy}$  in the middle of the slab (vertical symmetry plane), and  $\sigma_{yz}$  in the center of the waveguide (lateral symmetry plane).

In Figures 4.3 and 4.4 we present dispersion diagrams for modes supported in the single line defect photonic crystal waveguide of square and triangular symmetry. The propagation constant  $\beta$ , also labeled as  $k_y$ , is on the x-axis of the diagram, and normalized frequency in units  $a/\lambda$  is on the y-axis. Dispersion diagram is calculated for 25 different values of the propagation constant  $k_y$  ( $\beta$ ) in the interval  $(0, \pi/a)$ . The direction of propagation of light in the case of the waveguide made in a square lattice PC is along the  $\Gamma X$  direction in the reciprocal space. Due to the periodicity of the waveguide in the y direction,  $k_y$  can only take values in the interval  $(0, \pi/a)$ , that is any value between  $\Gamma$  and  $X$  points. The procedure for finding dispersion diagram of guided modes was discussed in Chapter 2 and here it is again briefly summarized. We fix one value of  $k_y$  by applying Bloch boundary

conditions to the boundaries of the waveguide unit cell. Then, we evolve in time the initial field in the waveguide and store the field evolution in several low symmetry points. We find the spectrum of these time evolutions by applying a fast Fourier transform. Peaks in the spectrum correspond to the characteristic modes of the structure. However, not all of the modes that we find in this way are necessarily guided modes of the waveguide, and we can detect modes of PC slab, as well. Since guided modes can exist only in the region in  $(k_y, a/\lambda)$  space where there are no photonic crystal modes, it is necessary to project all the bands of PC lattice onto the  $\Gamma X$  direction. In Figures 4.3 and 4.4 the dark gray regions are regions where modes of photonic crystal slab exist. The light line is indicated with the solid line going from  $(0, 0)$  to  $(\pi/a, 0.5)$ . All modes above the light line, in the light gray region, will leak energy into the air, and modes that exist in the dark gray region will couple to the states of photonic crystal and leak energy into it. The regions where 3-D localization of light in the waveguide can occur are shown in white in both Figures 4.3 and 4.4.

By analyzing Figure 4.3, it becomes clear that there are two mechanisms of light confinement in the lateral direction. First, guiding can occur if the mode is below all photonic crystal modes (modes  $e_1$ ,  $o_1$  and  $o_2$  in Figure 4.3). These modes do not “see” the Si slab perforated with 2-D PC lattice as the PBG material, but rather as material with an effective refractive index ( $n_{eff}$ ) lower than the refractive index of Si core ( $n_{Si} = 3.5$ ). The mechanism of guiding for these modes is similar to the standard index-contrast waveguide: total internal reflection. Since they do not see periodicity of the PC there is no upper limit for propagation constant  $k_y$ , and therefore, at the zone boundary ( $k_y = \pi/a$ ), they appear to be folded back into the first Brillouin zone of the waveguide. However, careful FDTD analysis of this waveguide mode shows the existence of the small bandgap at the zone boundary. This is an indication that the modes do “feel” the periodicity of the lattice as discussed in the later section. When modes cross the regions where the modes of the PC slab exist, they interact with them and leak energy into the PC. This is due to the fact that the modes of the PC slab extend outside the first BZ.

Another type of guiding occurs for the modes that are located in the bandgap (modes  $e_2 - e_4$  in Figure 4.3). These modes are truly photonic crystal effect guided modes, and would not exist if there was no periodic crystal lattice. They are pulled down, into the bandgap, from the air band and therefore we expect them to resemble the properties of that band. Since the bottoms of the air bands are flat (see band diagrams of the even

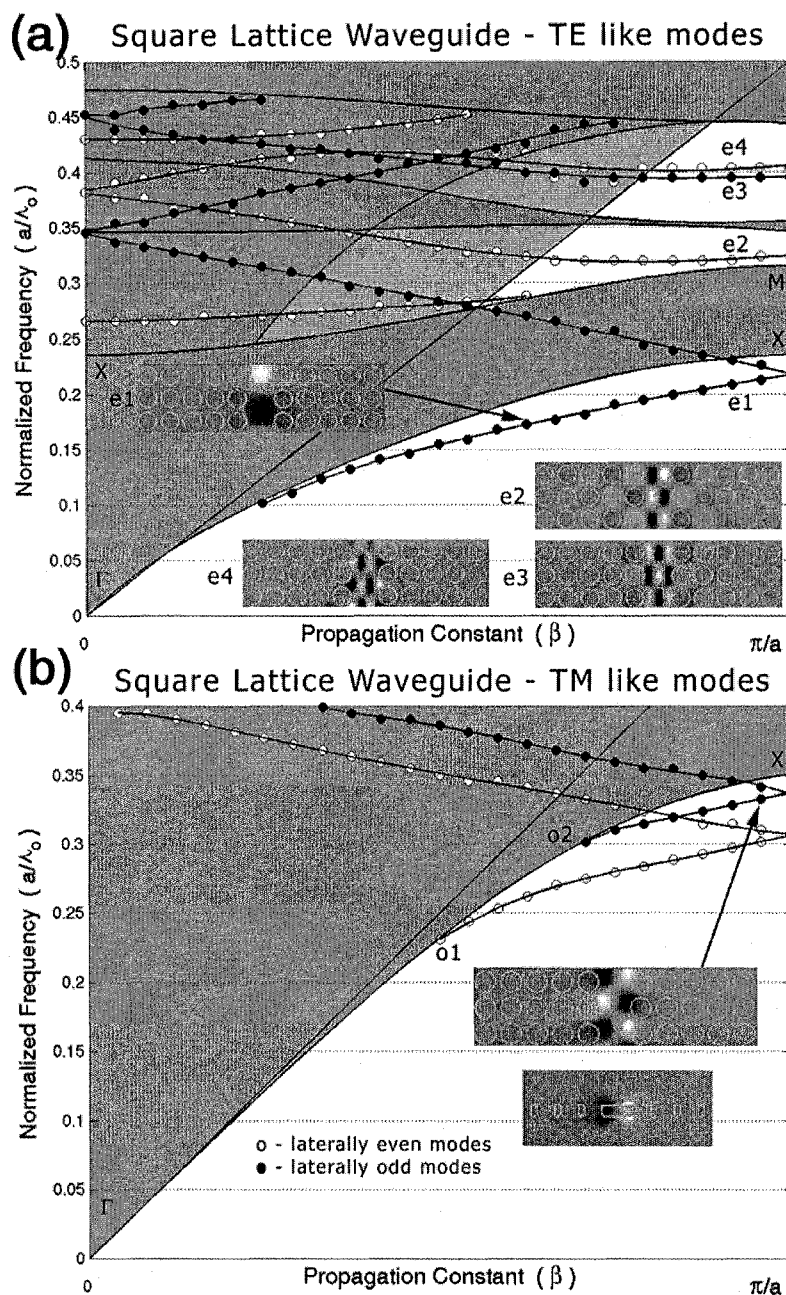


Figure 4.3: Dispersion diagram for (a) vertically even (TE-like) and (b) vertically odd (TM-like) guided modes in the square lattice waveguide. Symmetry of the modes with respect to the lateral symmetry plane ( $\sigma_{yz}$ ) is indicated. Modes are labeled  $e_1 - e_4$  for vertically even case, and  $o_1 - o_2$  for vertically odd case. Characteristic high symmetry points are also shown (dielectric band only). Insets show field patterns of (a)  $B_z$  and (b)  $E_z$  components in the middle of the slab (z-slice) for different guided modes. In the case of TM-like guided modes ( $o_1$  and  $o_2$ ), distribution of  $E_z$  component along the cross section of the waveguide is shown, as well.

modes in  $XM$  direction, Chapter 2), we expect these PC effect guided modes to have flat dispersion. The flat dispersion will result in the small group velocity and inefficient transport of energy, the property that needs to be investigated in more detail.

Field profiles of the  $B_z$  (TE-like modes) and  $E_z$  (TM-like modes) components of the field in the middle of the slab ( $\sigma_{xy}$  plane) are shown as insets in Figure 4.3. Figure 4.5 shows field distribution of the same components along the cross section of the waveguide ( $\sigma_{xz}$  plane) for several different modes. As we can see, all the modes are fundamental in the vertical direction, and have different number of nodes in the lateral direction. In this work we are interested in the PBG effect guided modes: mode  $e_2$  in the first order bandgap, and modes  $e_3$  and  $e_4$  in the second order bandgap. Field profiles for these modes are taken for  $k_y = \frac{22}{24} \cdot \frac{\pi}{a}$ . For this value of  $k_y$ , mode  $e_2$  approaches, in  $(k_y, a/\lambda)$  space, modes of PC slab (gray region), couples to them and leaks energy into the photonic crystal. This can be observed in the inset  $e_2$  in Figure 4.3(a) as the  $B_z$  field pattern penetrating the photonic crystal. If we move away from the zone boundary, closer to the light line, the mode will start radiating more energy into the air, and again will experience a loss. If we want to excite  $e_2$  mode with an external light source, light will also couple to the leaky  $e_1$  mode, since it exists in the same frequency range, and coupling efficiency will decrease. In addition, the dispersion diagram for the TM-like modes [Figure 4.3(b)] tells us that the mode  $e_2$  exists in the same frequency range as the  $e_2$ , and therefore the single mode operation of the waveguide is not possible. This problem could be solved by selecting the polarization of the input light, so that we preferentially couple to the  $e_2$  mode. Modes  $e_3$  and  $e_4$  in the second order gap have different spatial profiles but are very close in frequency. This can be understood by analyzing the properties of the PC slab modes. We observe that, in the case of square lattice, the second air band along  $XM$  direction is double degenerate [Figure 2.3(a)], and therefore when pulled down in the bandgap will produce two closely spaced modes  $e_3$  and  $e_4$ .

In Figure 4.3(b) we show the dispersion relation for guided modes with vertically odd symmetry (TM-like). Although there is no bandgap for TM-like modes [Figure 2.3(a)], light can be localized to the waveguide due to the refractive index contrast, as described above.

In Figure 4.4 we show dispersion relations for the guided modes in the waveguide based on the triangular PC lattice. In the case of a triangular lattice waveguide, a single line defect is formed in the  $\Gamma J$  direction. Again,  $k_y$  can assume values in the interval  $(0, \pi/a)$

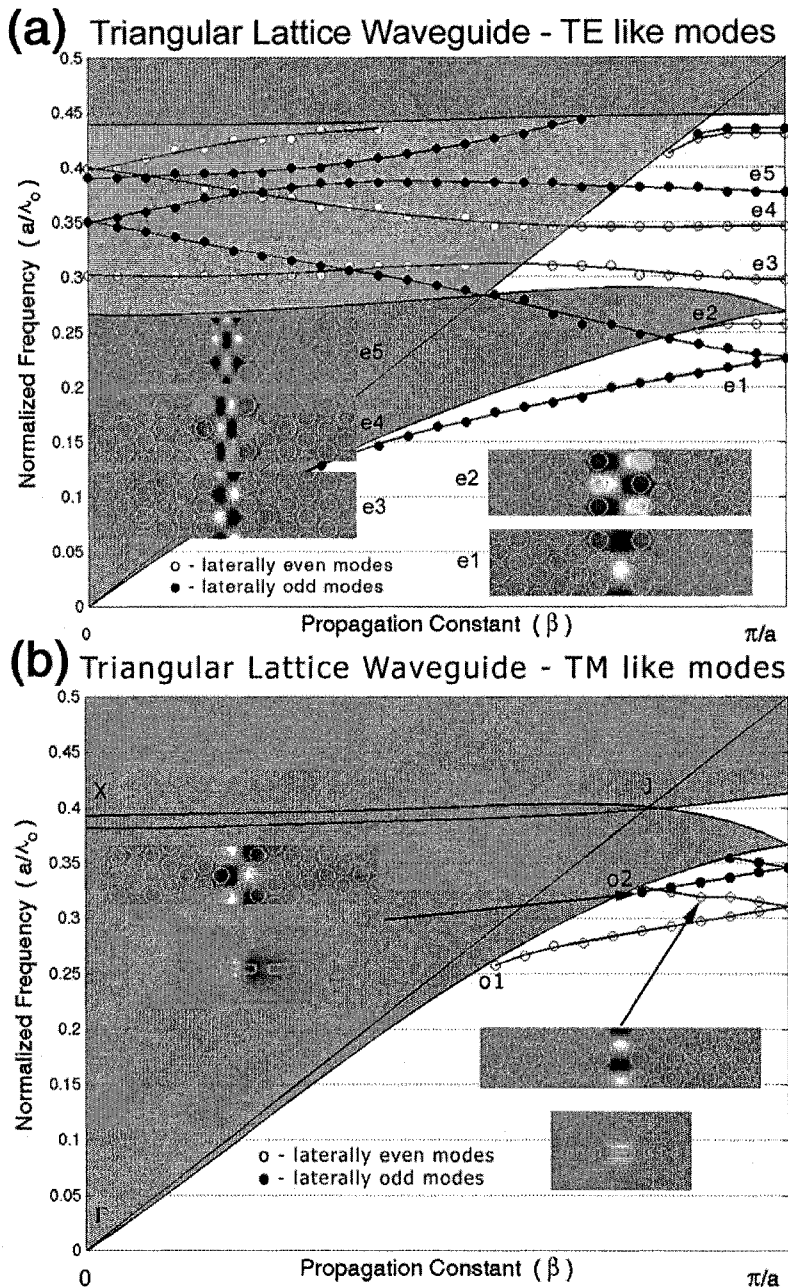


Figure 4.4: Dispersion diagram for (a) vertically even (TE-like) and (b) vertically odd (TM-like) guided modes in the waveguide based on the triangular PC lattice. Insets show field patterns of (a)  $B_z$  and (b)  $E_z$  components in the middle of the slab (z-slice). In the case of TM-like modes ( $o_1, o_2$ ), distribution of  $E_z$  component along the cross section of the waveguide ( $\sigma_{xz}$  plane) is shown. Note that the cross sections for  $o_1$  and  $o_2$  modes are taken at different positions along the waveguide. Field profile for  $o_2$  is taken near the cut-off and therefore the field penetrates the photonic crystal, as can be seen in the inset.

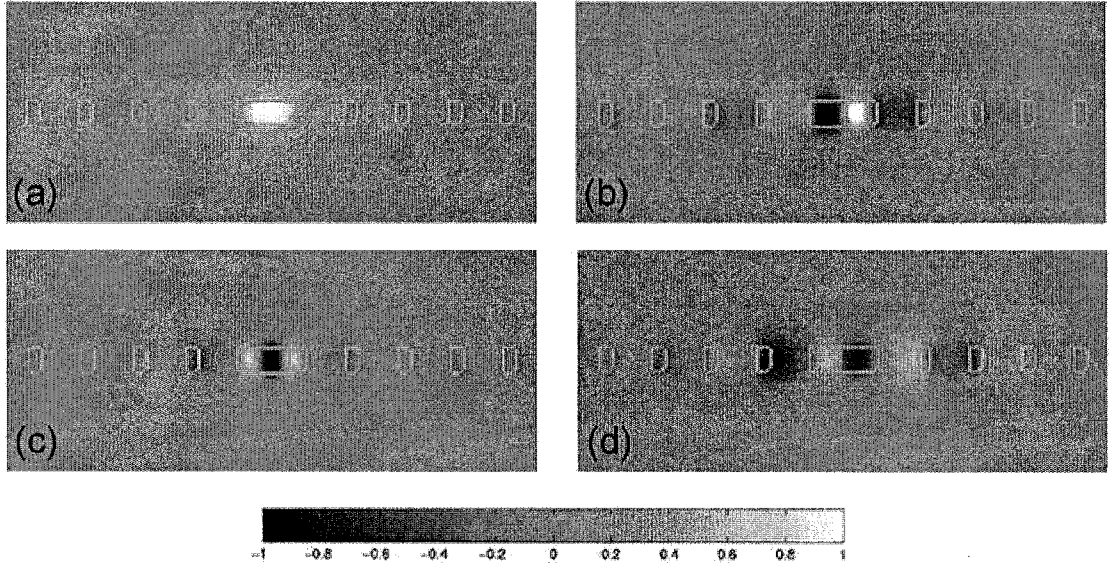


Figure 4.5: Distribution of the  $B_z$  component of the field along the cross section of the **square** lattice based waveguide ( $\sigma_{xz}$  plane) for different guided modes. Labeling is (mode,  $k_y \cdot \frac{a}{\pi}$ ,  $a/\lambda$ ). (a)  $(e_1, 15/24, 0.173)$ , (b)  $(e_2, 22/24, 0.320)$ , (c)  $(e_3, 22/24, 0.395)$  and (d)  $(e_4, 22/24, 0.404)$ . It can be seen that all the modes are fundamental in the vertical direction. The core of the waveguide appears as the rectangle in the center of the figure.

what represents  $3/4$  of the  $\Gamma J$  direction. In Figure 4.4 we have projected all the bands from Figure 2.3(b) to the  $(0, 3/4 \cdot \Gamma J)$  range (gray regions). We see that the triangular lattice based waveguide can support several TE-like modes. Two of them,  $e_1$  and  $e_2$ , are “index” guided and lie below the modes of PC lattice. Other modes are PBG effect guided, and are located in the bandgap. The structure also supports two index guided TM-like modes [Figure 4.4(b)]. Since the bandgap is closed in the case of TM-like modes there are no PBG effect guided TM-like modes. In Figure 4.6 we show field profiles of the  $B_z$  components along the cross section of the waveguide ( $\sigma_{xz}$  plane) for several different modes.

Before analyzing the different types of waveguides in the next three sections, it is important to notice that all PBG guided modes shown in Figure 4.4 (below the light line, and in the frequency bandgap) have an almost flat dispersion relation. Therefore, these modes will have small group velocities and will be able to guide the light only in a very narrow frequency range. This is very different from an ideal case, where we want to have efficient transport of energy in a wide frequency range. Also, coupling between PC waveg-

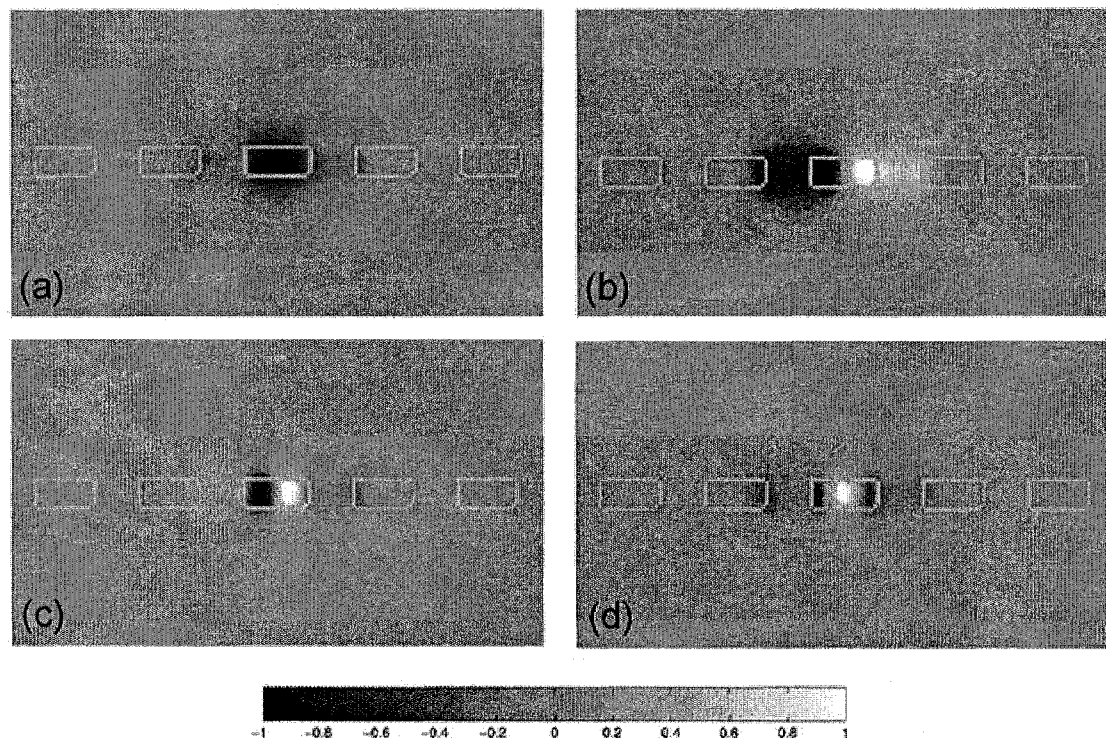


Figure 4.6: Distribution of the  $B_z$  component of the field along the cross section of the **triangular** lattice based waveguide ( $\sigma_{xz}$  plane) for different guided modes. (a)  $(e_1, 17/24, 0.191)$ , (b)  $(e_2, 24/24, 0.260)$ , (c)  $(e_4, 21/24, 0.346)$  and (d)  $(e_5, 21/24, 0.382)$ . Again, all the modes are fundamental in the vertical direction. The core of the waveguide appears as the rectangle in the center of the figure.

uides and conventional waveguides is expected to be poor due to very different dispersion characteristics of the two waveguides, and alternative methods of adiabatic coupling need to be used.<sup>86–88</sup> However, small group velocity can be interesting for the enhancement of nonlinear phenomena, realization of delay lines, compact interferometers, etc.

#### 4.2.2 Effect of the Hole Size on the Waveguide Properties

In the previous section we learned that single line defect waveguides, based on triangular or square lattice photonic crystals, are multimode structures and can support both TE-like and TM-like polarized modes. However, for many applications it is advantageous to work with single-mode structures. In this section we investigate the influence of photonic crystal hole size on the dispersion properties of a PPC waveguide.

The waveguides were analyzed using 3-D FDTD code. We have analyzed Si slabs (refractive index assumed to be  $n_{Si} = 3.5$ ) of thickness  $t = 0.55a$ , surrounded by air on both sides, and perforated with a 2-D triangular lattice of holes of radius  $r = 0.3a$ . The discretization of the space used in 3-D FDTD code was again  $a = 20$  computational points. In the analysis that follows, we have analyzed only one half of the structure in the vertical direction, with a mirror boundary condition applied at the middle of the slab. In the vertical direction we have applied Mur's absorbing boundary conditions (BC) at a distance of  $4a$  points (more than one wavelength in air) from the surface of the slab. In the  $y$  direction (along the waveguide) we have applied Bloch BCs and in that way we could control the propagation constant of the mode ( $\beta$ ). In the  $x$  direction we have applied Mur's ABC after eight layers of PC at both sides of the waveguide. In this section we will be interested mostly in TE-like modes, since the bandgap exists only for these modes.

In Figure 4.7 we show the band diagram for a triangular lattice photonic crystal with  $r/a = 0.3$ . The bandgap for the modes of bulk photonic crystal is open around  $\frac{a}{\lambda_0} = \frac{\omega a}{2\pi c} \approx 0.28$  normalized frequency. In the previous section we used the value  $r/a = 0.4$ . The smaller value of  $r$  results in a narrower bandgap, but in turn improves localization of light within a slab, which is especially important for efficient turning of corners. In addition, as it will be shown later in this section, a PPC waveguide with smaller holes supports fewer guided modes.

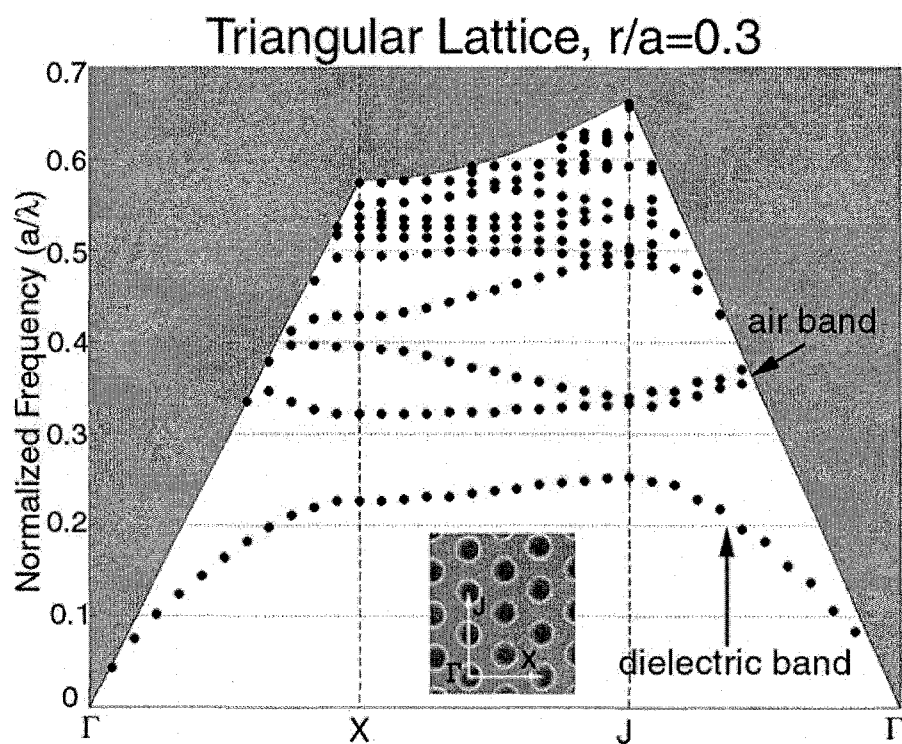


Figure 4.7: The band diagram for the TE-like (vertically even) modes of the Si slab perforated with triangular lattice of air holes. Parameters used in analysis are  $r = 0.3a$  (hole radius),  $t = 0.55a$  (slab thickness),  $n_{Si} = 3.5$  (refractive index of Si).

By omitting one row of holes we form a single line defect waveguide (*type 0*), as analyzed in the previous section. This type of waveguide, where we increase the amount of the high dielectric material comparing to the unperturbed PPC, is called a *donor-type* waveguide. Figure 4.8(a) shows the dispersion diagram for guided modes of a single line defect waveguide. The crossing of *mode 1* and *mode 2* in Figure 4.8 is due to the different symmetry properties of these two modes in the lateral direction (*mode 1* is odd and *mode 2* even with respect to the mirror plane in the center of the waveguide). The modes above the light line will leak energy into the air (leaky modes). In this work we are interested only in the truly photonic bandgap (PBG) guided modes of the waveguide. Therefore, from now on (Figures 4.10, 4.13 and 4.14) we will show only modes that are located in the frequency bandgap. In addition, *modes 3* and *4* are not of any practical interest since they are located very close to the band edge and therefore will be pushed back into the air-band when we change the waveguide geometry. Because of that, they will not be included in the analysis that follows. In this paper we will be interested in the position of *modes 1* and *2*, and any other additional modes that appear as we make some changes to the single line defect waveguide.

For comparison, in Figure 4.8(b) we show the dispersion diagram for guided modes in a single line defect waveguide with  $r/a = 0.4$ , where all other parameters are held the same as in Figure 4.8(a). It is clear that the structure with larger holes has a much more complicated dispersion diagram. The most important difference between the two structures is that in the case of bigger holes there exist leaky modes at all bandgap frequencies. Therefore, by coupling light from an external light source into the waveguide, leaky modes are excited as well, and the coupling efficiency decreases. However, in the structure with  $r/a = 0.3$  there are no leaky modes in the frequency range where *mode 1* becomes guided [Figure 4.8(a)]. Therefore, it can be used for guiding of light and efficient coupling from an external light source. However, *mode 1* is not very well confined to the waveguide, and decays slowly into the PPC, since it is located close to the dielectric-band edge. Thus, it may suffer from the finite size effects of PPC and be more sensitive to the fabrication disorder. In order to achieve the efficient guiding of light, it is desirable to push *mode 1* to higher frequencies, closer to the midgap, and use it as our guided mode of preference. This can be achieved by reducing the amount of high dielectric material that forms the waveguide.

In the next two sections we will investigate different waveguide designs, based on a tri-

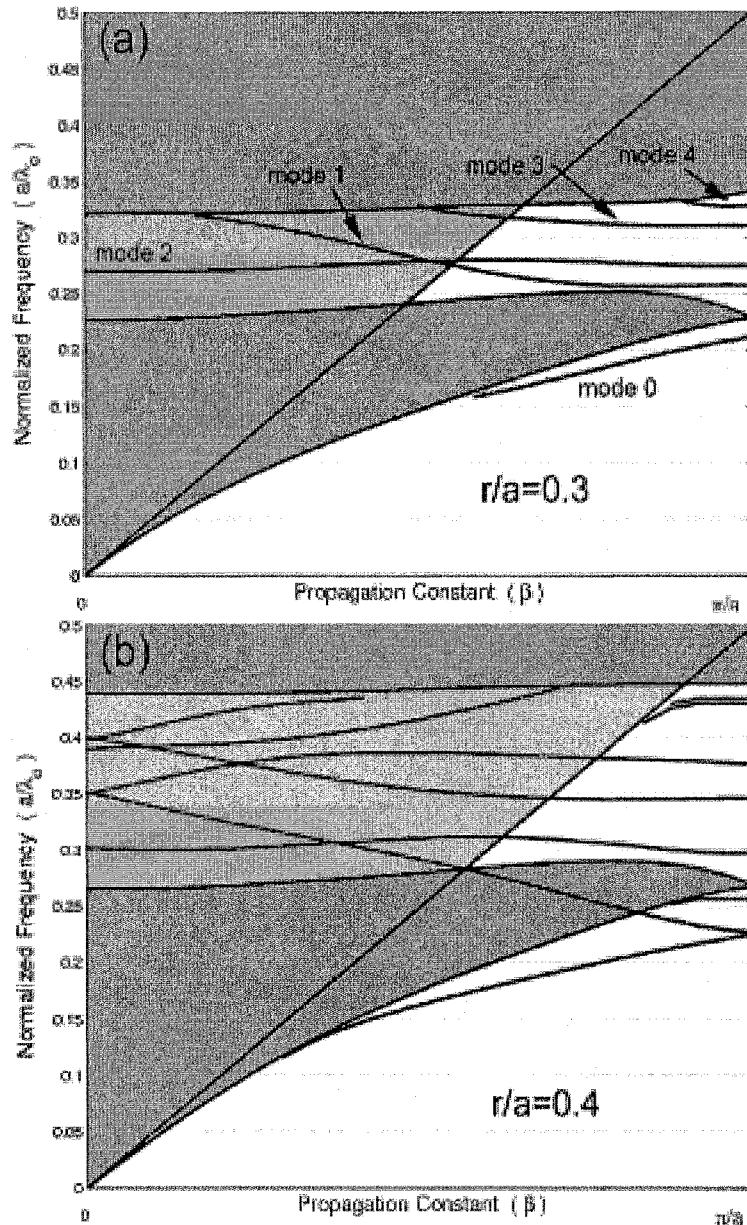


Figure 4.8:  $\omega - \beta$  relation for the guided modes in the single line defect waveguide *type 0* for (a)  $r/a = 0.3$  and (b)  $r/a = 0.4$ . The straight solid line represents the light line. The modes above the light line, in the light gray region, will leak energy into the air (leaky modes). The dark gray areas are the regions where extended states of the PPC slab exist. Guiding can occur in the white regions.

angular PPC lattice, and analyze their  $\omega - \beta$  dispersion properties. We will show several ways of controlling the frequencies of guided modes, a feature that can also lead to the single-mode regime of the operation of the waveguide. The ability to control the position of the guided modes within a frequency bandgap of surrounding PPC is necessary in order to achieve three important goals:

**1. Low-loss waveguiding**

Reduced lateral and vertical losses

**2. Good coupling efficiency**

No leaky modes at the frequency of interest

**3. Coupling between different PPC devices**

Mode matching between waveguide and cavity is necessary in order to realize efficient channel-drop filters, for example. The eigen frequency of the cavity mode is fixed by a choice of a high quality factor of the cavity, and good coupling can be achieved by tuning the waveguide mode.

#### 4.2.3 Waveguides Based on the Rearrangement of the PPC Lattice

The straightforward way of controlling frequencies of the guided modes is the reduction of the waveguide width. By reducing the amount of the high-refractive index material, we push the modes to higher frequencies due to reduced overlap between the mode and high-refractive index material. This can be achieved by moving the two semi-infinite PPC mirrors that surrounds the single line defect, towards one another [Figure 4.9(a), (b)], along  $\Gamma X$  direction.<sup>89–92</sup> We will call this type of waveguide *type 1*. The dispersion diagram of the guided modes in waveguides of different widths is shown in Figure 4.10(a). We can observe that modes 1 and 2 are shifted towards higher frequencies as the width of the waveguide decreases. For parameter  $M=5$  *mode 1* is shifted closer to the midgap frequency and therefore losses related to the leaks into the PPC are reduced. That means that *mode 1* can now be used to guide the light in the waveguide. However, a big disadvantage of *type 1* waveguide is the broken symmetry of the triangular lattice - it is impossible to create sharp bends with the waveguide sections of the same width [Figure 4.9(b)], unless we create unwanted line defects close to the bend and in that way reduce the bending efficiency. Therefore, the *type 1* waveguide is not a good candidate for controlling the position of the guided modes.

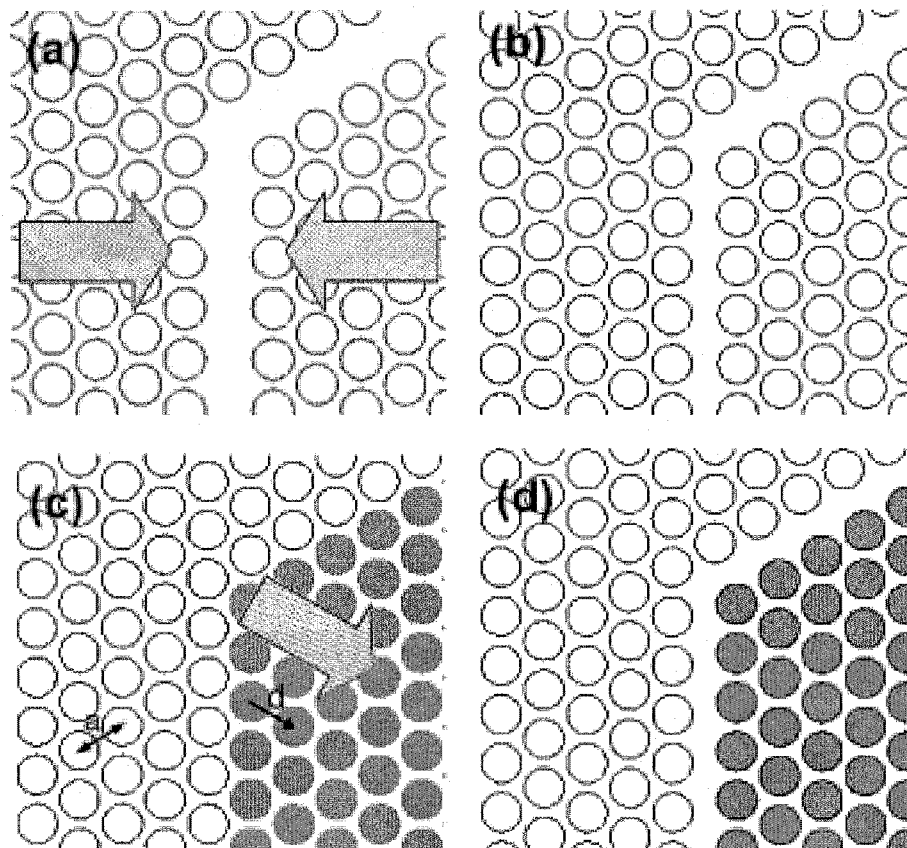


Figure 4.9: Different type of waveguides. By moving the PPC mirrors that surround the single line defect waveguide (a) along the direction indicated by arrows ( $\Gamma X$  direction) we can form a *type 1* waveguide (b). (c) Unperturbed PPC lattice. If we offset the black holes along the  $\Gamma J$  direction (as indicated by arrow) for the amount  $d$ , we can form a (d) new type of waveguide (*type 2*). By controlling the parameter  $d$ , we can control the positions of the guided modes of the structure.

Another, more promising, method of controlling the positions of the guided modes is shown in Figure 4.9(d). This novel type of waveguide<sup>89</sup> will be called *type 2*. The waveguide is formed from the PPC lattice by moving two regions of PPC apart, along the  $\Gamma$ J (nearest neighbor) direction, by the offset  $d = l \cdot a$  [Figure 4.9(c), (d)], where  $l$  is a real number. For  $l = 1$  we can form the single line defect waveguide, and for  $0 < l < 1$  waveguide narrower than a single line defect. Now, it is possible to create sharp  $60^\circ$  bends within the waveguide without introducing unwanted line defects. Dispersion characteristics for guided modes in this structure, as a function of the parameter  $d$ , are shown in Figure 4.10(b).

For  $d = 0.5a$ , *mode 1* is pushed to around the midgap frequency, and *mode 2* is pushed out of the bandgap, all the way back into the air band. Therefore, we have achieved our goals of designing a waveguide with reduced lateral losses (due to the finite-size effects and fabrication disorder) and increased coupling efficiency, since there are no leaky modes at the frequency of interest. However, because of the dislocation of the PPC regions, creation of  $120^\circ$  bends as well as an easy integration of *type 2* waveguide with PC cavities, is not straightforward any more.

In Figure 4.11 we show field patterns of *mode 1* in the case of *type 1* and *type 2* waveguides, for parameters  $M = 5$  and  $d = 0.5a$ , respectively. In both cases, E and B field have an anti-node at the middle of the waveguide, and therefore it is possible to efficiently couple TE polarized light (with  $B_z$  and  $E_x$  components) from an external light source into the waveguide.

There is one more interesting feature that can be observed in Figure 4.10(b). An extra mode, pulled from the dielectric band up into the bandgap, appears as we reduce the value of the parameter  $d$  [labeled *accept. mode* in the Figure 4.10(b)]. This mode has the same symmetry as *mode 1*, and therefore the two modes interact strongly (anti-crossing). This mode can also be observed in the case of *type 1* waveguide [Figure 4.10(a)]. Now, what has to be explained is why does the *acceptor-type* guided mode appear in the *donor-type* waveguide, since we would expect that by adding dielectric material, guided modes are formed by reducing the frequency of the air-band modes.

In order to explain this, we will focus our attention to Figure 4.12. Figure 4.12(a) and (b) show electric field distribution (amplitude) in the unperturbed PPC at the X point for

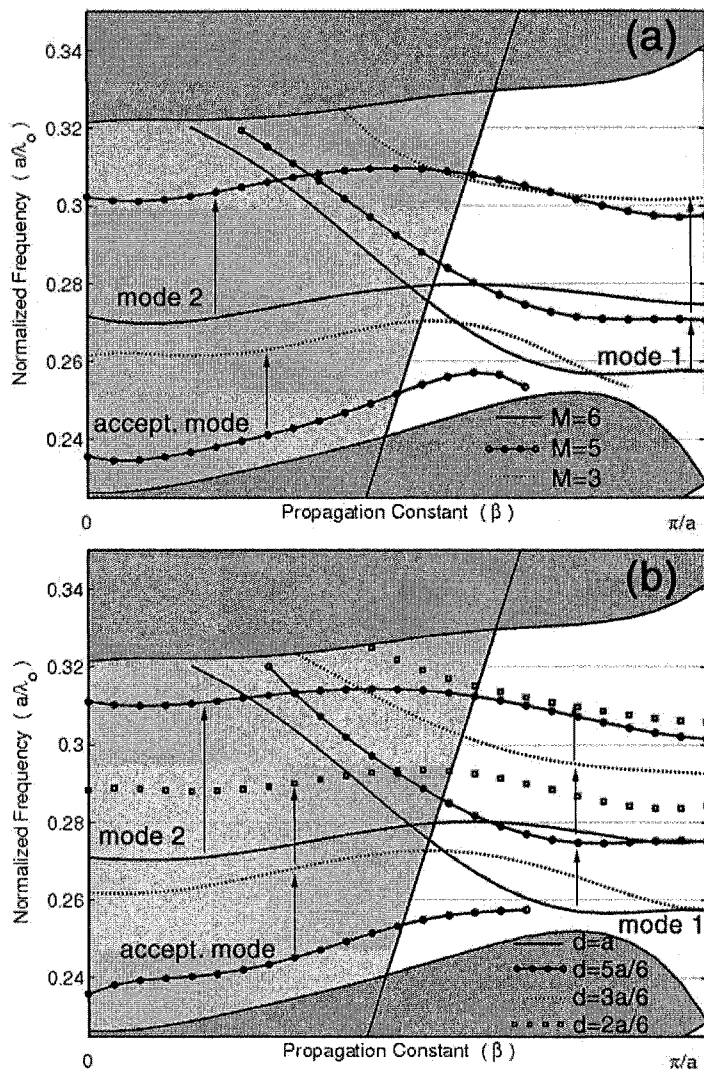


Figure 4.10: Dispersion relations for the guided modes of the *type 1* and *type 2* waveguides for different values of controlling parameters ( $M$  and  $d$  respectively). Arrows indicate the positions of the modes as we change the controlling parameters. (a) *Type 1* waveguide. The width of the waveguide (center-to-center distance between two holes adjacent to the waveguide) is defined as  $a \cdot \sqrt{3}/2 \cdot (1 + M/6)$ .  $M=6$  yields a single line defect waveguide. (b) *Type 2* waveguide. Position of the modes as a function of the parameter  $d$  - offset along the  $\Gamma J$  direction.

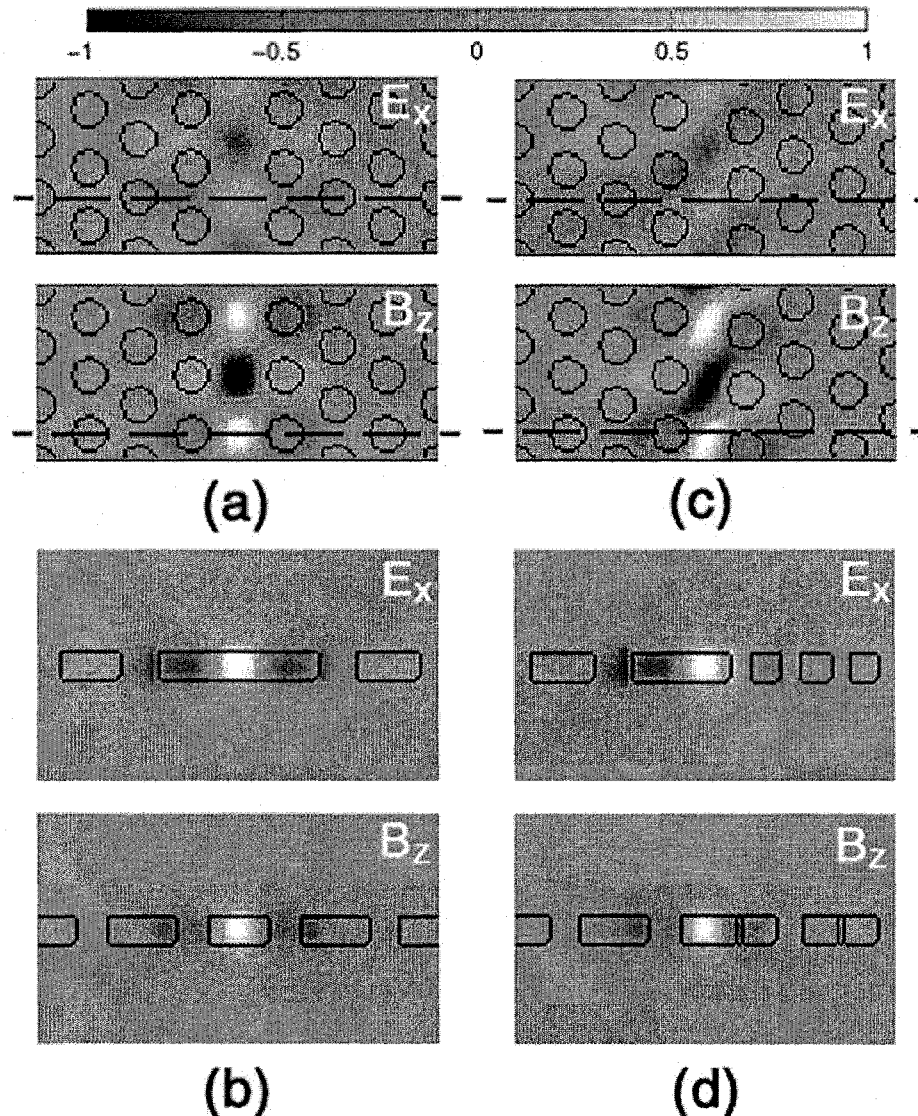


Figure 4.11: (a), (b) Field pattern of the *mode 1* in the *type 1* waveguide for  $M = 5$ . (c), (d) Field pattern of the *mode 1* in the *type 2* waveguide, for  $d = 0.5a$ . (a) and (c) show field profiles at the middle of the slab, and (b) and (d) at the positions indicated by dashed lines in the (a) and (c) respectively. The intensity bar is also shown. Field patterns are shown for  $\beta = \pi/a$ .

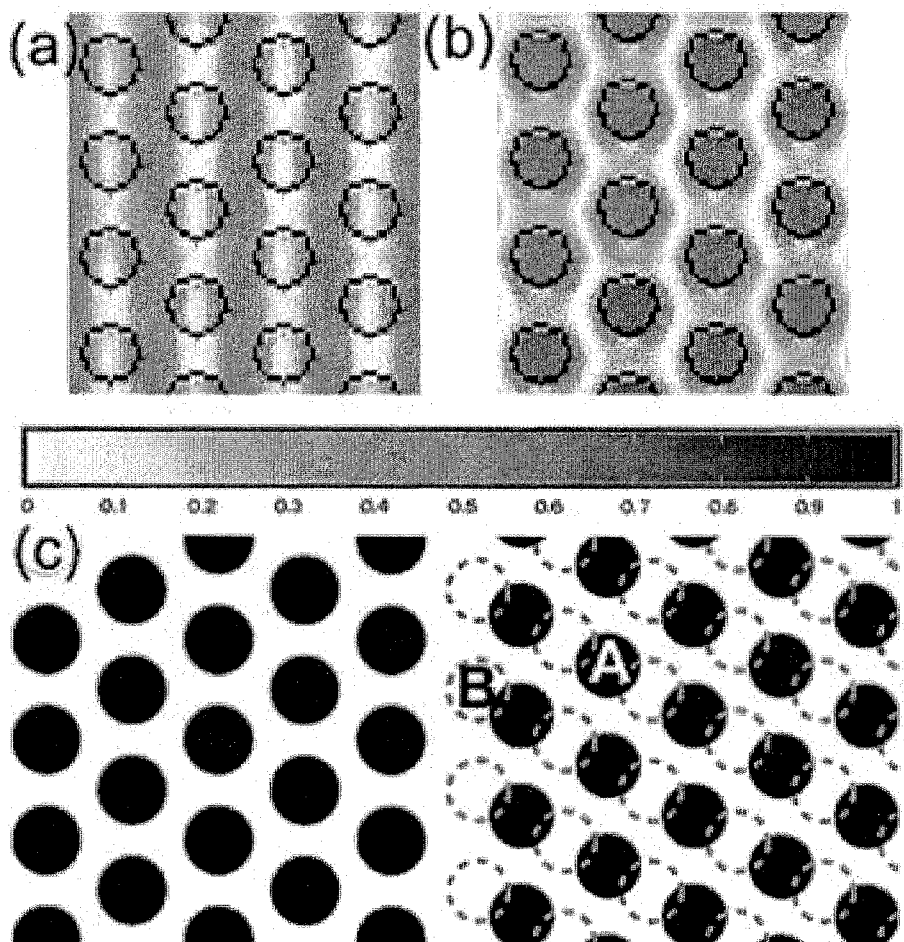


Figure 4.12: Electric field pattern at X point in the unperturbed PPC in the case of (a) dielectric and (b) air band. (c) Black holes - new type of waveguide (for  $d = 0.5a$ ). Black holes at the LHS and open holes at the RHS represent positions of the holes in the unperturbed PPC. The regions where air replaces dielectric (A) and vice versa (B) as we move holes around (black holes at the RHS) are also indicated.

dielectric and air band, respectively. In Figure 4.12(c) unperturbed PPC is represented by the black holes at the left hand side (LHS) and the open holes at the RHS of the figure. The offsetting of the open holes by amount  $d = a$  in  $\Gamma J$  direction is equivalent to the removal of one row of holes - net result is a single line defect waveguide (*type 0*). In either case, there are regions where dielectric material substitutes for air, and therefore modes from the air band are pulled down into the bandgap to form a localized state. However, if the offset is less than  $a$ , for example  $d = 0.5a$  in the case of Figure 4.12(c) (new position of the open holes is represented by the black holes at the RHS), there will be regions where air will appear instead of the dielectric material (A), in addition to regions where dielectric material will replace the air (B). Therefore, modes from the dielectric band will be pulled up into the bandgap, due to their increased overlap with air (*acceptor-type* modes) and modes from the air band will be pulled down into the bandgap due to increased overlap with the dielectric material (*donor-type* modes). This explains the appearance of both types of modes in a *donor-type* waveguide. Therefore, we conclude that, in order to form the waveguide, what matters is not the absolute amount of dielectric material added to the PPC, but rather the relative position of the holes in the unperturbed and perturbed PPC.

#### 4.2.4 Waveguides Based on the Modification of the Hole Size

So far we have investigated properties of three different types of waveguides (including the single line defect waveguide). In all cases, waveguides were formed as narrow regions of high dielectric constant material, surrounded by the PPC mirrors at both sides. The position of the guided mode within the bandgap was then controlled by moving the holes around. Beside this approach, positions of the guided modes can also be controlled by changing the size of the holes in one or more rows. For example, if we increase the radius of the holes adjacent to the single line defect waveguide, we can form a new type of waveguide - *type 3* [Figure 4.13(a)]. This method was proposed and analyzed in 2-D by Adibi et al.<sup>93</sup> Here, we present results of the 3-D FDTD analysis of the structure. In Figures 4.13(b) and (c) we show the dispersion relation for the TE-like guided modes in this waveguide. As expected, by increasing the size of the holes, the modes of the original waveguide (*type 0*) are shifted towards higher frequencies. Also, other modes, in both laterally even and odd case, appear - these are *acceptor-type* modes, pulled up from the dielectric band due to the increased size

of the holes adjacent to the waveguide. This is particularly dramatic in the case of the laterally odd modes, where the *acceptor-type* mode interacts strongly with the *donor-type mode 1*, and the two anti-cross. Therefore, the feature observed in the Adibi et al., the bending of the *mode 1*, is due to its interaction with the *acceptor-type* mode. For  $r_{defect}/a = 0.5$ , all the *donor-type* guided modes are pushed back into the air band (there are some leaky *donor-type* modes, though), and the only modes that remain are the *acceptor-type modes*. In conclusion, this waveguide has a rather complicated band structure, and many modes are present due to the fact that we have changed the properties of three rows of holes. Therefore, it is probably not a good candidate for the efficient controlling of the position of the modes within the bandgap. The advantage of this structure over the *type 1* and *type 2* waveguides is the fact that no holes are moved, and therefore, the structure has exactly the same symmetry as the original triangular lattice. Because of that, it is possible to create not only the  $60^\circ$  bends, but also the  $120^\circ$  ones.

Another promising mechanism of controlling the positions of the guided modes within a bandgap is shown in insets in Figure 4.14(a) and (b). The waveguide is formed by reducing (*donor-type*) or increasing (*acceptor-type*) the radius of one row of holes.<sup>78,89,94</sup>

In Figure 4.14(a) we can observe that by reducing the size of the holes from  $0.3a$  to  $0$ , modes are moving towards lower frequencies. For  $r_{defect} = 0.2a$  (small perturbation to the rest of PPC with  $r = 0.3a$ ) *mode 1* is centered around the midgap frequency. In addition, coupling from an external light source is optimized since there are no leaky modes around the  $a/\lambda_0 \approx 0.29$  range of interest. This structure does not support any *acceptor-type* modes since the waveguide has full symmetry of the triangular lattice and no holes were moved around. The only perturbation is the reduction in size of the holes, and therefore, only the modes from the air band will be pulled down into the bandgap due to the increased overlap with high dielectric constant material. Finally, integration of any kind of cavities with this type of waveguide is very easy since the full symmetry of the triangular PC lattice is preserved.

If we increase the size of one row of holes [Figure 4.14(b)], we form the waveguide that can be used for real single mode operation. By making the holes bigger, the only modes that are localized to the line defect are *acceptor-type* modes. For  $r_{defect} = 0.45a$ , the first order *acceptor-type* mode (*mode 1*) is centered around the midgap frequency, and can be used for

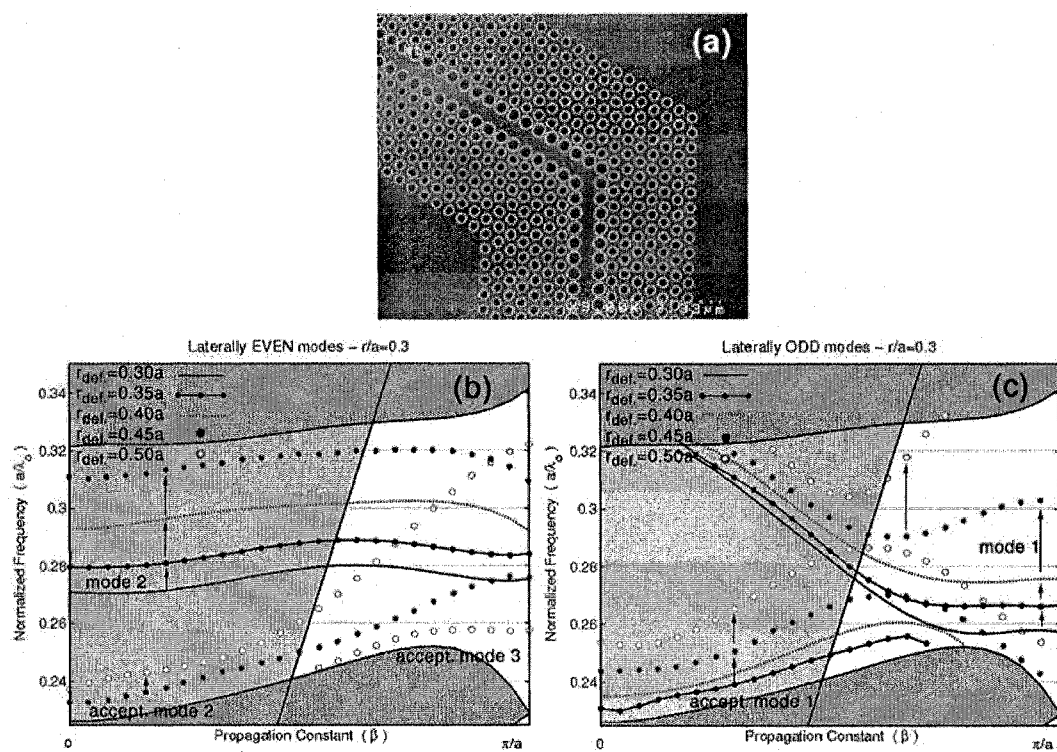


Figure 4.13: (a) SEM micrograph of the fabricated *type 3* waveguide, formed by increasing the size of the holes adjacent to the single line defect waveguide. (b) and (c) Dispersion relations - position of the laterally (a) even, and (b) laterally odd modes as the function of the size of the holes adjacent to the waveguide.

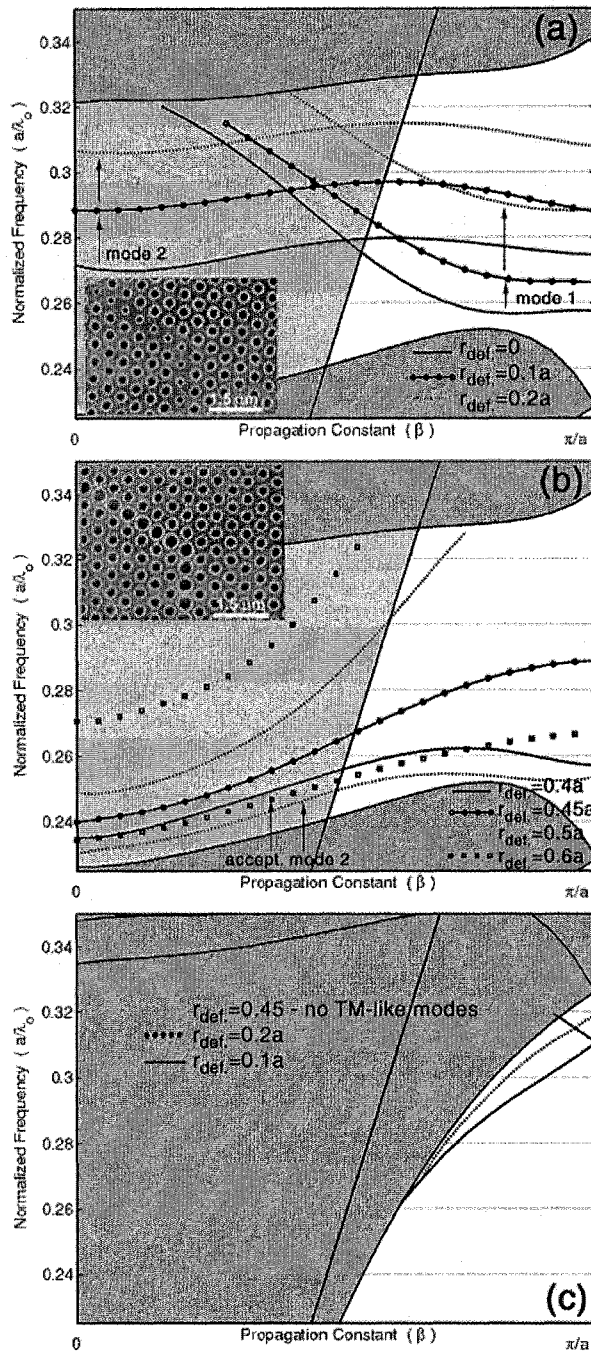


Figure 4.14: Dispersion relation for the guided modes in the (a) *type 4* and (b) *type 5* waveguides, as the function of the radius of the *defect holes* ( $r_{\text{defect}}$ ). Arrows indicate positions of the modes for different values of  $r_{\text{defect}}$ . SEM micrographs of the fabricated structures are shown in the insets. (c) Dispersion diagram for TM-like guided modes supported in *type 4* and *type 5* waveguides.

the guiding of light. This mode is expected to have a higher group velocity than any of the modes described above, due to its slope in the  $\omega - \beta$  dispersion relation. Also, it spans across a wider range than any other mode described so far. These two features are desirable in order to have efficient transport of energy along the waveguide. However, by increasing the size of the holes, the efficiency of turning sharp bends might decrease due to the increased vertical losses since the light is less confined to the slab (bigger holes). This feature needs to be investigated in more detail. This waveguide is a very interesting structure for the investigation of the fundamental properties of the PC guiding mechanism. The reason is the fact that guided modes in this structure are truly PBG effect guided modes. Guiding by effective refractive index contrast is not possible in this structure, since the “core” of the waveguide (line with bigger holes) actually has a smaller effective refractive index than the surrounding PPC (Figure 4.14(c)). Therefore, TM-like modes will not be guided in this structure at all. Therefore, in experiment, any light that is guided, and detected at the output of the waveguide has to be guided due to the PBG effect.

In Figure 4.15(a) and (b) we show field patterns of *mode 1* in the *type 4* waveguide for  $r_{defect} = 0.2a$ , and in (c) and (d) mode of the *type 5* waveguide for  $r_{defect} = 0.45a$ . Both modes have odd lateral symmetry, and  $E_x$  and  $B_z$  have anti-node at the middle of the waveguide. Therefore, it is possible to couple efficiently the TE-polarized light from an external light source into the waveguide. It is interesting to note that in the case of the *type 4* waveguide E-field reaches maximum at the positions of reduced holes [Figure 4.15(a)], and in the case of the *type 5* waveguide at the dielectric regions. This is because in the case of Figure 4.15(a) mode is pulled down from the air-band (E field localized in the holes, see Figure 4.12) and in the case of Figure 4.15(b) mode is pulled up from the dielectric band (E-field localized in the dielectric).

### 4.3 Fabrication

In this section we describe the fabrication procedure for making photonic crystal waveguides in silicon-on-insulator material (SOI).<sup>18</sup> Waveguides with a different number of bends in square and triangular lattices respectively were fabricated. In addition, we have fab-

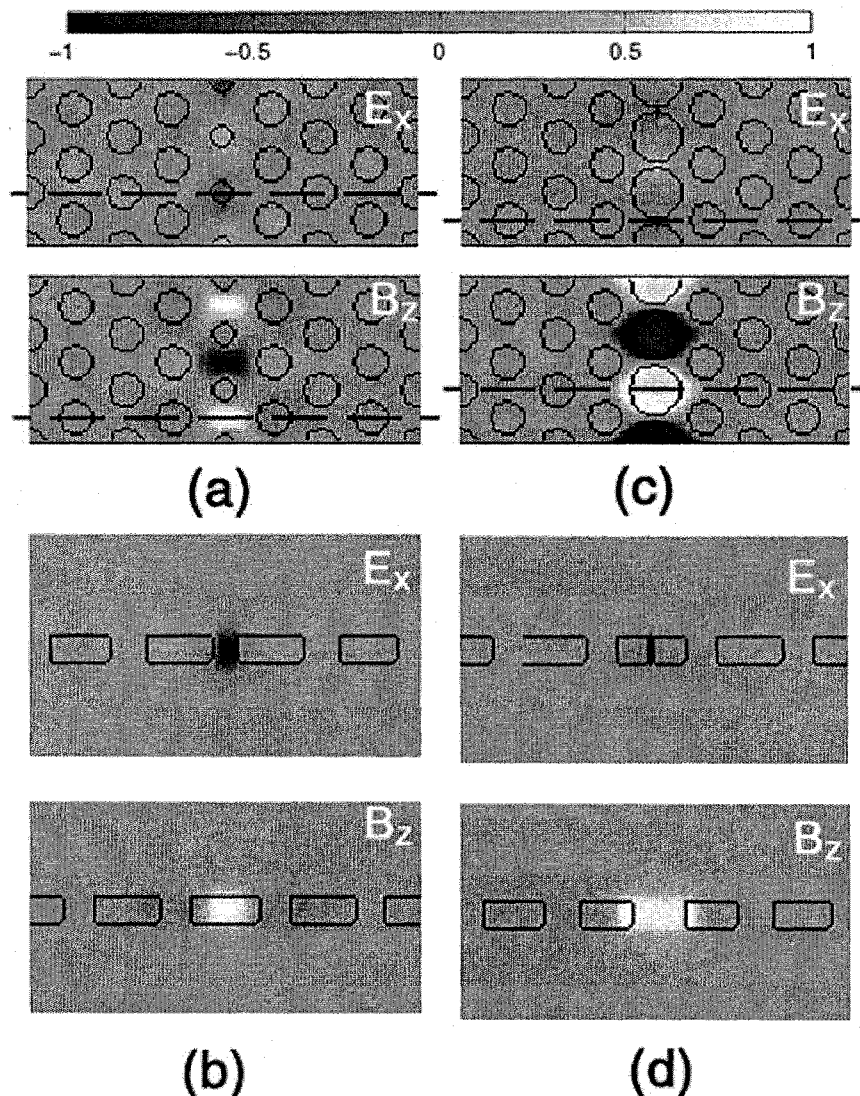


Figure 4.15: (a), (b) Field patterns of the *mode 1* in the *type 4* waveguide with  $r_{defect} = 0.2a$ . (c), (d) Field patterns of the guided mode in the *type 5* waveguide with  $r_{defect} = 0.45a$ . (a) and (c) show field profiles at the middle of the slab, and (b) and (d) at the positions indicated by dashed lines in the (a) and (c), respectively. Field patterns are shown for  $\beta = \pi/a$ .

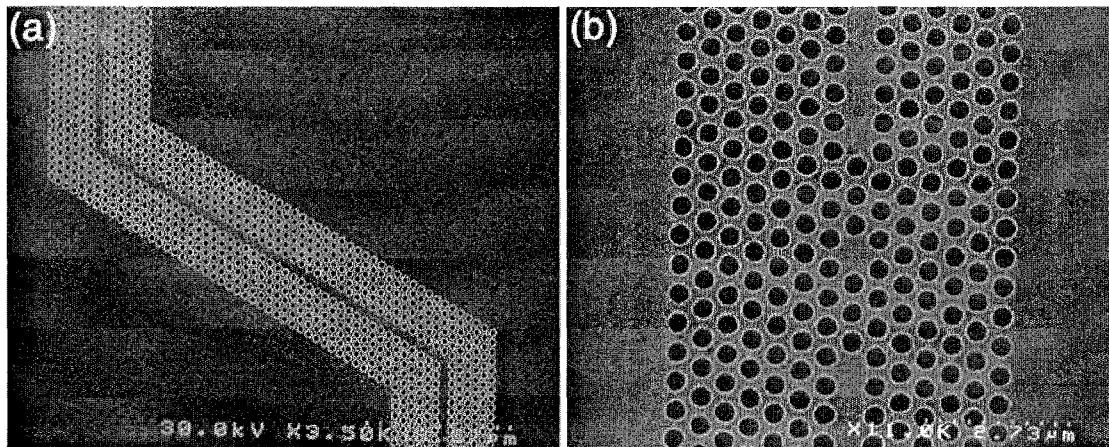


Figure 4.16: (a) Waveguide with two 60 bends and  $25\mu m$  bend-to-bend spacing. (b) High Q cavity filter formed by coupling single defect cavity to the two waveguide sections.

ricated structures that incorporate different types of cavities coupled to the waveguides (Figure 4.16). These types of structures can be used as high Q filters but are also very promising candidates for quantum computing applications.

Our waveguides were fabricated in a Silicon on Insulator (SOI) wafer, as single crystal silicon is known to be transparent within the interesting  $1.3 - 1.7\mu m$  wavelength range. The fabrication techniques to define microstructures within Silicon have been thoroughly researched, and it is possible to obtain large areas of high quality waveguide slabs of known thickness. The advantage of the procedure described here is that, due to the high etching rate selectivity of Polymethylmethacrylate (PMMA) over silicon, no mask amplification procedure is required to define the photonic crystals. Patterns are defined in PMMA using electron beam lithography, and directly transferred into Si using Chemically Assisted Ion Beam Etching (CAIBE).

Table 4.1: The structure of SOI wafer

Layer Number	Layer Type	Layer Thickness
3 (top)	Si slab	340nm
2	SiO <sub>2</sub>	340nm
1	Si substrate	$\approx 500\text{mm}$

The structure of the wafer is shown in Table 4.1 and the whole fabrication procedure is summarized in Figure 4.17. As discussed in Chapter 2, the optimal thickness of the Si slab is around  $0.182 \cdot \lambda$  for a square and  $0.2 \cdot \lambda$  for a triangular lattice. This thickness can be controlled on an SOI wafer by oxidizing the surface of the Si until the desired silicon thickness is obtained.

After oxidation, the formed  $\text{SiO}_2$  layer was removed from the top by dissolution in hydrofluoric acid (49% HF). The sample was then prepared for electron beam lithography. A PMMA, with a molecular weight of 950K, was deposited on the sample by spinning. The sample was then baked on the hot plate at  $150^\circ\text{C}$  for 45 minutes. The resulting PMMA thickness was measured to be  $150\text{nm}$ . Electron beam lithography was performed in a converted Hitachi S-4500 field emission Scanning Electron Microscope operated at 30 kV.  $500\mu\text{m}$  sections of both triangular and square lattice photonic crystal waveguides were defined. The exposed PMMA was then developed in a 3:7 mixture of 2-ethoxyethanol and methanol for 30 seconds and finally rinsed in IPA for 15 seconds. Patterns were then transferred through the Si slab using CAIBE with a 1250V  $\text{Ar}^+$  beam assisted by  $\text{XeF}_2$  as a reactive gas [Figure 4.18(a)]. We measure a 7 : 1 selectivity of Si etch rates versus PMMA in our optimized CAIBE system, which enables us to use relatively thin PMMA layers ( $50\text{nm}$  thick) as etch masks. In addition, the directionality of etch was found to be almost vertical, as can be observed in the Figure 4.18(b). This high selectivity and anisotropy permit us to define high quality photonic crystal structures within SOI silicon structures. However,  $\text{XeF}_2$  etch is known to leave relatively rough etched walls behind. This wall roughness might contribute to the scattering of light and might increase the losses of our waveguides. The etching could be improved using different etch chemistry and a more complicated fabrication procedure. For the purpose of the demonstration of photonic crystal waveguides, this small surface roughness was acceptable. After the CAIBE etching procedure, the PMMA resist was removed from the top of the sample.

In order to be able to couple the light in and out of the waveguide and perform the experimental verification of predicted properties, it is necessary to have access to both ends of the waveguide. To do so, the samples were cleaved at both ends. Prior to cleaving, the sample was mechanically polished from the back side using  $\text{Al}_2\text{O}_3$  polishing powder, and thinned from  $500\mu\text{m}$  to below  $100\mu\text{m}$ . This enabled us to obtain smooth cleaved edges at both ends of the waveguide [Figure 4.18(b)], which is very important in order to reduce the

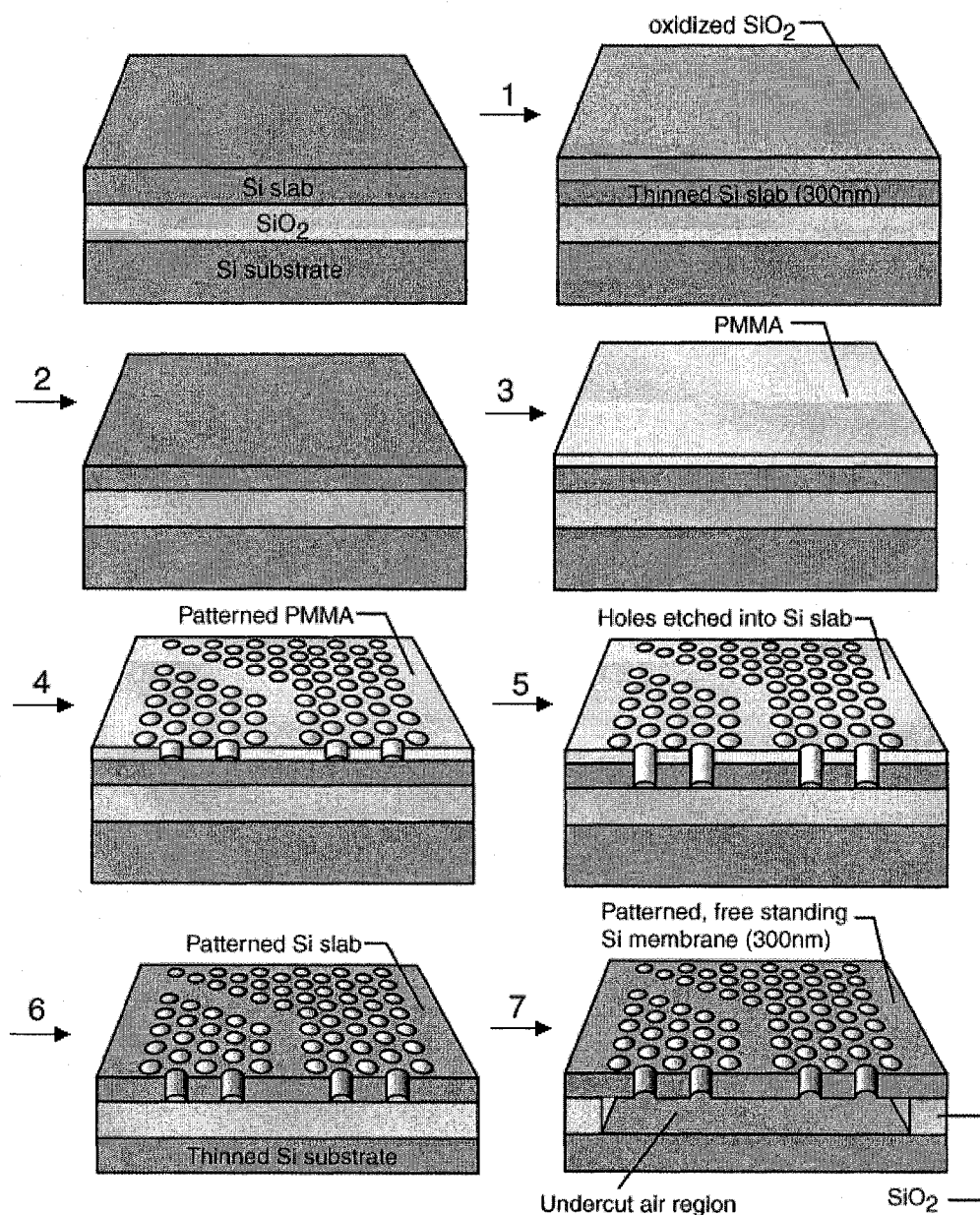


Figure 4.17: Fabrication procedure: 1) oxidation and 2) HF dip in order to define the thickness of the Si slab; 3) deposition of PMMA and 4) electron-beam lithography to define patterns in PMMA; 5) CAIBE to transfer patterns into silicon; 6) removal of PMMA and thinning of the substrate; 7) HF dip to remove SiO<sub>2</sub> layer underneath the waveguide in order to improve the vertical confinement of light.

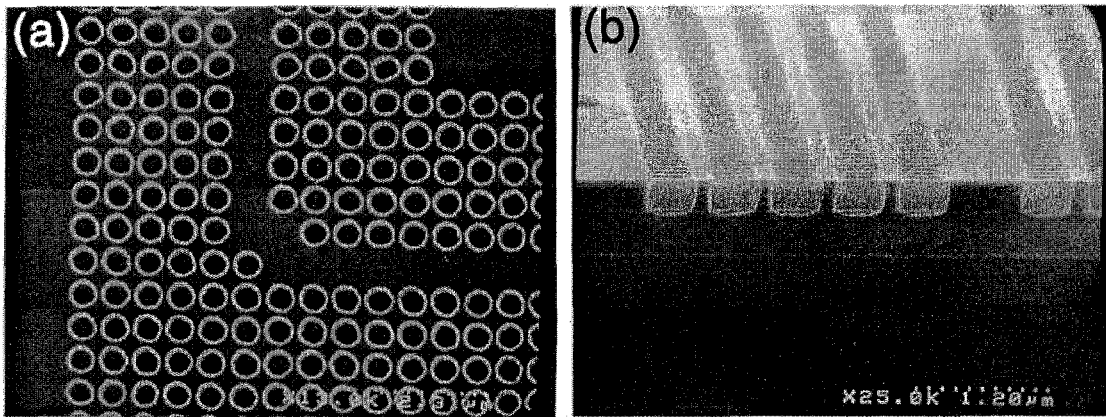


Figure 4.18: (a) SEM micrograph of the  $90^\circ$  bend in the square lattice after CAIBE. (b) SEM micrograph of the cross section of the square lattice waveguide. Layers top-down are Si slab ( $280\text{nm}$ ),  $\text{SiO}_2$  ( $340\text{nm}$ ) and Si substrate. The lattice constant is  $a \approx 500\text{nm}$  and the hole radius  $r \approx 200\text{nm}$ .

insertion losses during optical coupling from a glass fiber to the photonic crystal waveguide.

The final step, undercutting of the waveguide, again required immersion into hydrofluoric acid. This was performed in order to increase the refractive index contrast in the vertical direction and thereby improve the vertical confinement of light within the slab. In addition, by having the slab surrounded by air at both sides, the structure is made symmetric and its eigen modes can be characterized by their symmetry properties in the vertical direction. As we have seen, the bandgap is open only in the case of vertically even modes. If we did not remove  $\text{SiO}_2$  layer, the symmetry would be broken, and the distinction between the even and odd modes of the slab destroyed. Formerly odd modes would come into play and possibly close the bandgap. The  $\text{SiO}_2$  layer underneath the waveguides was removed by dissolution through the ion-etched holes. The fabricated SOI sample was dipped into the 49% HF for 30 seconds, and was then rinsed with de-ionized water for one minute. This process left the Si waveguide and photonic crystal mirror membrane suspended in the air. Figure 4.19 shows the cross section and the top view of a typical photonic crystal waveguide after HF undercutting.

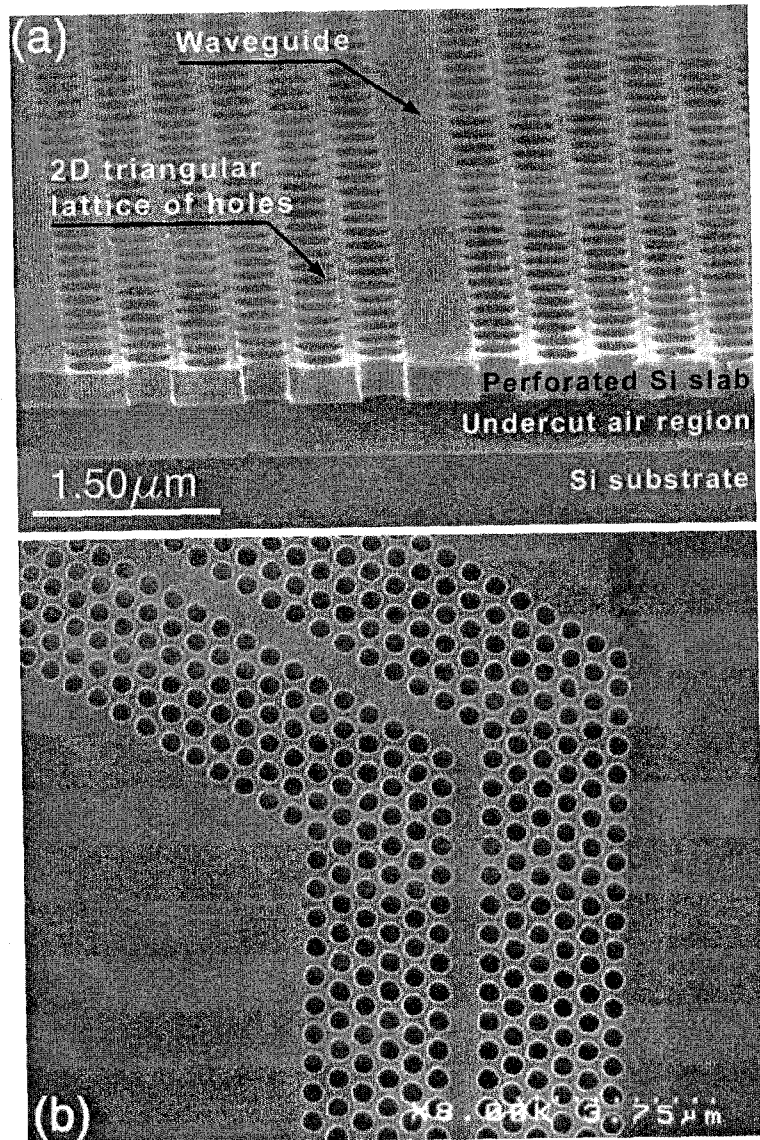


Figure 4.19: (a) SEM micrograph of the cross section of the triangular structure waveguide suspended in the air. Layers top-down are Si slab/ air/ Si substrate. (b) SEM micrograph of  $60^\circ$  bend in the triangular lattice. Area that is undercut extends about  $1\mu\text{m}$  around the waveguide. Parameters of the fabricated structure are  $a \approx 530\text{nm}$ ,  $r \approx 208\text{nm}$  and  $d \approx 300\text{nm}$ .

## 4.4 Experimental Characterization

### 4.4.1 Transmission Measurements

An objective of this work was a *qualitative* characterization of light propagation within single-line defect planar photonic crystal waveguides. Experimental confirmation of light propagation in these novel structures was one of the most challenging and the most competitive research areas in the field of photonic crystals at the time, since PPC waveguides were thought to be the next generation of low-loss optical waveguides. Many groups have tried to obtain experimental evidence of guiding in photonic crystal waveguides, but the race was won by Professor Baba's group at Yokohoma National University (Japan).<sup>95</sup> This first evidence of guiding was followed by works of Tokushima et al.<sup>96</sup> and Lončar et al.<sup>97</sup> Quantitative estimation of propagation losses in PPC waveguides was provided by Notomi et al.,<sup>79</sup> Talenau et al.<sup>98</sup> and Baba et al.<sup>99</sup>

Although photonic crystals waveguides have been around for several years now, their advantage over conventional photonic devices still waits to be experimentally confirmed. While theory predicts their superior characteristics, for example waveguides capable of transmitting light around sharp bends with low losses, real quantitative experimental confirmation is yet to be obtained. This is almost entirely due to the difficulties associated with the characterization of PC devices resulting from their small size. First, it is necessary to couple light from a glass fiber into thin semiconductor slabs with reasonable efficiency. Second, it is important to efficiently couple the light from the slab into the PPC waveguide. Finally, measured light intensity from the exit facet of the waveguide has to be effectively shielded from the scattered light coming from the input.

A tunable semiconductor diode laser [ $\lambda \in (1440, 1590\text{nm})$ ] of rather modest power ( $4\text{mW}$ ) was used to characterize optical transmission. Butt-coupling of a single-mode fiber was used to introduce the laser output into the PC waveguide. Since fiber core diameter is around  $10\mu\text{m}$ , and slab thickness around  $0.3\mu\text{m}$ , coupling from the fiber to the waveguide was not efficient due to a large mode mismatch. This problem can be solved by designing a grating coupler and couple the light from the top into the Si slab, or by incorporating some sort of tapered-coupler to bring the light from the fiber into the intermediate waveguide section, and finally into the photonic crystal waveguide. In our case, sufficient optical power ( $\approx 10\mu\text{W}$ ) is coupled into the guide to carry out the characterization of waveguiding within

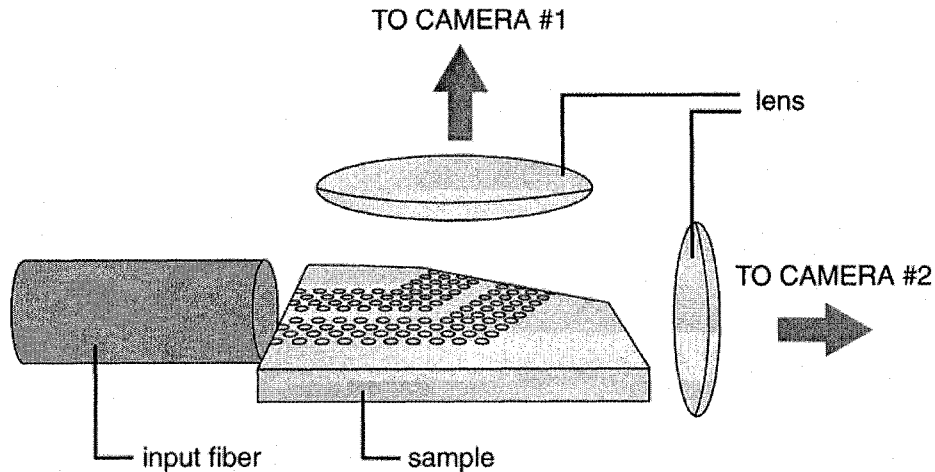


Figure 4.20: Experimental setup for characterization of PPC waveguides.

these structures. The experimental setup used in this experiment is shown in Figure 4.20.

Waveguiding performance was observed by visualization of the guiding structure with two infrared cameras. The first camera (*No.1*), positioned in the plane perpendicular to the sample, was used to observe the light scattered in the vertical direction. The second camera (*No.2*), positioned in the plane of the sample, was used to look at the cleaved output facet of the waveguide in order to observe the output (transmitted) signal. By careful manipulation of the input fiber, we were able to observe apparent guiding over two  $90^\circ$  bends with waveguide segments of  $\approx 200\mu m$  lengths (Figure 4.21) as well as guiding around a  $60^\circ$  bend (Figure 4.22). In order to obtain the evidences of guiding, light was intentionally coupled into the leaky modes of the waveguide. As it can be seen, in both square and triangular lattice photonic crystal waveguides, light propagates in the waveguides, is transmitted around the bend and then propagates in the second section of the waveguide. It can also be observed that light intensity in the waveguide segments after the bends is much weaker than the light intensity in the first part of the waveguide. This can be attributed to significant losses associated with the bending of the PPC waveguide. This is in contradiction with our expectation that PPC waveguides have superior bending efficiency over conventional waveguides. This significant loss can be attributed to the following effects:

### 1. Coupling to leaky modes

In order to obtain evidence of guiding within the PPC waveguide, light was inten-

tionally coupled into the leaky modes of the waveguide. These modes might not have high bending efficiency as the modes below the light line. Indeed, as it will be shown below, for the lattice with  $r/a = 0.4$  we predict small bending efficiency for the leaky modes around the mini stop bend.

## 2. Partially TM-like polarized light

Since the light was launched into the waveguides using tapered optical fiber, it was not possible to control the polarization of the light coupled into the waveguides. Therefore, significant TM-like polarized component might exist in the waveguide, and light with this polarization is not expected to have high bending efficiency due to the lack of photonic bandgap for these modes.

## 3. Wrong propagation constant

As it was shown in original work by Mekis et al., high transmission efficiency can be achieved only in a certain frequency band, and only for the range of propagation constants  $\beta$ .

In Figure 4.22 it is interesting to note the difference between two different corner designs. In the case (b), waveguide with cavity in the corner, light is localized in the corner. This is expected since the cavity supports bound states. This cavity serves as a “mode converter” and improve the coupling between two waveguide segments, thereby improving the bending efficiency. However, the useful bandwidth of the waveguide is limited upon introduction of the cavity and the tradeoff between two requirements needs to be made. Simple corner design, without an additional cavity, does not support bound states.

Whereas results shown in Figures 4.21–4.22 is instrumental in qualitative visualization of light propagation within the PC structures, the optimization of true waveguiding requires the observation of the guided mode exiting from the PC sample. This is particularly important to distinguish between light scattered from the surface due to the holes of the PPC lattice, and light coupled into and “emitted” from the waveguide, as in the case of real leaky/guided modes of the structure. For example, results similar to those shown in Figures 4.21 and 4.22 were obtained when light from a HeNe laser ( $\lambda = 650\text{nm}$ ) was directed towards the sample. In this case, light cannot be coupled into the waveguide, since it is outside the useful bandgap frequency range, and the signal is attributed to the scattering from the surface of the sample. Therefore, in order to obtain unambiguous evidence

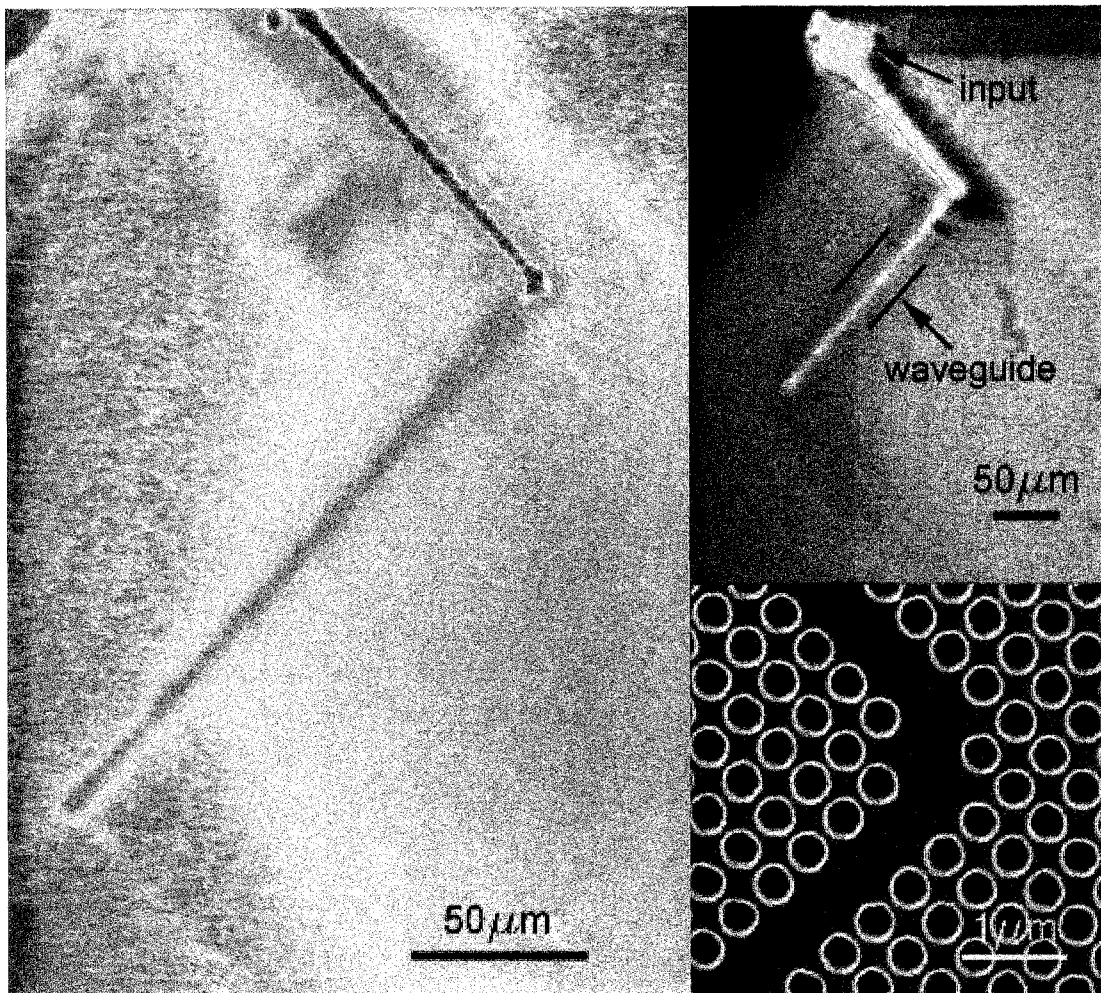


Figure 4.21: Light guided in the waveguide around two 90 bends (top view). It can be seen that the light is confined to the waveguide (upper right inset). Inset in the lower right corner shows the SEM micrograph of the corner design in the square lattice. Visualization of light propagation is made possible by coupling intentionally to leaky modes which radiate from the top surface of the guide. Enhanced losses for these modes can be seen at the sharp bends.

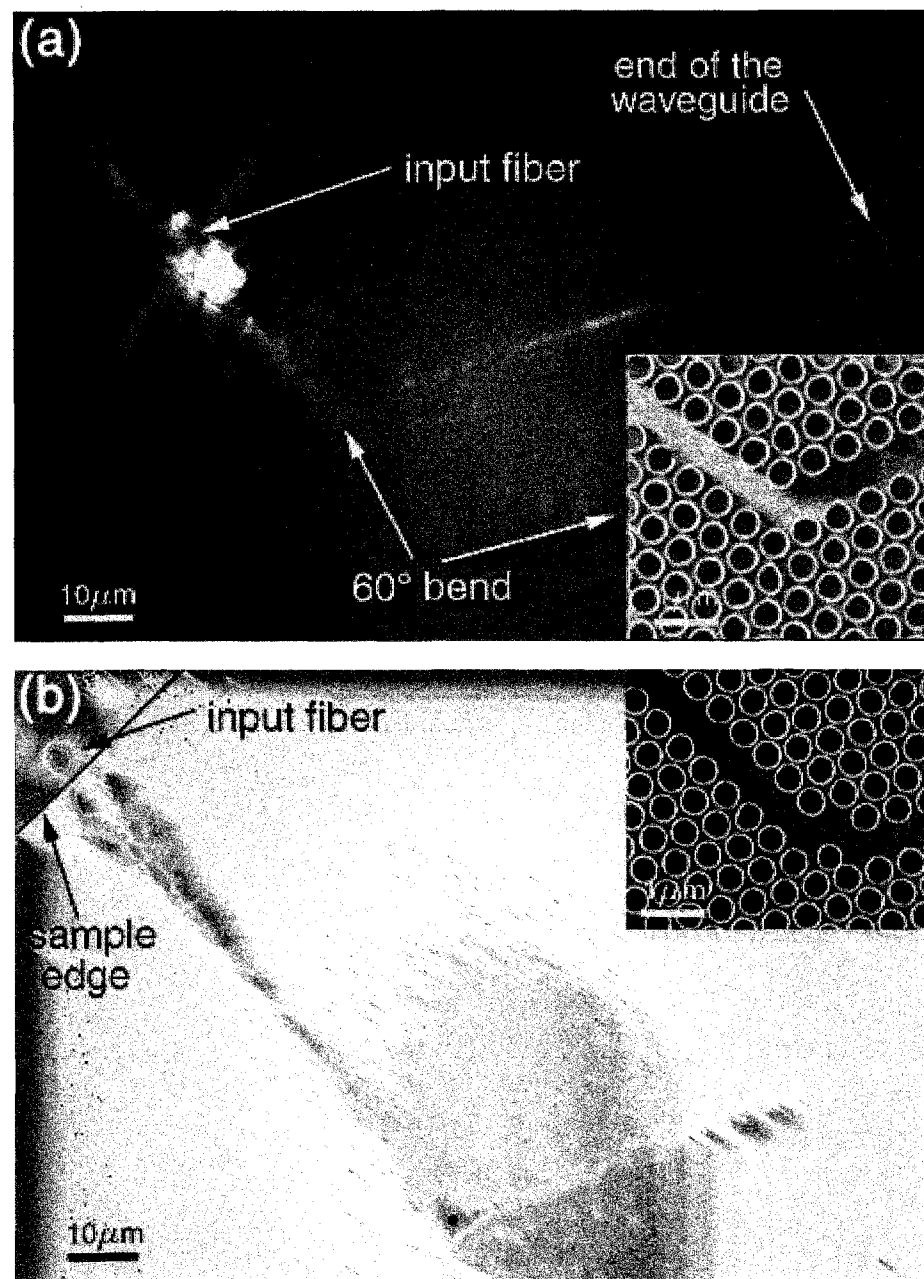


Figure 4.22: Visualization of light guided in the triangular lattice single line defect waveguide around 60° bend in the case of (a) simple corner design and (b) corner with cavity.

of guiding we need to look at the output of the waveguide and not into the “leaks”. By reference to the output camera (*No.2*), we were able to confirm that true guiding by the PC is obtained by a different set of coupling conditions. Under these conditions, a clear guided mode is observed at the output facet of the waveguide, and very little light is scattered out of the waveguide perpendicular to the wafer. For the case where the fiber was correctly aligned to the waveguide, Figure 4.23(a), camera *No.2* detected two signals, marked A and B. The light in spot A has a significant component that is not coupled from the input fiber into the waveguide and is therefore of little interest for characterization. This is due to the big mismatch between the input fiber and the waveguide. Also, this signal contains a TM-like polarized component of the light coupled into the waveguide, since it does not make it around the corner due to the lack of the photonic bandgap. On the other hand, spot B represents the light that is guided around the sharp  $60^\circ$  bend in the PC waveguide. The distance between the  $60^\circ$  bend and the output of the waveguide was about  $50\mu m$ . This distance is sufficiently large to distinguish easily between the signals A and B. Figure 4.23(c) shows detected output power as a function of position along the cleaved output facet of the waveguide. On the left hand side is an intensity scan of spot B corresponding to the guided mode. Between B and A any measured intensity would correspond to light scattered out of the guide through the PC (loss in the lateral direction). It can be seen that this intensity is below the threshold of the camera used. This result suggests that lateral confinement of light in PC waveguides is very good.

When the fiber was not aligned to the waveguide, Figure 4.23(b), camera *No.2* registered only one signal (A) - the one coming directly from the fiber. The other signal was not present since there was no light coupled into the waveguide. Similarly, when we moved the fiber in the vertical direction, guided signal (B) was present and not present depending on the relative position of the waveguide and the fiber. Therefore, we can conclude that signal B corresponds to the guided mode in this PC waveguide.

#### **4.4.2 Measurement of the Dispersion of the Guided Modes**

The qualitative evidence of guiding described in previous section was one of the first experimental observations of light propagation within photonic crystals. While our experiments showed that it is possible to guide the light in these structures, they also suggested that

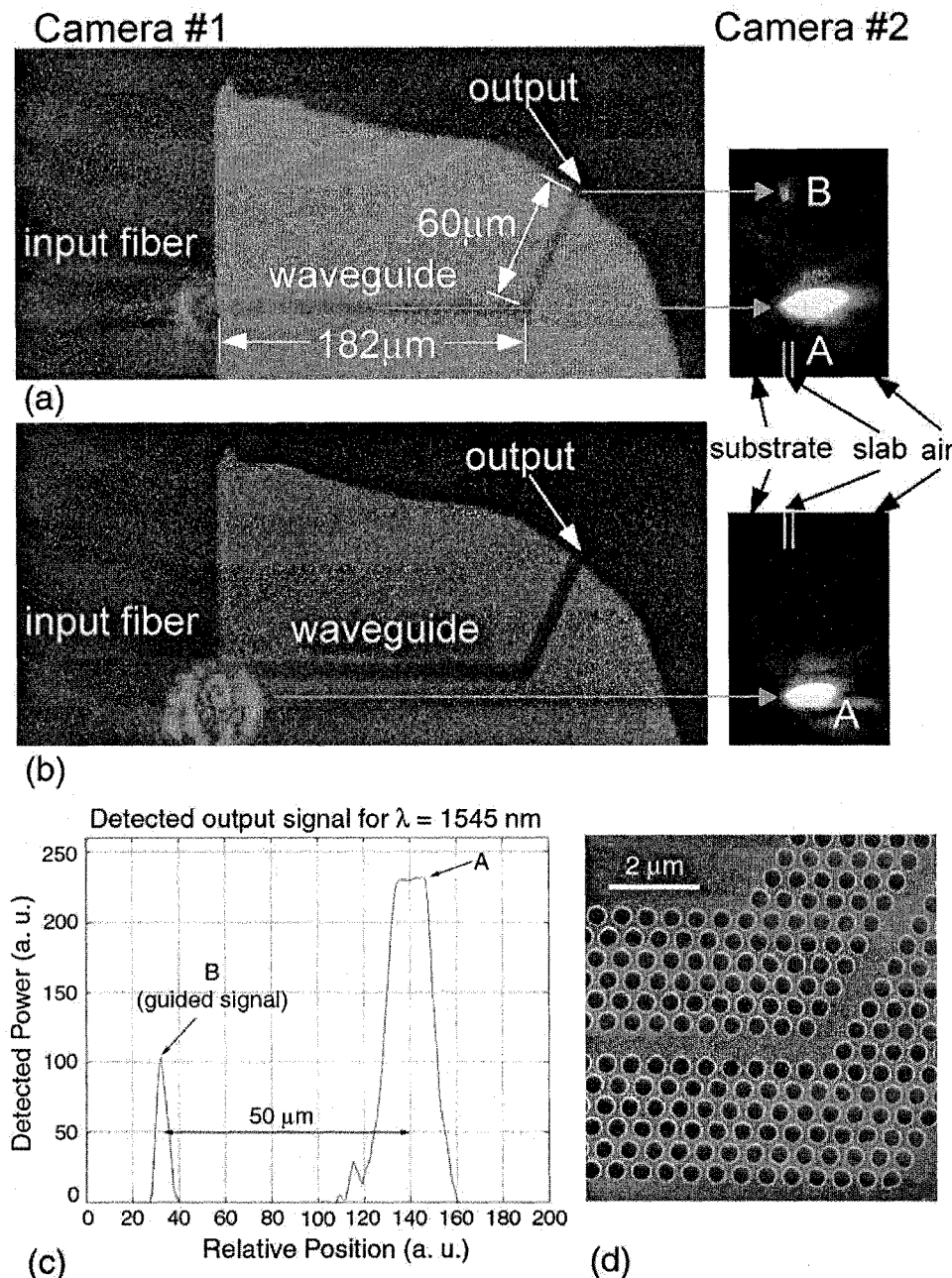


Figure 4.23: Waveguiding at  $\lambda = 1550 \text{ nm}$  around a  $60^\circ$  bend. Two cameras are used simultaneously, a top (camera No.1) and in-plane view (camera No.2) of the tested structure. (a) When input fiber is aligned to the input of the waveguide, an output signal, transmitted around  $60^\circ$  bend is detected (signal B) and (b) when it is misaligned a transmitted signal is not present. The position of the slab is indicated with two parallel lines. (c) Detected output power (arbitrary units) at different positions along the cleaved output facet of the waveguide. Two peaks correspond to the signals A and B. The figure is obtained as a line scan of the Figure 4(a) along the middle of the slab.

the propagation losses are rather high. These losses are at least an order of magnitude higher than losses in conventional waveguides fabricated in low refractive index contrast materials (e.g., glass), and they can be attributed to scattering losses due to imperfections in the fabrication of PPC waveguides. On the other hand, since structures fabricated in high-index contrast platforms are much smaller than ones fabricated in glass, it is necessary to transport the light for shorter distances only, and therefore higher losses might be acceptable. However, cross talk between adjacent waveguides still remains to be a big problem since the light scattered from one of the waveguides can couple into neighboring waveguide and contribute to the noise in that channel. At the same time there have been reports, both experimental and theoretical, on efficient light propagation in conventional waveguides fabricated in SOI material. For all of these reasons we concluded that PPC waveguide offers little advantage over conventional waveguide when they are used for a plain transport of photons from one point to another. However, unusual dispersion properties of PPC waveguides still make them interesting for applications like enhanced nonlinear phenomena, compact interferometers, dispersion compensators, etc. These applications are based on the fact that light can be significantly slowed down in PPC waveguides,<sup>79,80</sup> and that their dispersion properties can be controlled by modifying their geometry. The goal of this work was an experimental investigation of the dispersion properties of the modes of single-line defect planar photonic crystal waveguides.

In our experiments, we have tested two different structures: the first one was a single line defect waveguide with a single  $60^\circ$  bend in it, and the second was a straight waveguide with a single defect cavity in the middle. At first we show numerical and experimental results for the waveguide with the cavity in it. In this case, the cavity was surrounded by three layers of photonic crystal on each side (Figure 4.24). Numerical analysis of the experiment is shown in Figure 4.25. In this case, light was excited with the dipole sources positioned at the entrance of the waveguide. As expected, light coupled in the waveguide, travels towards the cavity. The light with a frequency different from the cavity resonance is reflected back and interacts with a forward propagating wave, forming the standing wave as observed in Figure 4.25.

These standing waves were also detected in experiments. In the Figure 4.26 we show the pattern of light coupled out of the top surface of the waveguide structure and detected by

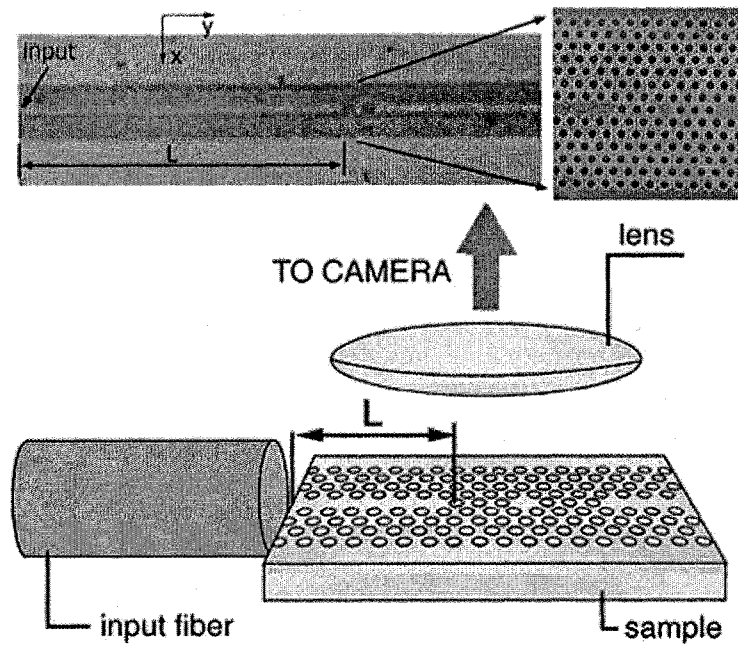


Figure 4.24: Experimental setup. The structure that we have characterized is a single line defect waveguide with a single defect cavity in it.  $L \approx 122\mu m$ .

the camera. At nearly every wavelength, a clear periodic intensity modulation can be seen along the waveguide direction. It should be noted, however, that at  $1495nm$  and  $1505nm$  this modulation intensity has nearly disappeared. It can further be seen that the spatial periodicity of this modulation grows shorter as the difference between the wavelength and  $1500nm$  grows larger, in *either direction of the wavelength*.

In order to better understand these results it is necessary to extract information on the spatial periodicity of the modulation pattern (that is propagation constant  $\beta$ ). Once we get  $\beta$  for each wavelength ( $\lambda$ ) of the light coupled into the structure, we can map out the dispersion diagram of the mode excited in the waveguide, that is the relation  $a/\lambda = f(\beta)$ . We have analyzed our experimental results using a fast Fourier transform (FFT), and the results are shown in Figure 4.27. The black dots in this figure represent results from our 3-D FDTD simulation (shown only in the frequency range of interest) whereas the black solid lines are polynomial fit to these numerical results. One unit cell of the waveguide, with Bloch boundary conditions applied in the direction of propagation ( $y$ -axis), was modelled

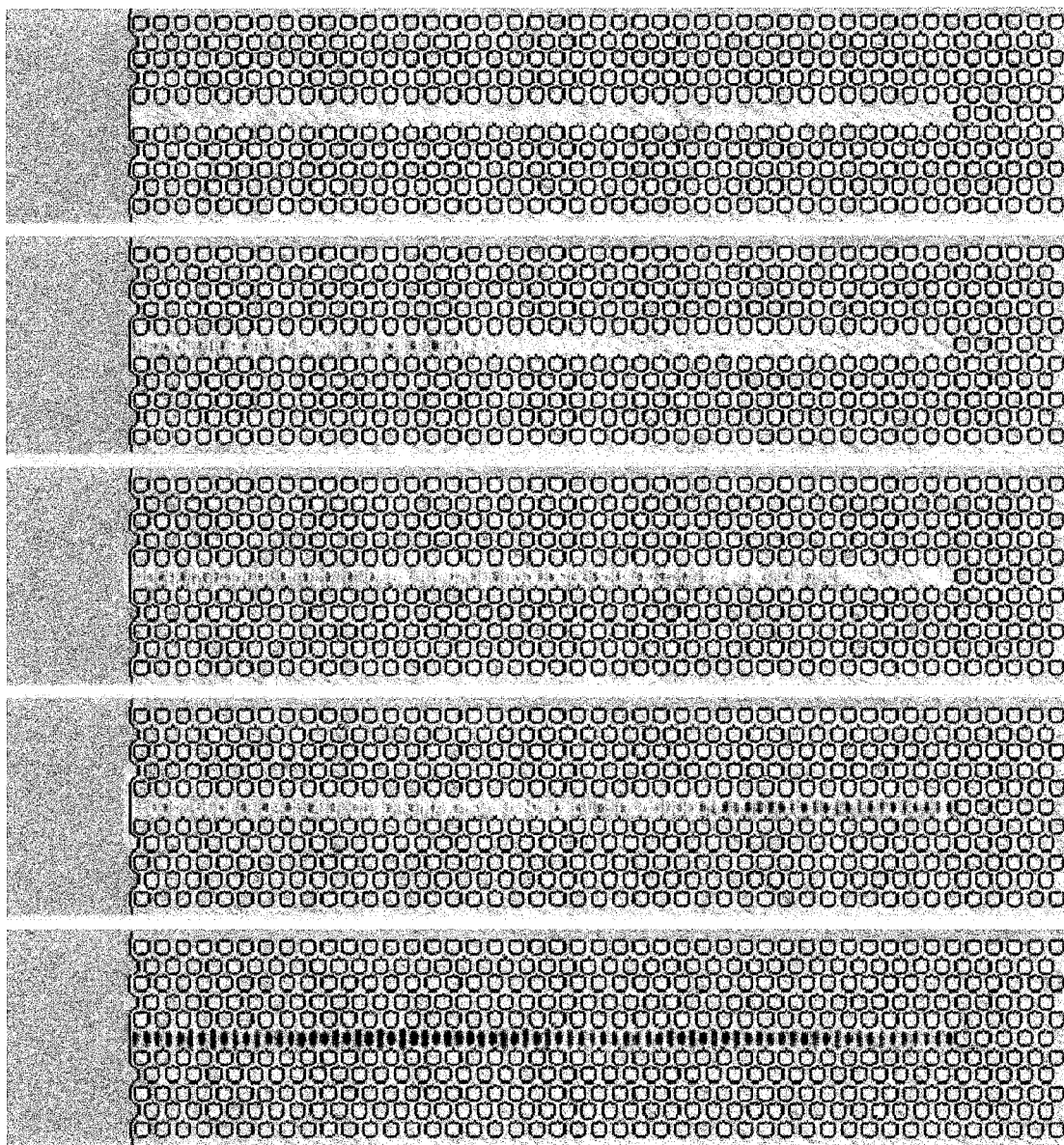


Figure 4.25: Formation of the standing wave in the numerical model of our experiment. Waveguides, closed with cavities at one side, are excited with dipole sources at the entrance of the waveguide (left-hand side).

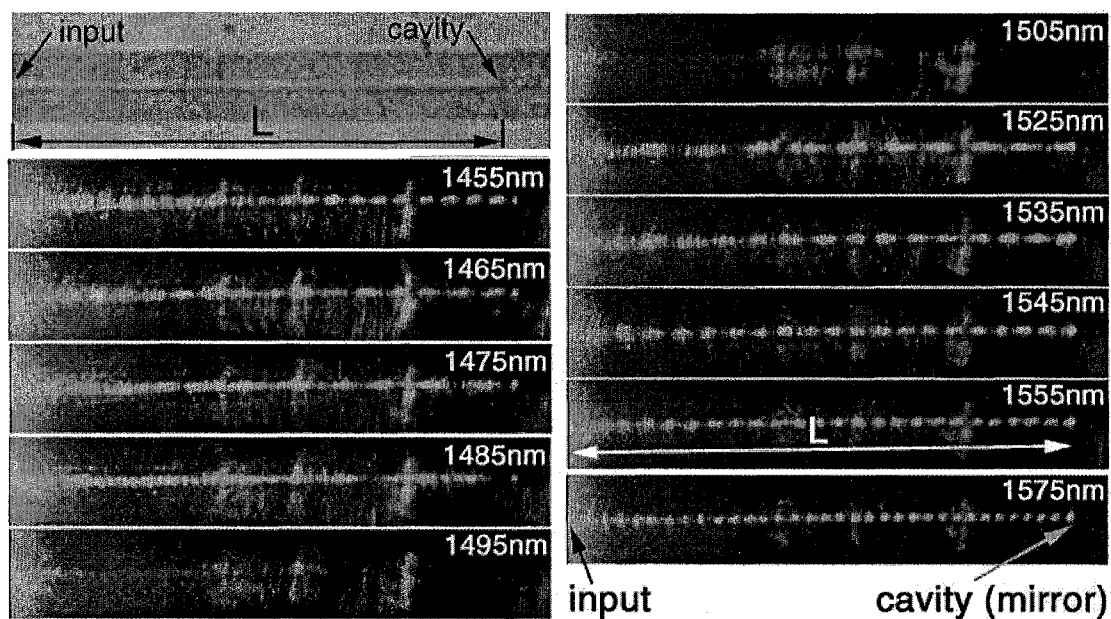


Figure 4.26: Wavelength dependence of the signal scattered in the vertical direction, detected by the camera. Periodic intensity modulation can be observed for all wavelengths except for  $\lambda \in (1490\text{nm}, 1510\text{nm})$ . Periodicity of this modulation grows shorter as the difference between the wavelength and  $1500\text{nm}$  grows larger, in either direction of the wavelength. An optical microscope image of the structure is also shown.  $L = 122\mu\text{m}$ .

in order to obtain the dispersion diagram. The region shown in blue in Figure 4.27 is the result of the FFT of the line scans along the patterns shown in Figure 4.26. The experimentally detected propagation constants are represented by light blue dots, for each normalized frequency. It can be seen that our experimental results are in very good agreement with the 3-D FDTD simulations. The slight shift of the experimental results towards the higher frequencies can be attributed to the difference between the refractive index of Si used in the simulation ( $n_{Si} = 3.5$ ) and the refractive index of Si slab used in the experiment, fabrication tolerances and the resolution of the FDTD algorithm ( $a = 20$  computational points). Experimental results also show the presence of a small stop-band around  $a/\lambda = 0.353$ , as predicted by 3-D FDTD analysis. Our experimental results can now be explained in the following way: light from the tunable laser source is coupled to leaky  $e_1$  mode of the waveguide, and as it propagates down the waveguide (towards the single defect cavity) it radiates energy in the vertical direction since the mode is leaky (above the light line). The light in the frequency range of our laser [ $a/\lambda \in (0.333, 0.368)$ ] can not couple to the mode of single defect cavity since it is located at frequency  $a/\lambda = 0.326$ . Therefore, the light is reflected back and interferes with the forward-propagating light forming the standing wave pattern observed in Figure 4.26. The cleaved input facet and the single defect cavity act as mirrors, and light coupled to the leaky modes of the waveguide resonates between them. This experimental finding is in excellent agreement with results of numerical modeling shown in Figure 4.25.

It is interesting to note that a pattern similar to the one shown in the Figure 4.26 was observed between the input facet and the  $60^\circ$  bend during characterization of the SLD waveguide with  $60^\circ$  bend in it. Figure 4.28 shows the standing wave pattern formed between the input facet of the waveguide and the  $60^\circ$  bend. This indicates that the reflection of the leaky  $e_1$  mode from the bend is significant, and that the transmission around the bend is small. Indeed, 3-D FDTD simulation of the structure [Figure 4.28(b)] shows both features: formation of the standing wave pattern in the input portion of the waveguide, and low transmission around the bend. For example, the bending efficiency is only 15% when  $a/\lambda = 0.345$ . Poor transmission efficiency can also be explained by following the simple symmetry argument: mode  $e_1$  has an odd symmetry (antinode of the  $B_z$  field at the center of the waveguide) with respect to the symmetry plane that cuts along the center of the

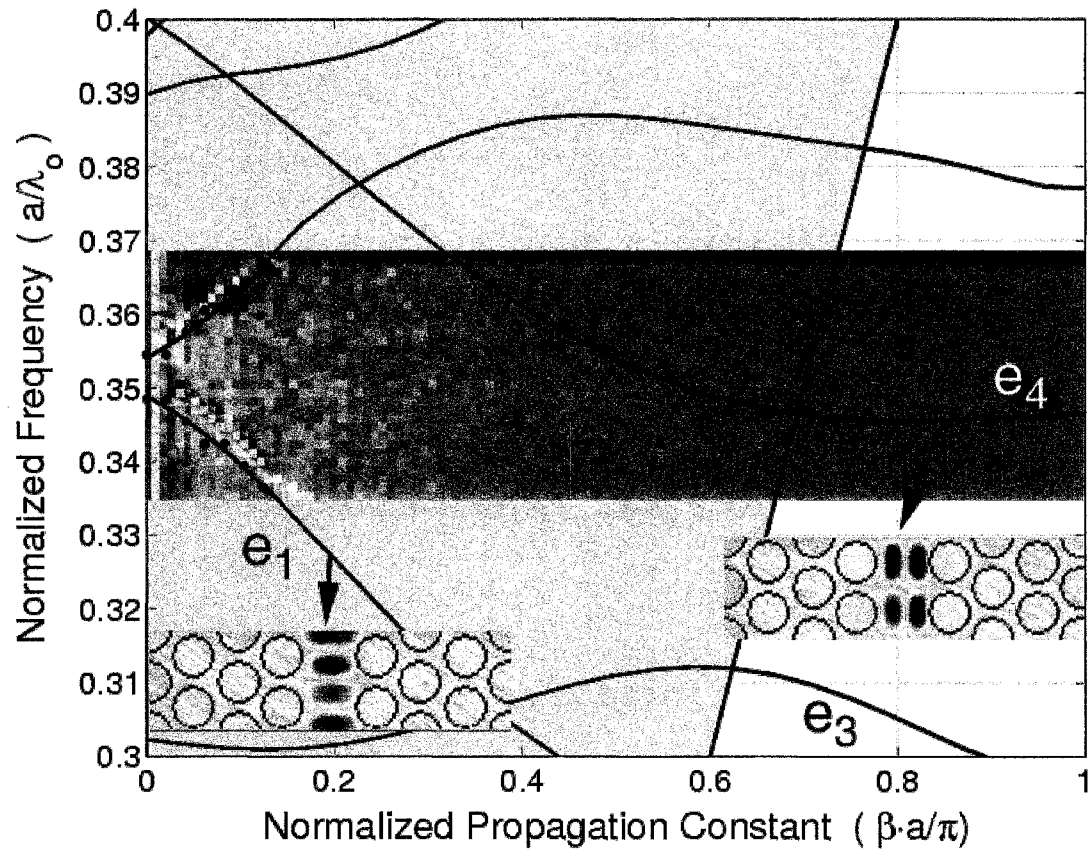


Figure 4.27: Experimentally mapped dispersion diagram of the leaky TE-like modes supported in the waveguide, overlaid onto the calculated diagram (black solid lines). Frequency range probed in the experiment is shown in blue. The light-blue pixels represent the spatial frequencies ( $\beta$ ) detected in the spectrum of the periodic intensity modulation pattern recorded by the camera. Insets show mode profiles ( $B_z$ ) for the two modes of interest. The light line is represented by the straight solid line, the leaky-modes region in light-gray, and the extended states of photonic crystal in dark-gray.

waveguide (x-z plane). Also, it can be seen that the mode has spatial periodicity  $\approx a$  in the direction of propagation. Therefore, the whole period of spatial oscillation can fit within the waveguide bend - that is, within the bend mode reaches both negative and positive amplitude. Transmission around the bend can be understood as sequence of following events: light that arrives to the bend acts as a source that excites the modes in the second section of the waveguide (after the bend). Since the “light source” in the bend has an even symmetry (both negative and positive amplitude), it will not be able to efficiently excite the odd  $e_1$  mode in the second section due to the symmetry argument. As long as the waveguide is single mode, very little light can be transmitted around the bend in the same  $e_1$  mode. If the waveguide is not single mode at the frequency of interest, then light in the bend can couple into other modes, but with reduced conversion efficiency. This multimode feature and weak bending efficiency can be observed in Figure 4.28 as a weak signal after the bend.

The guided modes, on the other hand, are expected to have much better transmission efficiency. For example modes close to the edges of the Brillouin zone will have spatial periodicity of  $2 \cdot a$ , and therefore it will be possible to fit only half the spatial period within the waveguide bend. Therefore, the second section of the waveguide, after the bend, will be excited with the “light source” of *appropriate* symmetry, resulting in high transmission efficiency. By including some sort of defect in the bend (e.g., cavity) we can break the symmetry of the mode even in the case of leaky modes, and high transmission efficiency can be achieved.

As a next step, we wanted to estimate the transmission losses of the leaky modes supported in our single line defect waveguide. Figure 4.29 shows normalized light intensity (in dB) in the waveguide as a function of position along the waveguide, obtained from Figure 4.26. This result can be used to estimate propagation losses by calculating the reduction in signal intensity along the waveguide. Due to multiple reflections of the light in the waveguide (from both input facet and cavity), it is not straightforward to calculate waveguide losses with high accuracy by looking at this standing wave pattern. However, it can be observed that the light signal detected at the end of the waveguide is stronger when the frequency is closer to the mini stop band. Therefore, we can conclude that the losses are growing smaller as we approach the mini stop band.<sup>80,100</sup> This is a somewhat unexpected result, and it predicts the existence of long-life time modes in the waveguide section be-

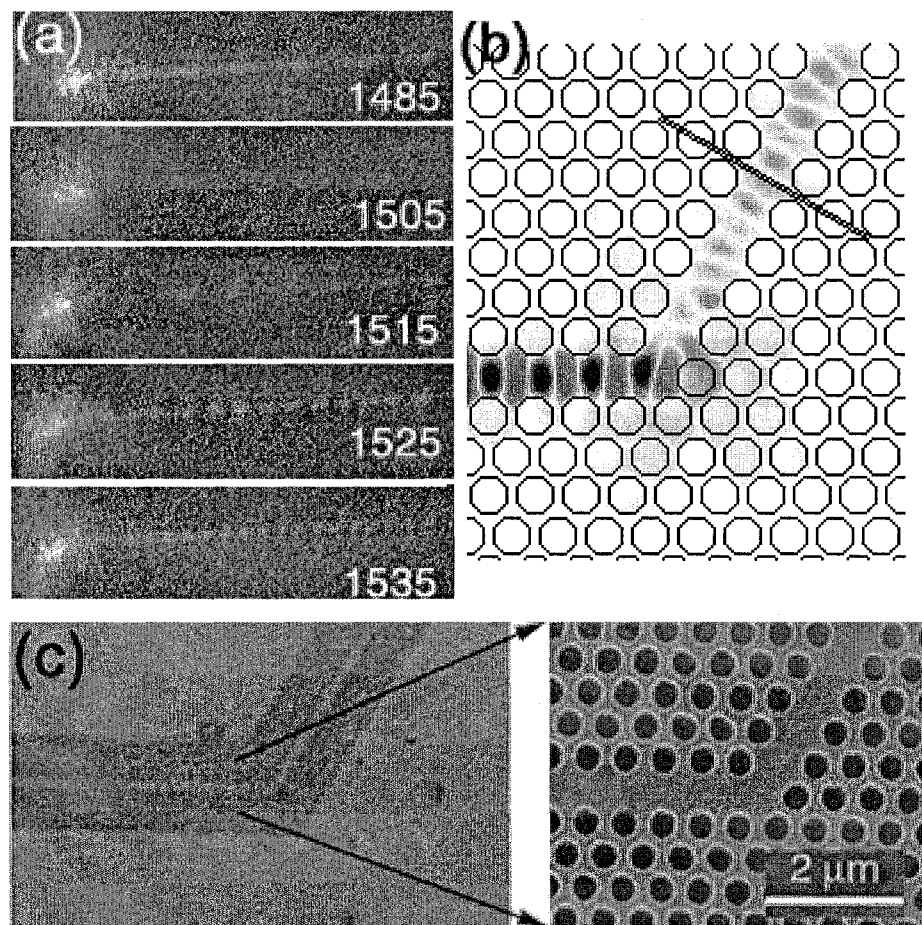


Figure 4.28: Standing wave formed in a waveguide with bend. (a) Experiment and (b) 3-D FDTD simulation.

tween the single-defect cavity and cleaved input facet of the waveguide. Leaky modes with long life times have been theoretically predicted in the bulk planar photonic crystal lattice by Sakoda et al.<sup>101</sup> Also, our experimental findings were recently confirmed in theory by Andreani et al.<sup>102</sup>

In order to understand this reduction in transmission losses we have numerically analyzed waveguide section formed between two PPC mirrors [Figure 4.30(a)]. The structure was excited using dipole sources of fixed frequency. Choosing the symmetry of the dipole sources we were able to excite only the leaky modes ( $e_1$ ). This was also confirmed by inspecting the field profile ( $B_z$  component at the middle of the slab) of the excited mode, for each frequency [Figure 4.30(a)]. Due to the memory limitations of our computers (1Gb of memory), the length of the waveguide section was chosen to be  $40.5 \cdot a$  ( $a = 12$  points in 3-D FDTD algorithm) instead of the  $\approx 230 \cdot a$ , as it was in our experiment. In order to make calculations easier, the waveguide section was also closed with PPC at both ends. This change should not affect the profile of the standing wave formed in the waveguide section. The results are shown in Figure 4.30(b) that shows profiles of the  $P_z$  component of the Poynting vector in case when leaky modes were excited at three different frequencies. Periodic intensity modulation can be seen. The periodicity of this standing wave pattern has the same trend with respect to the frequency as in the experiment: it becomes longer as the frequency approaches the mini stop band. It is important to say that this standing wave pattern was detected at a distance of about  $1\mu m$  from the surface of the sample. This is again in excellent agreement with the experiment, where the standing wave pattern was observed above the sample, i.e. at a different focal distance from the one used to image the surface of the sample.

The dispersion diagram for the TE-like modes supported in the single line defect PPC waveguide is again shown in Figure 4.31. The geometry of the analyzed structure is  $r/a = 0.4$ ,  $t/a = 0.55$ ,  $n_{Si} = 3.5$  (refractive index of silicon) and  $a=20$  computational points. Mode  $e_1$  (encircled) is the one of interest in this work. That mode is mainly effective refractive index contrast guided, and it appears to be folded back into the first Brillouin zone by the periodicity of the lattice. The mini stop band open for  $\beta = 0$  is an indication that the mode  $e_1$  is affected by the lattice periodicity. Because of the discrete translational

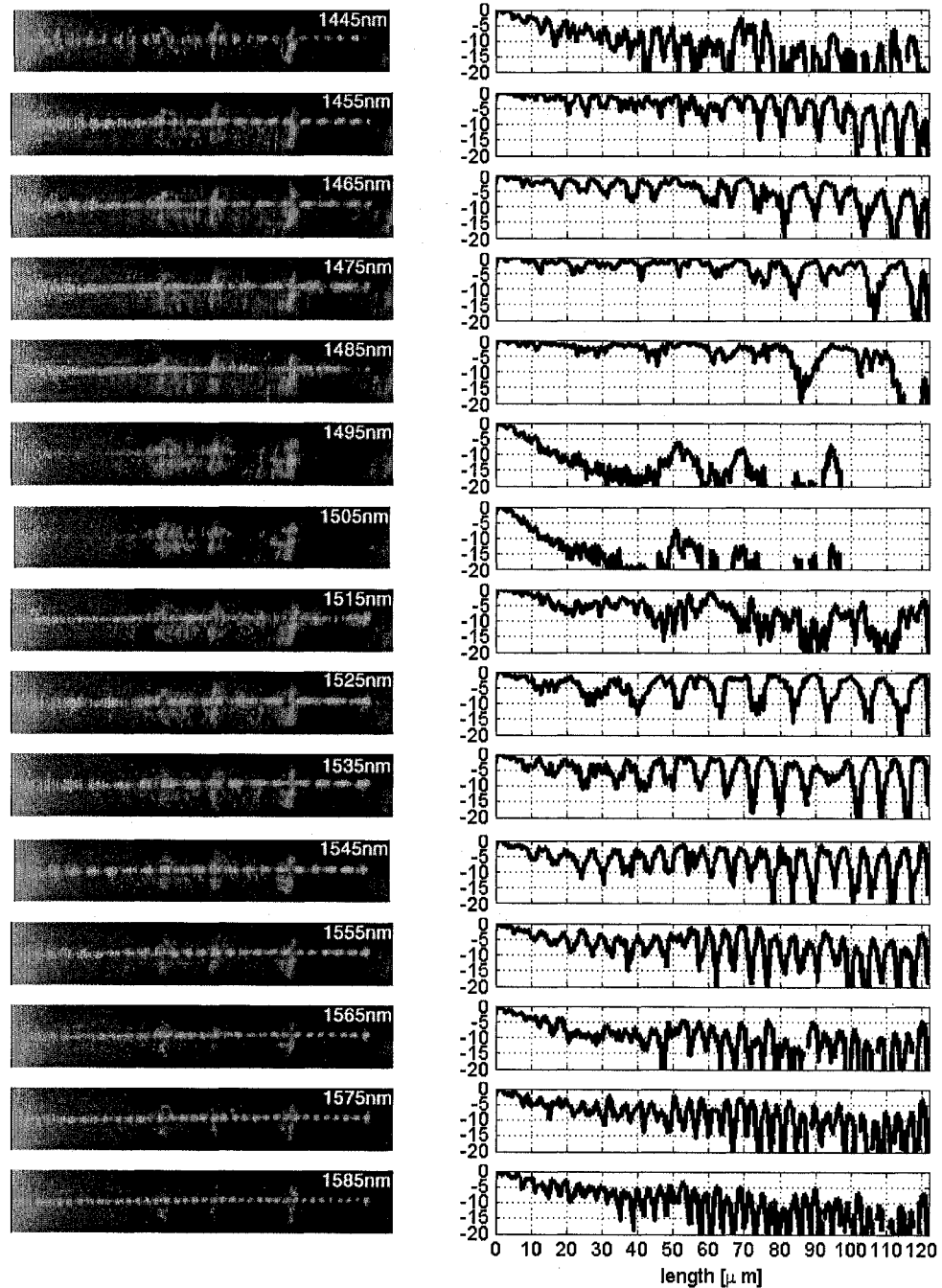


Figure 4.29: (a) Signal detected with the camera, and (b) light intensity in the waveguide normalized to the intensity at the input - line scans across the data shown in (a). Radiation losses can be seen to increase as the wavelength departs from the mini stop band centered around 1500nm.

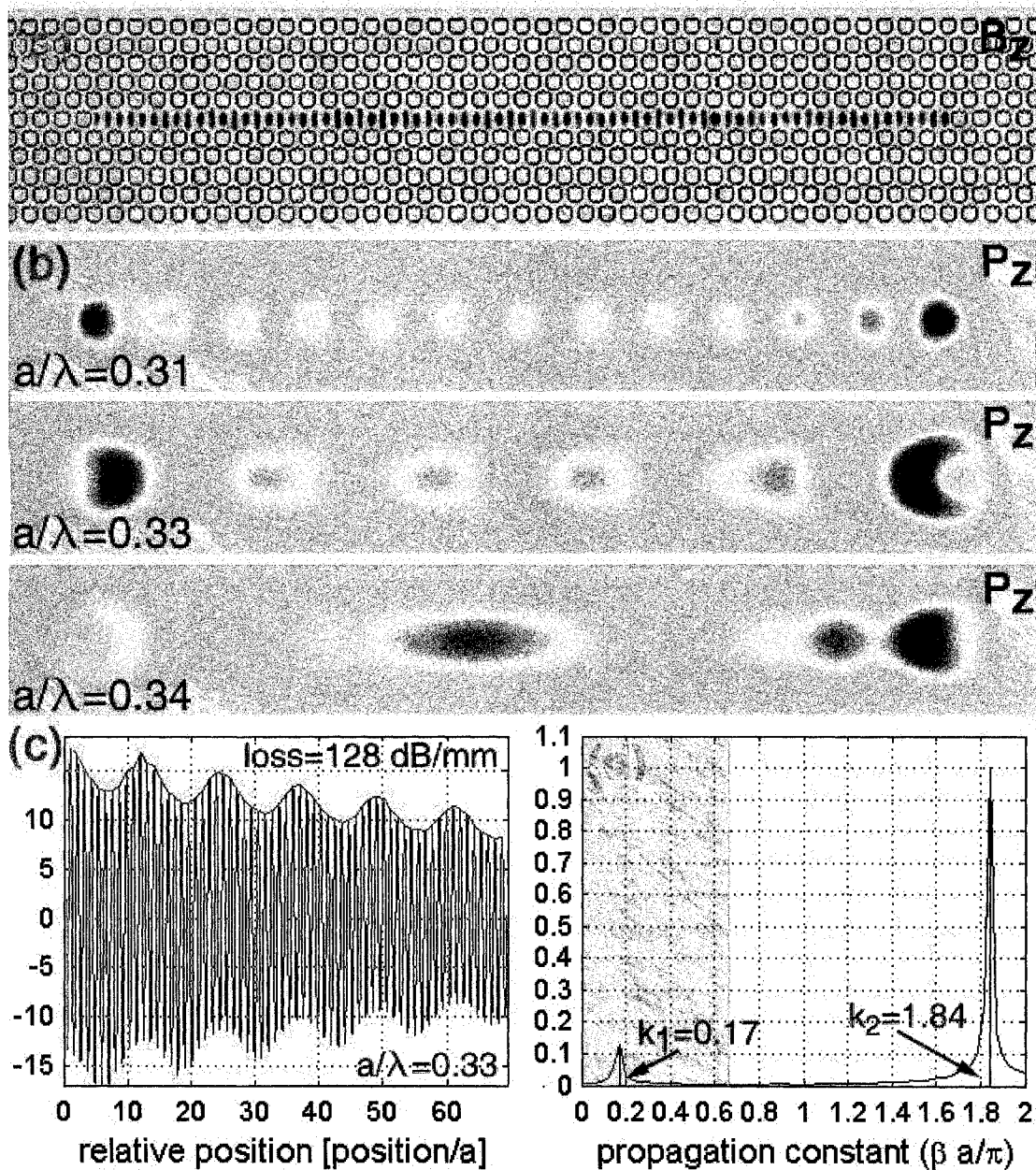


Figure 4.30: (a) Field profile ( $B_z$  taken at the middle of the slab) of a leaky mode excited in the waveguide. (b)  $P_z$  component of the Poynting vector, at a distance of about  $1\mu m$  from the top surface of the structure, shown for three different frequencies. Periodic intensity modulation can be observed. (c) Profile of  $B_z$  component taken at the center of the waveguide (envelop is shown in red). Beating between two Bloch components and signal attenuation along the waveguide can be seen. (d) Spatial frequency spectrum of the signal shown in (c). Most of the mode energy is stored in the component at  $k_2$  since its intensity is almost 10 times greater than the one at  $k_1$ . The light cone is represented in gray.

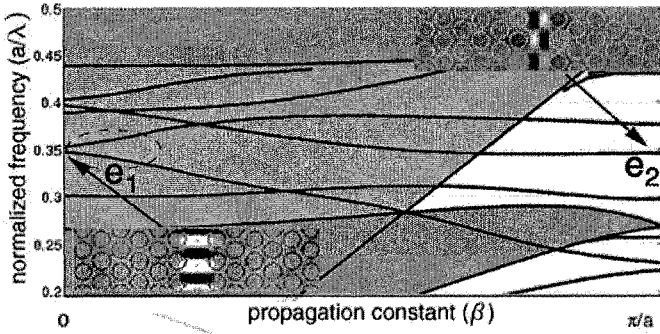


Figure 4.31: Dispersion diagram of the TE-like guided modes supported in the triangular lattice PPC waveguide. The light cone is shown in light-gray and the extended states of the surrounding PPC (projected along  $\Gamma J$  direction) in dark-gray.

symmetry of the PPC waveguide in the  $y$ -axis direction, field components of each waveguide mode can be expressed as

$$B(x, y, z) = u(x, y, z) \cdot e^{i\beta y} = \sum_K U_K(x, z) \cdot e^{i(K+\beta)y}, \quad (4.1)$$

$$U_K = \frac{1}{a} \int_{-a/2}^{a/2} u(x, y, z) \cdot e^{-iKy} dy, \quad (4.2)$$

since Bloch function  $u(x, y, z)$  is periodic [ $u(x, y, z) = u(x, y + a, z)$ ].  $B(x, y, z)$  is one of three  $\vec{B}$  field components (similar relations hold for the electric field component),  $\beta$  is Bloch wave vector limited to range  $\beta \in (-\pi/a, \pi/a)$ , and  $K$  is reciprocal space lattice vector ( $K = 0, \pm 2\pi/a, \dots$ )\*. From Equation 4.1 it follows that, in general case, each mode supported in the waveguide [defined as a single  $(\beta, a/\lambda)$  point on the dispersion diagram shown in Figure 4.31] is a *composite* mode made up of infinitely many Bloch components that are coupled by photonic crystal.

When  $\beta$  is close to zero and  $a/\lambda \in (0.33, 0.37)$  Bloch component for  $K = 0$  lies above the light line and can radiate energy in the vertical direction. On the other hand components for  $K = N \cdot 2\pi/a$ , ( $N = 1, 2, \dots$ ) are located below the light line and do not leak the energy.

\*In order to account for the losses due to radiation in the vertical direction in the case of leaky modes, Equation 4.1 should be written as  $B(x, y, z) = u(x, y, z) \cdot e^{i\beta y} \cdot e^{-\alpha y}$ , where  $\alpha$  is the propagation loss parameter.

However, they are coupled to the leaky component at  $K = 0$  by the PPC, and therefore will lose energy by coupling to that component. The ratio of energy stored in Bloch component for  $K = 0$  and the energy stored in all other components will determine the losses of the whole *composite* mode defined in Equation 2.6. In order to explore this loss mechanism in more detail, we have modelled long waveguides ( $75 \cdot a$  long,  $a = 18$  points) using distributed 3-D FDTD code. The waveguide, shown in the Figure 4.30(a), was excited by the dipole sources ( $E_x$  component) positioned at one end of the structure. The symmetry of the source was such that only  $e_1$  mode was excited. Figure 4.30(c) shows the intensity of  $B_z$  component along the center of the waveguide, when  $a/\lambda = 0.33$ . It can be seen that intensity of the field decreases as we move away from the input of the waveguide, yielding the losses of  $\approx 128\text{dB/mm}$ . The interplay between the different Bloch components is also apparent. Figure 4.30(d) shows the FFT of the line-scan shown in Figure 4.30(c). Only two spatial frequencies, located at  $k_1 = 0.17 \cdot \pi/a$  and  $k_2 = 1.84 \cdot \pi/a$ , are detected in this case, and the amplitude of component  $k_2$  is almost ten times bigger than the amplitude of  $k_1$ . Having in mind the resolution of our FFT ( $0.014 \cdot \pi/a$ ) we can conclude that  $k_2 = 2\pi/a - k_1^\dagger$ . From the dispersion diagram shown in Figure 4.31 we find that for frequency  $a/\lambda = 0.33$  Bloch wave vector has a value of  $\beta = 0.167 \cdot \pi/a$ . This agrees well with  $k_1$ . Finally, we conclude that the leaky mode of interest consists of Bloch components at  $K = 0$  and  $K = 2\pi/a$ , and that more than 90% of its energy is stored in the component at  $K = 2\pi/a$ , that lies above the light line. Because of that, the overall losses of the mode will be smaller than what would have been expected keeping in mind only its “distance” from the light line. We have calculated the losses of the  $e_1$  mode at various frequencies, and we have found that the losses are decreasing from around  $135\text{dB/mm}$  to  $33\text{dB/mm}$  when  $a/\lambda$  is changing from  $a/\lambda = 0.33$  to  $a/\lambda = 0.345$ . That is, the losses become smaller as we approach the mini stop-band located at  $\beta = 0$ . We have attributed this to the reduction of the ratio of energy stored in Bloch components at  $K = 0$  and  $K = 2 \cdot \pi/a$ .

At the end, we compare the experimentally estimated losses of the waveguide with the numerically calculated ones. The results are summarized in Table 4.2. The numerical results are obtained by the calculation ratio of energy that propagates through the waveguide

---

<sup>†</sup>This resolution was determined by discretization used in 3-D FDTD model ( $a=18$  points), determined by the memory of the computer used to perform the simulation, and by the length of 3-D FDTD time evolution

Table 4.2: Waveguide losses of the leaky  $e_1$  mode of the PPC waveguide

$a/\lambda$	Theory	Experiment
0.33	140 dB/mm	120 dB/mm
0.34	100 dB/mm	80 dB/mm
0.345	33 dB/mm	20 dB/mm

section that consists of 20 layers of photonic crystal. The waveguides were again excited using dipole sources. As mentioned above, experimental estimation of the waveguide losses is not accurate due to the multiple reflections from the facet and mirror (cavity) in the waveguide. However, it can be seen that both theory and experiment predict that losses should decrease as we approach the mini stop band at the center of the Brillouin zone.

From the experimentally obtained dispersion diagram (Figure 4.27) we can also estimate the group velocity of the light in the waveguide, by finding the derivative of the dispersion curve. Light can be significantly slowed down as we approach the mini stop band due to strong dispersion of the  $e_1$  mode. However, it was not possible to carry out the experiment at these extreme conditions (slow light) due to difficulties associated with coupling of light into the modes with small group velocity.

## 4.5 Conclusions

In conclusion, we have demonstrated design, fabrication and characterization of photonic crystal waveguides. 3-D FDTD analysis was used to model waveguides and optimize their properties. We have shown that a single line defect supports both effective index contrast guided and PBG effect guided modes. In addition, we have shown that index guiding can occur for the vertically odd modes (TM-like) although the bandgap is not open in that case. We have also presented and analyzed, using 3-D FDTD method, several mechanisms of controlling the position of the guided modes within the PPC based waveguides. Ability to engineer the position of the guided mode is very important in order to achieve efficient guiding, coupling into the waveguides and mode-matching between various PPC devices. We have developed a new fabrication technique for defining these structures in silicon on

insulator wafers. Fabrication technique involves only one mask layer and is compatible with microelectronic fabrication techniques. Photonic crystal waveguides were characterized and we were able to see the evidence of guiding of light around 60 and 90 corners. We have also demonstrated an equilibrium propagating mode of a photonic crystal waveguide that is a Bloch mode consisting of guided and radiative components. The radiative component, responsible for all the propagation losses has been experimentally and theoretically identified. Transmission losses of the leaky mode were estimated and long life-time leaky modes (reduced losses) were observed at the center of the Brillouin zone. We have explained the origin of this loss reduction and have attributed it to the ratio of energy stored in radiative and guided Bloch component.

## Bibliography

- [1] E. Yablonovitch, "Inhibited spontaneous emission in solid-state physics and electronics," *Phys. Rev. Lett.*, vol. 58, pp. 2059–2062, may 1987.
- [2] S. John, "Strong localization of photons in certain disordered dielectric superlattices," *Phys. Rev. Lett.*, vol. 58, pp. 2486–2488, 1987.
- [3] J. D. Joannopoulos, R. D. Meade, and J. N. Winn, *Photonic Crystals*. Princeton, New Jersey: Princeton University Press, 1995.
- [4] K. Sakoda, *Optical Properties of Photonic Crystals*. Springer, Berlin: Springer, 2001.
- [5] J. Jewell, J. Harbison, and A. Scherer, "Microlasers," *Scientific American*, vol. 266, p. 56, 1991.
- [6] R. F. Cregan, B. J. Mangan, J. C. Knight, T. A. Birks, P. S. J. Russell, P. J. Roberts, and D. C. Allan, "Single-mode photonic band gap guidance of light in air," *Science*, vol. 285, pp. 1537–1539, 1999.
- [7] C. Cheng and A. Scherer, "Fabrication of photonic band-gap crystals," *J. Vac. Scie. Tech. B*, vol. 13, no. 6, pp. 2696–2700, 1995.
- [8] T. Krauss, R. DeLaRue, and S. Brand, "Two-dimensional photonic-bandgap structures operating at near infrared wavelengths," *Nature*, vol. 383, no. 6602, pp. 699–702, 1996.
- [9] P. Villeneuve, S. Fan, S. Johnson, and J. Joannopoulos, "Three-dimensional photon confinement in photonic crystals of low-dimensional periodicity," *IEE Proc. Optoelet.*, vol. 145, no. 6, pp. 384–390, 1998.

- [10] O. Painter, A. Husain, A. Scherer, P. Lee, I. Kim, J. O'Brien, and P. Dapkus, "Lithographic tuning of a two-dimensional photonic crystal laser array," *IEEE Phot. Tech. Lett.*, vol. 12, no. 9, pp. 1126–1128, 2000.
- [11] H. Kosaka, T. Kawashima, A. Tomita, M. Notomi, T. Tamamura, T. Sato, and S. Kawakami, "Superprism phenomena in photonic crystals: Toward microscale light-wave circuits," *J. Lightwave Tech.*, vol. 17, no. 11, pp. 2032–2038, 1999.
- [12] A. Taflove, *Computational Electrodynamics - The Finite-Difference Time-Domain Method*. Norwood, Massachusetts: Artech House, 1995.
- [13] N. Ashcroft and N. D. Mermin, *Solid state Physics*. Saunders College Publishing, 1976.
- [14] H. Benisty, C. Weisbuch, D. Labilloy, M. Rattier, C. Smith, T. Krauss, R. De la Rue, R. Houdre, U. Oesterle, C. Jouanin, and D. Cassagne, "Optical and confinement properties of two-dimensional photonic crystals," *J. Lightwave Tech.*, vol. 17, no. 11, pp. 2063–2077, 1999.
- [15] O. Painter, J. Vučković, and A. Scherer, "Defect modes of a two-dimensional photonic crystal in an optically thin dielectric slab," *J. Opt. Soc. Am. B*, vol. 16, no. 2, pp. 275–285, 1999.
- [16] J. Witzens, M. Lončar, and A. Scherer, "Self-collimation in planar photonic crystals," *IEEE J. Sel. Top. Quant. El.*, vol. 8, no. 6, pp. 1246–1257, 2002.
- [17] S. Johnson, S. Fan, P. Villeneuve, J. Joannopoulos, and L. Kolodziejski, "Guided modes in photonic crystal slabs," *Phys. Rev. B*, vol. 60, no. 8, pp. 5751–5758, 1999.
- [18] M. Lončar, T. Doll, J. Vučković, and A. Scherer, "Design and fabrication of silicon photonic crystal optical waveguides," *J. Lightwave Tech.*, vol. 18, no. 10, pp. 1402–1411, 2000.
- [19] G. Mur, "Absorbing boundary conditions for the finite-difference approximation of the time-domain electromagnetic equations," *IEEE Trans. Electromagn. Comput.*, vol. 23, pp. 377–382, 1981.

- [20] H. Ryu, S. Kim, H. Park, J. Hwang, Y. Lee, and J. Kim, "Square-lattice photonic band-gap single-cell laser operating in the lowest-order whispering gallery mode," *Appl. Phys. Lett.*, vol. 80, no. 21, pp. 3883–3885, 2002.
- [21] M. D. B. Charlton, S. W. Roberts, and G. J. Parker, "Guided mode analysis, and fabrication of a 2-dimensional visible photonic band structure confined within a planar semiconductor waveguide," *Materials Science and Engineering B*, vol. 49, pp. 155–165, Sept. 1997.
- [22] H. Kosaka, T. Kawashima, A. Tomita, M. Notomi, T. Tamamura, T. Sato, and S. Kawakami, "Superprism phenomena in photonic crystals," *Phys. Rev. B*, vol. 58, no. 16, pp. R10096–R10099, 1998.
- [23] H. Kosaka, T. Kawashima, A. Tomita, M. Notomi, T. Tamamura, T. Sato, and S. Kawakami, "Self-collimating phenomena in photonic crystals," *Appl. Phys. Lett.*, vol. 74, no. 9, pp. 1212–1214, 1999.
- [24] H. Kosaka, T. Kawashima, A. Tomita, M. Notomi, T. Tamamura, T. Sato, and S. Kawakami, "Photonic crystals for micro lightwave circuits using wavelength-dependent angular beam steering," *Appl. Phys. Lett.*, vol. 74, no. 10, pp. 1370–1372, 1999.
- [25] M. Notomi, "Theory of light propagation in strongly modulated photonic crystals: Refractionlike behavior in the vicinity of the photonic band gap," *Phys. Rev. B*, vol. 62, no. 16, pp. 10696–10705, 2000.
- [26] E. Silvestre, J. Pottage, P. Russell, and P. Roberts, "Design of thin-film photonic crystal waveguides," *Appl. Phys. Lett.*, vol. 77, no. 7, pp. 942–944, 2000.
- [27] B. Gralak, S. Enoch, and G. Tayeb, "Anomalous refractive properties of photonic crystals," *J. of Optical Soc. of Am. B*, vol. 17, p. 1012, 2000.
- [28] C. Luo, S. Johnson, and J. Joannopoulos, "All-angle negative refraction in a three-dimensionally periodic photonic crystal," *Appl. Phys. Lett.*, vol. 81, no. 13, pp. 2352–2354, 2002.
- [29] T. Baba and T. Matsumoto, "Resolution of photonic crystal superprism," *Appl. Phys. Lett.*, vol. 81, no. 13, pp. 2325–2327, 2002.

- [30] T. Baba and M. Nakamura, "Photonic crystal light deflection devices using the superprism effect," *IEEE J. Quant. El.*, vol. 38, no. 7, pp. 909–914, 2002.
- [31] L. Wu, M. Mazilu, T. Karle, and T. Krauss, "Superprism phenomena in planar photonic crystals," *IEEE J. Quant. El.*, vol. 38, no. 7, pp. 915–918, 2002.
- [32] M. Lončar, T. Yoshie, A. Scherer, P. Gogna, and Y. Qiu, "Low-threshold photonic crystal laser," *Appl. Phys. Lett.*, vol. 81, no. 15, pp. 2680–2682, 2002.
- [33] M. Lončar, A. Scherer, and Y. Qiu, "Photonic crystal laser sources for chemical detection," *to appear in Appl. Phys. Lett.*, 2003.
- [34] E. Yablonovitch, T. Gmitter, R. Meade, A. Rappe, K. Brommer, and J. Joannopoulos, "Donor and acceptor modes in photonic band-structure," *Phys. Rev. Lett.*, vol. 67, no. 24, pp. 3380–3383, 1991.
- [35] J. Vučković, M. Lončar, H. Mabuchi, and A. Scherer, "Design of photonic crystal microcavities for cavity QED," *Phys. Rev. E*, vol. 6501, no. 1, pp. art. no.–016608, 2002.
- [36] J. Vučković, M. Lončar, and A. Scherer, "Design of photonic crystal optical microcavities," *Proceedings of SPIE Photonics West Conference, San Jose, CA*, January 2001.
- [37] J. Vučković and Y. Yamamoto, "Photonic crystal microcavities for cavity quantum electrodynamics with a single quantum dot," *Appl. Phys. Lett.*, vol. 82, no. 15, pp. 2374–2376, 2003.
- [38] K. Srinivasan and O. Painter, "Momentum space design of high-Q photonic crystal optical cavities," *Opt. Exp.*, vol. 10, no. 15, pp. 670–684, 2002.
- [39] M. Watts, S. Johnson, H. Haus, and J. Joannopoulos, "Electromagnetic cavity with arbitrary Q and small modal volume without a complete photonic bandgap," *Opt. Lett.*, vol. 27, no. 20, pp. 1785–1787, 2002.
- [40] E. Miyai and K. Sakoda, "Quality factor for localized defect modes in a photonic crystal slab upon a low-index dielectric substrate," *Opt. Lett.*, vol. 26, no. 10, pp. 740–742, 2001.

- [41] T. Yoshie, J. Vučković, A. Scherer, H. Chen, and D. Deppe, "High quality two-dimensional photonic crystal slab cavities," *Appl. Phys. Lett.*, vol. 79, no. 26, pp. 4289–4291, 2001.
- [42] S. Johnson, S. Fan, A. Mekis, and J. Joannopoulos, "Multipole-cancellation mechanism for high-Q cavities in the absence of a complete photonic band gap," *Appl. Phys. Lett.*, vol. 78, no. 22, pp. 3388–3390, 2001.
- [43] H. Park, J. Hwang, J. Huh, H. Ryu, Y. Lee, and J. Kim, "Nondegenerate monopole-mode two-dimensional photonic band gap laser," *Appl. Phys. Lett.*, vol. 79, no. 19, pp. 3032–3034, 2001.
- [44] P. Pottier, C. Seassal, X. Letartre, J. Leclercq, P. Viktorovitch, D. Cassagne, and C. Jouanin, "Triangular and hexagonal high Q-factor 2-D photonic bandgap cavities on III-V suspended membranes," *J. Lightwave Tech.*, vol. 17, no. 11, pp. 2058–2062, 1999.
- [45] J. O'Brien, O. Painter, R. Lee, C. Cheng, A. Yariv, and A. Scherer, "Lasers incorporating 2-D photonic bandgap mirrors," *Elect. Lett.*, vol. 32, no. 24, pp. 2243–2244, 1996.
- [46] M. Meier, A. Mekis, A. Dodabalapur, A. Timko, R. Slusher, J. Joannopoulos, and O. Nalamasu, "Laser action from two-dimensional distributed feedback in photonic crystals," *Appl. Phys. Lett.*, vol. 74, no. 1, pp. 7–9, 1999.
- [47] K. Inoue, M. Sasada, J. Kawamata, K. Sakoda, and J. Haus, "A two-dimensional photonic crystal laser," *Jap. J. Appl. Phys. 2*, vol. 38, no. 2B, pp. L157–L159, 1999.
- [48] R. Lee, O. Painter, B. Kitzke, A. Scherer, and A. Yariv, "Photonic bandgap disk laser," *Elect. Lett.*, vol. 35, no. 7, pp. 569–570, 1999.
- [49] O. Painter, R. Lee, A. Scherer, A. Yariv, J. O'Brien, P. Dapkus, and I. Kim, "Two-dimensional photonic band-gap defect mode laser," *Science*, vol. 284, no. 5421, pp. 1819–1821, 1999.
- [50] M. Imada, S. Noda, A. Chutinan, T. Tokuda, M. Murata, and G. Sasaki, "Coherent two-dimensional lasing action in surface-emitting laser with triangular-lattice photonic crystal structure," *Appl. Phys. Lett.*, vol. 75, no. 3, pp. 316–318, 1999.

- [51] J. Hwang, H. Ryu, D. Song, I. Han, H. Song, H. Park, Y. Lee, and D. Jang, "Room-temperature triangular-lattice two-dimensional photonic band gap lasers operating at  $1.54 \mu\text{m}$ ," *Appl. Phys. Lett.*, vol. 76, no. 21, pp. 2982–2984, 2000.
- [52] M. Notomi, H. Suzuki, and T. Tamamura, "Directional lasing oscillation of two-dimensional organic photonic crystal lasers at several photonic band gaps," *Appl. Phys. Lett.*, vol. 78, no. 10, pp. 1325–1327, 2001.
- [53] T. Happ, A. Markard, M. Kamp, J. Gentner, and A. Forchel, "InP-based short cavity lasers with 2D photonic crystal mirror," *Elect. Lett.*, vol. 37, no. 7, pp. 428–429, 2001.
- [54] C. Monat, C. Seassal, X. Letartre, P. Viktorovitch, P. Regreny, M. Gendry, P. Rojo-Romeo, G. Hollinger, E. Jalaguier, S. Pocas, and B. Aspar, "InP 2-D photonic crystal microlasers on silicon wafer: room temperature operation at  $1.55 \mu\text{m}$ ," *Elect. Lett.*, vol. 37, no. 12, pp. 764–766, 2001.
- [55] M. Fujita and T. Baba, "Microgear laser," *Appl. Phys. Lett.*, vol. 80, no. 12, pp. 2051–2053, 2002.
- [56] P. Lee, J. Cao, S. Choi, Z. Wei, J. O'Brien, and P. Dapkus, "Room-temperature operation of VCSEL-pumped photonic crystal lasers," *IEEE Phot. Tech. Lett.*, vol. 14, no. 4, pp. 435–437, 2002.
- [57] H. Ryu, S. Kwon, Y. Lee, Y. Lee, and J. Kim, "Very-low-threshold photonic band-edge lasers from free-standing triangular photonic crystal slabs," *Appl. Phys. Lett.*, vol. 80, no. 19, pp. 3476–3478, 2002.
- [58] M. Imada, A. Chutinan, S. Noda, and M. Mochizuki, "Multidirectionally distributed feedback photonic crystal lasers," *Phys. Rev. B*, vol. 65, no. 19, pp. art. no.–195306, 2002.
- [59] T. Yoshie, O. Shchekin, H. Chen, D. Deppe, and A. Scherer, "Quantum dot photonic crystal lasers," *Elect. Lett.*, vol. 38, no. 17, pp. 967–968, 2002.
- [60] S. Kim, H. Ryu, H. Park, G. Kim, Y. Choi, Y. Lee, and J. Kim, "Two-dimensional photonic crystal hexagonal waveguide ring laser," *Appl. Phys. Lett.*, vol. 81, no. 14, pp. 2499–2501, 2002.

- [61] C. Monat, C. Seassal, X. Letartre, R. Regreny, P. Rojo-Romeo, P. Viktorovitch, M. d'Yerville, D. Cassagne, J. Albert, E. Jalaguier, S. Pocas, and B. Aspar, "InP-based two-dimensional photonic crystal on silicon: In-plane bloch mode laser," *Appl. Phys. Lett.*, vol. 81, no. 27, pp. 5102–5104, 2002.
- [62] A. Sugitatsu and S. Noda, "Room temperature operation of 2-D photonic crystal slab defect-waveguide laser with optical pump," *Elect. Lett.*, vol. 39, no. 2, pp. 213–215, 2003.
- [63] M. Lončar, T. Yoshie, A. Scherer, P. Gogna, and Y. Qiu, "Low-threshold photonic crystal laser," *Proceedings of SPIE Photonics West Conference, San Jose, CA*, January 2003.
- [64] J. Vučković, M. Lončar, H. Mabuchi, and A. Scherer, "Optimization of the Q factor in photonic crystal microcavities," *IEEE J. Quant. El.*, vol. 38, no. 7, pp. 850–856, 2002.
- [65] S. Noda, M. Yokoyama, M. Imada, A. Chutinan, and M. Mochizuki, "Polarization mode control of two-dimensional photonic crystal laser by unit cell structure design," *Science*, vol. 293, no. 5532, pp. 1123–1125, 2001.
- [66] K. Okamoto, M. Lončar, T. Yoshie, A. Scherer, Y. Qiu, and P. Gogna, "Near-field scanning optical microscopy of photonic crystal nanocavities," *Appl. Phys. Lett.*, vol. 82, no. 11, pp. 1676–1678, 2003.
- [67] A. Sakai, T. Fukazawa, and T. Baba, "Low loss ultra-small branches in a silicon photonic wire waveguide," *IEICE Trans. Elect.*, vol. E85C, no. 4, pp. 1033–1038, 2002.
- [68] C. Manolatou, J. S. G., S. Fan, P. Villeneuve, H. Haus, and J. Joannopoulos, "High-density integrated optics," *J. of Lightwave Tech.*, vol. 17, pp. 1682–1692, 1999.
- [69] A. Mekis, J. Chen, I. Kurland, S. Fan, P. Villeneuve, and J. Joannopoulos, "High transmission through sharp bends in photonic crystal waveguides," *Phys. Rev. Lett.*, vol. 77, no. 18, pp. 3787–3790, 1996.
- [70] A. Chutinan and S. Noda, "Waveguides and waveguide bends in two-dimensional photonic crystal slabs," *Phys. Rev. B*, vol. 62, no. 7, pp. 4488–4492, 2000.

- [71] E. Chow, S. Lin, J. Wendt, S. Johnson, and J. Joannopoulos, "Quantitative analysis of bending efficiency in photonic-crystal waveguide bends at  $\lambda=1.55 \mu\text{m}$  wavelengths," *Opt. Lett.*, vol. 26, no. 5, pp. 286–288, 2001.
- [72] J. Zimmermann, M. Kamp, R. Schwertberger, J. Reithmaier, A. Forchel, and R. Marz, "Efficient light transmission through InP-based photonic crystal waveguides," *Elect. Lett.*, vol. 38, no. 4, pp. 178–180, 2002.
- [73] A. Chutinan, M. Okano, and S. Noda, "Wider bandwidth with high transmission through waveguide bends in two-dimensional photonic crystal slabs," *Appl. Phys. Lett.*, vol. 80, no. 10, pp. 1698–1700, 2002.
- [74] Y. Sugimoto, N. Ikeda, N. Carlsson, K. Asakawa, N. Kawai, and K. Inoue, "Experimental verification of guided modes in 60 degrees-bent defect waveguides in algaas-based air-bridge-type two-dimensional photonic crystal slabs," *J. Appl. Phys.*, vol. 91, no. 5, pp. 3477–3479, 2002.
- [75] A. Talneau, L. Le Gouezigou, N. Bouadma, M. Kafesaki, C. Soukoulis, and M. Agio, "Photonic-crystal ultrashort bends with improved transmission and low reflection at  $1.55 \mu\text{m}$ ," *Appl. Phys. Lett.*, vol. 80, no. 4, pp. 547–549, 2002.
- [76] A. Yariv, Y. Xu, R. Lee, and A. Scherer, "Coupled-resonator optical waveguide: a proposal and analysis," *Opt. Lett.*, vol. 24, no. 11, pp. 711–713, 1999.
- [77] S. Nishikawa, S. Lan, N. Ikeda, Y. Sugimoto, H. Ishikawa, and K. Asakawa, "Optical characterization of photonic crystal delay lines based on one-dimensional coupled defects," *Opt. Lett.*, vol. 27, no. 23, pp. 2079–2081, 2002.
- [78] S. Johnson, P. Villeneuve, S. Fan, and J. Joannopoulos, "Linear waveguides in photonic-crystal slabs," *Phys. Rev. B*, vol. 62, no. 12, pp. 8212–8222, 2000.
- [79] M. Notomi, K. Yamada, A. Shinya, J. Takahashi, C. Takahashi, and I. Yokohama, "Extremely large group-velocity dispersion of line-defect waveguides in photonic crystal slabs," *Phys. Rev. Lett.*, vol. 8725, no. 25, pp. art. no.–253902, 2001.
- [80] M. Lončar, D. Nedeljković, T. Pearsall, J. Vučković, A. Scherer, S. Kuchinsky, and D. Allan, "Experimental and theoretical confirmation of bloch-mode light propagation in photonic crystal waveguides," *Phys. Rev. Lett.*, vol. 8725, no. 25, pp. art. no.–253903, 2001.

- gation in planar photonic crystal waveguides," *Appl. Phys. Lett.*, vol. 80, no. 10, pp. 1689–1691, 2002.
- [81] Y. Xu, R. Lee, and A. Yariv, "Propagation and second-harmonic generation of electromagnetic waves in a coupled-resonator optical waveguide," *J. Opt. Soc. Am. B*, vol. 17, no. 3, pp. 387–400, 2000.
- [82] S. Mookherjea and A. Yariv, "Second-harmonic generation with pulses in a coupled-resonator optical waveguide," *Phys. Rev. E*, vol. 65, no. 2, pp. art. no.–026607, 2002.
- [83] M. Soljacic, S. Johnson, S. Fan, M. Ibanescu, E. Ippen, and J. Joannopoulos, "Photonic-crystal slow-light enhancement of nonlinear phase sensitivity," *J. Opt. Soc. Am. B*, vol. 19, no. 9, pp. 2052–2059, 2002.
- [84] M. Rahn, A. Fox, M. Skolnick, and T. Krauss, "Propagation of ultrashort nonlinear pulses through two-dimensional AlGaAs high-contrast photonic crystal waveguides," *J. Opt. Soc. Am. B*, vol. 19, no. 4, pp. 716–721, 2002.
- [85] R. Meade, A. Devenyi, J. Joannopoulos, O. Alerhand, D. Smith, and K. Kash, "Novel applications of photonic band-gap materials - low-loss bends and high-q cavities," *J. Appl. Phys.*, vol. 75, no. 9, pp. 4753–4755, 1994.
- [86] Y. Xu, R. Lee, and A. Yariv, "Adiabatic coupling between conventional dielectric waveguides and waveguides with discrete translational symmetry," *Opt. Lett.*, vol. 25, no. 10, pp. 755–757, 2000.
- [87] A. Talneau, P. Lalanne, M. Agio, and C. Soukoulis, "Low-reflection photonic-crystal taper for efficient coupling between guide sections of arbitrary widths," *Opt. Lett.*, vol. 27, no. 17, pp. 1522–1524, 2002.
- [88] A. Mekis and J. Joannopoulos, "Tapered couplers for efficient interfacing between dielectric and photonic crystal waveguides," *J. Lightwave Tech.*, vol. 19, no. 6, pp. 861–865, 2001.
- [89] M. Lončar, J. Vučković, and A. Scherer, "Methods for controlling positions of guided modes of photonic-crystal waveguides," *J. Opt. Soc. Am. B*, vol. 18, no. 9, pp. 1362–1368, 2001.

- [90] M. Notomi, A. Shinya, E. Kuramochi, I. Yokohama, C. Takahashi, K. Yamada, J. Takahashi, T. Kawashima, and S. Kawakami, “Si-based photonic crystals and photonic-bandgap waveguides,” *IEICE Trans. Elect.*, vol. E85C, no. 4, pp. 1025–1032, 2002.
- [91] A. Yariv, “Coupled-wave formalism for optical waveguiding by transverse bragg reflection,” *Opt. Lett.*, vol. 27, no. 11, pp. 936–938, 2002.
- [92] H. Benisty, “Modal analysis of optical guides with two-dimensional photonic band-gap boundaries,” *Journal of Applied Physics*, vol. 79, pp. 7483–7492, May 1996.
- [93] A. Adibi, R. Lee, Y. Xu, A. Yariv, and A. Scherer, “Design of photonic crystal optical waveguides with singlemode propagation in the photonic bandgap,” *Elect. Lett.*, vol. 36, no. 16, pp. 1376–1378, 2000.
- [94] A. Chutinan and S. Noda, “Effects of structural fluctuations on the photonic bandgap during fabrication of a photonic crystal,” *J. Opt. Soc. Am. B*, vol. 16, no. 2, pp. 240–244, 1999.
- [95] T. Baba, N. Fukaya, and J. Yonekura, “Observation of light propagation in photonic crystal optical waveguides with bends,” *Elect. Lett.*, vol. 35, no. 8, pp. 654–655, 1999.
- [96] M. Tokushima, H. Kosaka, A. Tomita, and H. Yamada, “Lightwave propagation through a 120° sharply bent single-line defect photonic crystal waveguide,” *Applied Physics Letters*, vol. 76, pp. 952–954, Feb. 2000.
- [97] M. Lončar, D. Nedeljković, T. Doll, J. Vučković, A. Scherer, and T. Pearsall, “Waveguiding in planar photonic crystals,” *Appl. Phys. Lett.*, vol. 77, no. 13, pp. 1937–1939, 2000.
- [98] A. Talneau, L. Le Gouezigou, and N. Bouadma, “Quantitative measurement of low propagation losses at  $1.55 \mu\text{m}$  on planar photonic crystal waveguides,” *Opt. Lett.*, vol. 26, no. 16, pp. 1259–1261, 2001.
- [99] T. Baba, N. Fukaya, and A. Motegi, “Clear correspondence between theoretical and experimental light propagation characteristics in photonic crystal waveguides,” *Elect. Lett.*, vol. 37, no. 12, pp. 761–762, 2001.

- [100] Y. Desieres, T. Benyattou, R. Orobtchouk, A. Morand, P. Benech, C. Grillet, C. Seassal, X. Letartre, P. Rojo-Romeo, and P. Viktorovitch, "Propagation losses of the fundamental mode in a single line-defect photonic crystal waveguide on an InP membrane," *J. Appl. Phys.*, vol. 92, no. 5, pp. 2227–2234, 2002.
- [101] T. Ochiai and K. Sakoda, "Dispersion relation and optical transmittance of a hexagonal photonic crystal slab," *Phys. Rev. B*, vol. 6312, no. 12, pp. art. no.–125107, 2001.
- [102] L. Andreani and M. Agio, "Intrinsic diffraction losses in photonic crystal waveguides with line defects," *Appl. Phys. Lett.*, vol. 82, no. 13, pp. 2011–2013, 2003.